Strong magnetic fields of accreting neutron stars

Modeling cyclotron resonance scattering features

Dissertation
zur Erlangung des Grades eines
Doktors der Naturwissenschaften
der Fakultät für Mathematik und Physik
der Eberhard-Karls-Universität Tübingen

vorgelegt von

Gabriele Schönherr

aus Düsseldorf
2007

Selbstverlegt von: G. Schönherr
Carl-Maria-Splett Str. 24
40595 Düsseldorf

Tag der mündlichen Prüfung: 27.6.2007

Dekan: Prof. Dr. N. Schopohl

1. Berichterstatter: Prof. Dr. A. Santangelo
2. Berichterstatter: Prof. Dr. J. Wilms

Erweiterte deutsche Zusammenfassung

Schönherr, Gabriele

Starke Magnetfelder akkretierender Neutronensterne — Modellierung von Zyklotronlinien —

Akkretierende Neutronensterne in Röntgendoppelsternsystemen sind einzigartige astrophysikalische Laboratorien für das Studium der Physik unter extremen Bedingungen. Nicht nur bedingt ihre Kompaktheit ein Maß an Gravitation das nur noch von Schwarzlochsystemen übertroffen wird; sie können auch extrem starke Magnetfelder, millionenfach stärker als das stärkste bisher auf Erden erzeugte Magnetfeld, haben. Diese Magnetfelder bestimmen die beobachtbaren Strahlungscharakteristika, darunter das wohl auffälligste die Emission von Strahlungspulsen. Ursprung und Struktur der Magnetfelder sind allerdings bis heute noch sehr rätselhaft.

Die einzig derzeit bekannte Methode, das Magnetfeld eines Neutronensterns zu vermessen, basiert auf dem Studium von Zyklotronlinien. Diese Spektrallinien wurden erstmals für das Doppelsternsystem Hercules X-1 entdeckt. Seitdem sind Zyklotronlinien für mehr als ein Dutzend Röntgenpulsare beobachtet worden. Sie entstehen durch resonante Streuprozesse von hochenergetischen Photonen mit quantisierten Elektronen in der akkretierten Materie an den Polen des Neutronensterns. Die Linienenergien sind nahezu proportional zum Oberflächenmagnetfeld des Neutronensterns. Die Untersuchung ihrer Profile bietet einen mächtigen Zugang zu der faszinierenden jedoch nur schlecht verstandenen Physik der Akkretion.

Der Zugriff auf qualitativ hochwertige Daten von Satelliten wie *BeppoSAX*, *RXTE*, *INTEGRAL* und *Suzaku*, hat die diagnostische Bedeutung von Zyklotronlinien heutzutage einerseits gesteigert. Andererseits gibt es bisher kein konkretes physikalisches Modell, um ihre komplexen Profile im Detail zu erklären. Stattdessen werden die Linienparameter und die Magnetfeldstärke mit phänomenologischen Modellen bestimmt. Mit solchen Ansätzen die zugrunde liegende Physik der Linienentstehung zu erschließen ist extrem schwierig.

Im Rahmen dieser Arbeit werden Zyklotronlinien mit Monte Carlo Simulationen berechnet. Die Linienprofile werden von Parametern wie dem Magnetfeld, der Akkretionsgeometrie, der Plasmatemperatur und optischen Tiefe, und des Austrittswinkels der Photonen abgeleitet. Darauf aufbauend wird ein neues Interpolations- und Faltungsmodell zur Modellierung von Zyklotronlinien in den Spektren von Röntgenpulsaren entwickelt. Dessen Implementierung als lokales Modell, genannt `cyclomc`, für die *XSPEC* Spektralanalyse-Software ermöglicht einen direkten Vergleich mit Beobachtungsdaten. Fitresultate für die Beobachtungen dreier Röntgenpulsare, V0332+53, Cen X-3 und 4U 1907+09, mit `cyclomc` erlauben einen ersten Blick auf die grundlegende Physik über einen phänomenologischen Ansatz hinaus.

Abstract

Schönherr, Gabriele

Strong magnetic fields of accreting neutron stars
— Modeling cyclotron lines —

Accreting neutron stars in X-ray binaries are unique astrophysical laboratories for studying the physics of matter under extreme conditions. Not only does their compact nature lead to an amount of gravity only topped by black hole systems; they can also possess extreme magnetic fields, exceeding the highest magnetic field which has ever been produced on Earth by a million times. These magnetic fields dominate the observed radiation characteristics, the most prominent being pulsed emission. The origin and structure of the magnetic fields, however, is still highly enigmatic.

The only direct method currently known for probing the magnetic field of a neutron star is the study of cyclotron resonance scattering features. These features, first discovered in the spectrum of the binary system Hercules X-1, have been observed as absorption lines in the spectra of more than a dozen accreting X-ray pulsars. They form due to resonant scattering processes of high energy photons with quantized electrons in the accreted matter at the neutron star poles. Their line energies are approximately proportional to the surface magnetic field strength of the neutron star. Moreover, the analysis of their shapes is a powerful tool for assessing the fascinating but poorly understood physics of accretion.

Today, with the access to data from satellites like *BeppoSAX*, *RXTE*, *INTEGRAL* and *Suzaku*, the diagnostic potential of cyclotron lines has grown anew: with these instruments the observed cyclotron line features have been energetically resolved in detail. On the other hand, explicit physical models to understand their complex observed shapes are lacking. Phenomenological models are used to obtain their characteristic parameters and to determine the magnetic field strength. The underlying physics, however, are extremeley difficult to assess with such an approach.

In the scope of this work, cyclotron resonance scattering features are calculated for typical neutron star spectra using Monte Carlo simulations. The line profiles are inferred under the assumption of physical parameters such as the magnetic field, the accretion geometry, the plasma temperature and optical depth, and the emergent angle of radiation. Based on these simulations, a new interpolation and convolution model is developed for modeling cyclotron lines in X-ray pulsar continua. This model is further implemented as a local model, named `cyclomc`, into the spectral fitting analysis package *XSPEC* to allow for a direct comparison with observational data. Results, obtained from fitting cyclotron lines for observations of the X-ray pulsars V0332+53, Cen X-3 and 4U 1907+09 with `cyclomc` allow for a first glimpse on the physics beyond a phenomenological analysis.

To my parents

Contents

1 Introduction **1**

2 Accreting X-ray pulsars **6**
2.1 Neutron stars 7
2.2 X-ray binaries 10
2.3 Accretion mechanisms 15
2.3.1 Distant accretion flow 17
2.3.2 Magnetospheric accretion 18
2.4 Pulsar mechanism and pulse profiles 22
2.5 Spectral properties 25
2.6 Gravity 28

3 Cyclotron line formation in strong magnetic fields **32**
3.1 Neutron star magnetic fields 32
3.2 Line formation in magnetized accreting neutron stars 34
3.3 Observational data 35
3.4 Theory of line formation 42
3.4.1 Quantization of electrons in a strong magnetic field 42
3.4.2 Cross sections for magnetic Compton scattering 44
3.5 Numerical models 48

4 Model design **53**
4.1 Aims 53
4.2 Methods 53
4.3 Physical setting 54
4.3.1 Magnetic field 54
4.3.2 Plasma electrons 54
4.3.3 Optical depth 55
4.3.4 Geometry 55
4.4 Technical realization 56
4.5 Consistency check and modeling progress 61

5 Theoretical predictions **63**
5.1 Geometry and optical depth 63
5.2 Angular redistribution 65
5.2.1 Isotropic photon injection 65
5.2.2 Non-isotropic photon injection 70
5.2.3 Mixing different angular contributions 71
5.3 Line energies vs. magnetic field strength B 74
5.3.1 Uniform magnetic field 74
5.3.2 Non-uniform magnetic field 74
5.4 Influence of the plasma temperature 78
5.5 Continuum shape and photon spawning 79

6 Comparison with observations **82**
6.1 Instruments 82
6.2 Source sample 84
6.3 Calculation of synthetic spectra 87
6.4 Observability of the predicted line features 89
6.5 `cyclomc` – an *XSPEC* model for fitting cyclotron lines 99
6.5.1 The first candidate – 'a long way down': V0332+53 101
6.5.2 Going further – Do we observe a correlation of the temperature and the cyclotron resonance energy? 104

7 Summary and conclusions **111**

Bibliography **117**

A Model implementation in *XSPEC* **126**

Acknowledgements 132

Curriculum vitae 134

Lebenslauf 135

List of Figures

1.1 Electromagnetic spectrum and atmospheric absorption. 2
1.2 Discovery observation of Sco X-1. 3
1.3 The galactic center in X-rays. 4
2.1 Discovery of pulsations in the light curve of Cen X-3. 7
2.2 Supernova classification. 8
2.3 Radio pulsar masses 9
2.4 Sketch of an accreting X-ray binary. 10
2.5 Spin period distribution of X-ray binaries. 11
2.6 Be mechanism for accretion 11
2.7 P-$\dot{P}$ diagram for neutron stars. 14
2.8 Evolutionary scenario for a ms pulsar formation 15
2.9 Accretion mechanisms. 16
2.10 Artist's impression of an X-ray binary. 17
2.11 Accretion regimes. 18
2.12 Magnetospheric accretion. 19
2.13 Filling of the accretion column. 20
2.14 Fan and pencil beam scenarios 21
2.15 Lighthouse effect. 22
2.16 Pulse profiles for Cen X-3, Her X-1 and Vela X-1. 23
2.17 Light curve and pulse profiles for Vela X-1. 24
2.18 X-ray pulsar spectra. 25
2.19 Broad-band spectrum of Her X-1. 26
2.20 Seed photon production mechanisms in the accretion column . . 27
2.21 Theoretical X-ray pulsar continuum spectrum. 29
2.22 Light deflection by a neutron star 31
3.1 Magnetic fields of different classes of pulsars 33
3.2 First cyclotron line detection for Her X-1 36
3.3 Detection of five CRSFs for 4U 0115+63 37
3.4 Phase-resolved analysis of CRSFs 39
3.5 Phenomenological fit of CRSFs in V0332+53 40
3.6 Parameter correlations for CRSFs. 41

3.7 Luminosity dependence of the fundamental CRSF. 42
3.8 Frequency dependence of magnetic scattering cross sections. . . 46
3.9 Analytic approximation of QED cross sections. 47
3.10 Scattering vs. absorption cross sections. 49
3.11 Geometries of the line-forming region. 50
3.12 Monte Carlo spectra from Isenberg, Lamb & Wang (1998b). . . 51
4.1 Profiles for electron-photon magnetic scattering 57
4.2 Monte Carlo Green's functions for photon redistribution 59
4.3 Monte Carlo Green's functions for photon redistribution II . . . 60
4.4 Modeling progress. 62
5.1 Line profiles for cylinder geometry. 64
5.2 Line profiles for slab 1-1 geometry. 65
5.3 Line profiles for slab 1-0 geometry. 66
5.4 Comparison of 1-1 and 1-0 slab geometry 67
5.5 Angular redistribution after scattering 68
5.6 Angle-dependent variation of the fundamental CRSF 69
5.7 Angular redistribution of the photons from unidirectional injection. 70
5.8 Distorted dipole geometry. 72
5.9 Effects of two-pole contributions. 73
5.10 Line profiles for different magnetic field strengths B 75
5.11 Comparison of a uniform and a non-uniform magnetic field . . . 76
5.12 Toy model for a magnetic field gradient 77
5.13 Dependence of the line shapes on the plasma temperature 78
5.14 Effects of photon spawning 80
5.15 Dependence of the line profiles on the continuum shape 81
6.1 Her X-1 synthetic spectra 90
6.2 V0332+53 synthetic spectra 91
6.3 A0535+26 synthetic spectra 92
6.4 4U 0115+63 synthetic spectra 93
6.5 V0332+53 synthetic spectra 94
6.6 4U 1907+09 synthetic spectra 95
6.7 Cen X-3 synthetic spectra 96
6.8 *RXTE HEXTE* simulations of a source with CRSFs. 98
6.9 Early-stage fit of V0332+53, cylinder, table model & local model. 100
6.10 Fit of V0332+53 data. 102
6.11 Fit of V0332+53 data, partial covering. 103
6.12 Fit parameter variation for V0332+53 105
6.13 Fit of 4U 1907+09 data, slab 1-0, partial covering. 107
6.14 Fit of Cen X-3 data, slab 1-0, partial covering 108
6.15 Temperature vs. cyclotron resonance. 110

A.1 FITS tables for `cyclomc`. 127
A.2 Illustration of Green's functions storage in FITS tables. 128

List of Tables

2.1	Mass constraints for white dwarfs, neutron stars and black holes.	9
3.1	List of sources with observed CRSFs.	38
4.1	Simulation parameter grid.	60
5.1	Comparison of a uniform and a non-uniform magnetic field.	77
6.1	Instrumental characteristics.	83
6.2	Source parameters for synthetic spectra.	97
6.3	Best fit parameters for V0332+53.	106
6.4	Best fit parameters for 4U 1907+09.	109
6.5	Best fit parameters for Cen X-3.	109

CHAPTER 1

Introduction

"I wonder why, I wonder why.
I wonder why I wonder...
I wonder why I wonder why,
I wonder why I wonder."
[Richard Feynman]

X-ray astronomy

X-ray astronomers indeed have had a lot to wonder about during the last decades. Since the first detection of extrasolar X-rays in the 1960s, an exciting new world has been opening up in the X-ray waveband. Different from the optical sky, the X-ray sky is a violent and constantly changing sight. The observed objects have temperatures of 10^6 K and higher, hinting at the presence of extreme conditions. Strong magnetic fields, very high gravity or explosive forces are often involved. Black holes and accreting neutron stars are among the objects observed in this hot universe which has long been inaccessible for observational astronomy. Contrary to other energy bands, where ground-based observatories can be used, X- and gamma-ray observations require space-based technologies. The atmospheric absorption of high-energy photons renders their detection from Earth impossible (Fig. 1.1). Although the challenge of space technologies slowed down the progress in this field of research at first, it has been a rapidly evolving area ever since.

The beginning of extrasolar X-ray astronomy dates back to the year 1962 when a rocket-based X-ray detector (Giacconi et al., 1962) was flown in order to observe fluorescence of the moon's surface from the solar wind. It turned out that the X-ray emission of the moon was below the detection limit of the detector. Instead, scanning the sky with Geiger counters, the rocket experiment discovered the first strong source

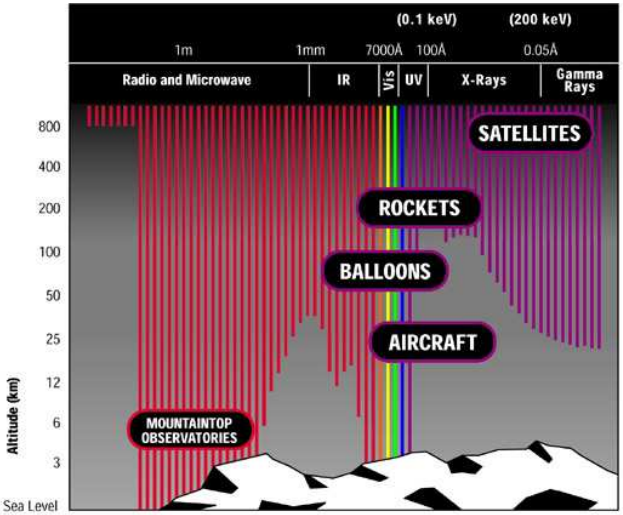

Figure 1.1: Electromagnetic spectrum and atmospheric absorption. The depth of the penetration (i.e. the depth at which the initial intensity has decreased by a factor 1/e) of light at different frequencies into the Earth's atmosphere is shown. The required observatories for the different energy bands are indicated (Image courtesy NASA: `http://chandra.harvard.edu/xray_astro/absorption.html`).

of X-ray emission in space outside the solar system. This source in the constellation Scorpius was later called Scorpius X-1 (Sco X-1), which is a luminous X-ray binary. Data from the discovery observation is shown in Fig. 1.2. Also, for the first time, evidence for an X-ray background radiation in space was provided.

To date, about half a million X-ray sources have been discovered [1]. Most sources were detected by virtue of satellite-based observatories. In 1970, 59 X-ray sources were known from all previous rocket and balloon missions. In 1980, thanks to the *Uhuru*[2] satellite, the British-US observatory *Ariel-V*, and the first High Energy Astronomy Observatory (*HEAO-1*), this number had grown to 700 known sources. Another ten years later, the *Einstein (HEAO-2)* observatory and the European Space Agency's X-ray Observatory (*EXOSAT*) established a list of 8000 sources. The launch of the Roentgen Satellite (*ROSAT*) and its extensive survey program made this number jump up again. In the year 2000, 220000 X-ray sources had been observed, a number which doubled in the following years mainly thanks to source detections by

[1] `http://heasarc.nasa.gov/docs/heasarc/headates/how_many_xray.html`

[2] the Swahili word for 'freedom'; a list of past and present X- and gamma-ray missions is provided, e.g., by NASA at `http://heasarc.nasa.gov/docs/observatories.html`

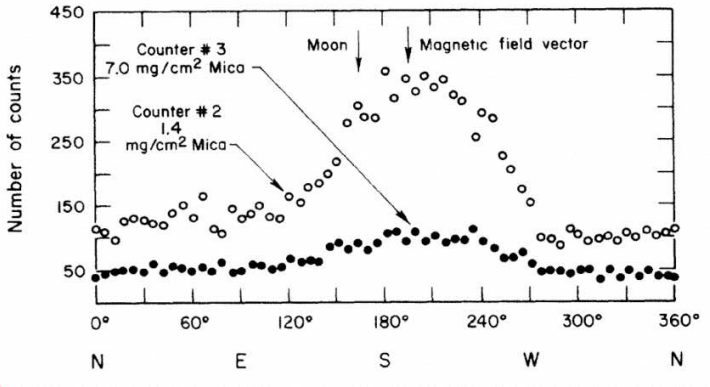

Figure 1.2: Discovery observation of the first extrasolar X-ray source Sco X-1 (Giacconi et al., 1962). The number of counts (accumulated in 350 s in each 6° interval) from two Geiger counters grouped around the longitudinal rocket axis versus the azimuth angle is shown.

the *Chandra*[3] satellite and the X-ray Multi-Mirror Mission (*XMM-Newton*). In 2010, estimates predict that the list of X-ray sources will encompass a million objects.

There is no sharply defined frontier in energy between gamma-rays and X-rays. One commonly speaks of soft X-rays from ~ 0.1–3 keV, of intermediate X-rays from 0.3–10 keV, and of hard or high-energy X-rays from 10 keV to ~ 0.5 MeV. For a general introduction to observational X-ray astronomy, see Charles & Seward (1995).

The high-energy universe is a unique laboratory to observe physics under extreme conditions which are not reproducible on Earth. The title of this thesis, "Strong magnetic fields of accreting neutron stars", hints at some of them. The wording 'strong' refers to fields which are a million times stronger than the largest magnetic field which has ever been produced in a laboratory on Earth. Also, gravitational fields so strong that they bend the escaping light are characteristic for accreting neutron stars. Relativistic quantum electrodynamics is required to discuss the radiation processes in the plasma. The extreme magnetic fields not only give rise to pulsar characteristics but also manifest themselves in the spectra of accreting neutron stars in the form of cyclotron resonance scattering features. As will be explained in detail later in this thesis, these features are formed in absorption due to resonant magnetic photon electron scattering in a relativistic magnetized plasma of quantized electrons. They are observed at energies directly linked to the magnetic field strength. A better understanding of

[3]named in honor of S. Chandrasekhar

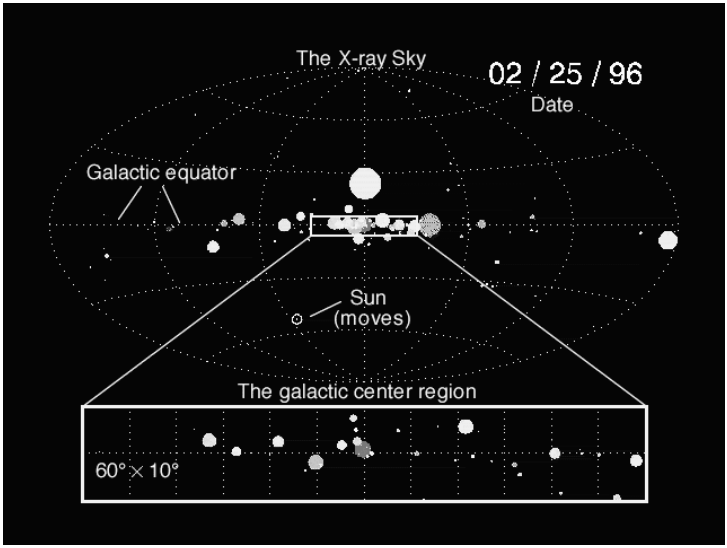

Figure 1.3: The galaxy in X-rays as seen by the Rossi X-ray Timing Explorer (*RXTE*). The big dot above the galactic plane corresponds to Sco X-1. The figure is a snapshot taken from a video released from a group of researchers at the Massachusetts Institute of Technology, led by Hale Bradt.

those features can help to reveal the mysterious nature of magnetized accreting neutron stars. This work is dedicated to the study of their formation in the spectra of accreting X-ray pulsars.

Outline

The outline of the present work is as follows: the next chapter gives an overview over the properties of accreting neutron stars, in particular of the class of accreting X-ray pulsars. It involves the discussion of general neutron star properties, binary dynamics, mechanisms of accretion, timing and spectral properties of those objects. Chapter 3 introduces the focus of this thesis: cyclotron resonance scattering features (CRSFs) in magnetized X-ray pulsar spectra. The basic theory of cyclotron line formation in a strong magnetic field is discussed. Key results from past observations are reported, and an overview of different numerical approaches to modeling cyclotron lines for accreting neutron stars is given. Chapter 4 focuses on the development of a new modeling approach, based on Monte Carlo simulations of the electron photon scattering

processes. Theoretical models are often hard to link to observational results. The precise steps of modeling are therefore motivated in particular from an observer's point of view. Theoretical predictions from the current model in chapter 5 are complemented in chapter 6 by a comparison of the model with real observational data. Finally, chapter 7 summarizes all results. Consequences of these results, relevant for (modeling) X-ray pulsar physics are concluded. Future model developments are anticipated, and an outlook on further approaches to understanding cyclotron resonance scattering features for accreting neutron stars is presented.

CHAPTER 2

Accreting X-ray pulsars

To date, more than 100 accreting X-ray pulsars have been detected (Bildsten et al., 1997; Liu, van Paradijs & van den Heuvel, 2005). X-ray pulsars are bright X-ray sources which exhibit a pulsed luminosity profile. Their observational properties are understood to arise from accretion powered, magnetized neutron stars in close binary systems with a normal star as companion (Pringle & Rees, 1972; Davidson & Ostriker, 1973; Lamb, Pethick & Pines, 1973). Sometimes, the term X-ray pulsar is also used in the literature for isolated, rotationally powered neutron stars or magnetars. Throughout the present work it always refers to accreting binary neutron stars which are the objects of interest of this work. For reviews of observations of accreting X-ray pulsars see, e.g., Nagase (1989), Bildsten et al. (1997) or di Salvo, Santangelo & Segreto (2004).

The first observational discovery of an accreting neutron star binary pulsar took place when regular pulsations in the X-ray energy band were observed from Centaurus X-3 (Cen X-3) by the *Uhuru* satellite (Giacconi et al., 1971a; Schreier et al., 1972, see Fig. 2.1). Shortly after, the same phenomenon was observed by *Uhuru* for Hercules X-1 (Her X-1; Tananbaum et al., 1972). X-ray pulsations had already been seen before in the spectrum of the Crab pulsar. However, Cen X-3 and Her X-1 had comparably slow rotational periods at similar X-ray luminosities, ruling out a rotationally-powered emission mechanism (Davidson & Ostriker, 1973; Ostriker & Davidson, 1973). The findings of their spin-up characteristics (a shortening of their rotation periods) confirmed this deduction. The observational identification[1] of both sources with binary systems instead pointed at accretion as the dominant source of energy. Following the interpretation of Pringle & Rees (1972) for Cen X-3, Davidson & Ostriker (1973) proposed Cen X-3 and Her X-1 to be the prototypes for this new class of accreting X-ray binary systems. Indeed, the high X-ray luminosities could be explained by the liberation of gravitational energy from matter being accreted onto a neutron star. Also, the spin-up rates were understood as a consequence of an angular momentum transfer associated with the accretion of the infalling gas. Many more

[1] from direct observational evidence such at eclipses and Doppler shifts of the pulsation.

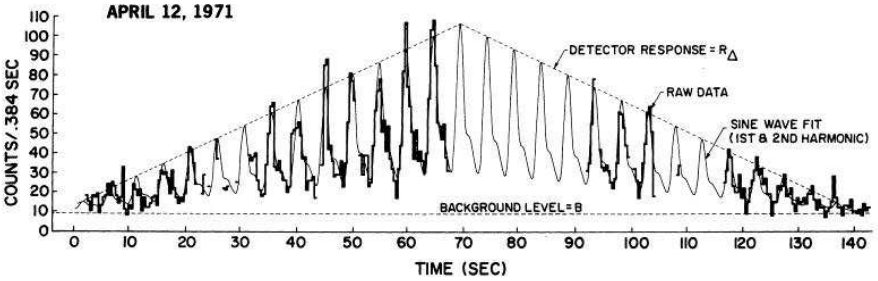

Figure 2.1: Discovery of of pulsations in the light curve of Cen X-3 (Giacconi et al., 1971a). Count histogram for 2–6 keV flux, received on April 12, 1971 by *Uhuru.* A sinusoidal fit to the data is also shown.

observations of X-ray pulsars have strengthened this understanding and contributed to a more complete picture of X-ray pulsars (Nagase, 1989). Accreting X-ray pulsars are believed to have masses of $M \sim 1.3$–$1.8\,M_{\odot}$, radii of $R \sim 10^6$ cm, luminosities of 10^{34}–10^{38} erg s^{-1}, to be spinning with periods of $P = 10^{-2}$–10^3 s, and to possess magnetic fields of the order of 10^{12} Gauss. There are persistent and transient sources which can only be observed (at high luminosities) during outburst events (see section 2.2).

Since the discovery of the first X-ray pulsar, through studies of their spectral and temporal behaviour, the understanding of these sources has increased significantly. In the following, the basic physics of accreting neutron stars is discussed. Different classes of neutron stars, the 'radio pulsars' and 'magnetars' are only briefly touched as a full-blown discussion of neutron star physics is far beyond the scope of this work. This chapter instead aims at a self-contained elaboration of those aspects which are most relevant for understanding the theory and the observational data of cyclotron resonance scattering features in the hard X-ray spectra of strongly magnetized, accreting neutron stars. More general information about neutron stars and compact X-ray binaries can be found for instance in the textbooks by Lewin, van Paradijs & van den Heuvel (1995), Glendenning (1996) or Lewin & van der Klis (2006).

2.1 Neutron stars

"I could be bound in a nut shell and count myself a king of infinite space."

[W. Shakespeare (Hamlet)]

Neutron stars are the compact remnants of massive normal stars with zero-age main

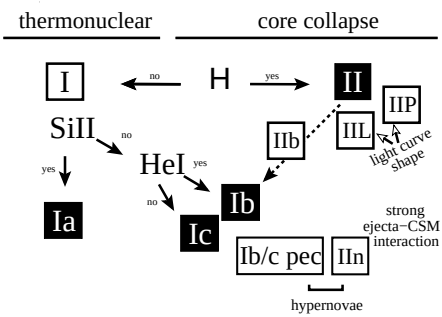

Figure 2.2: Supernova classification. Figure from Turatto (2003). The classification scheme is an extended version of the original spectroscopical distinction of class I (no hydrogen lines) and class II (hydrogen lines) (Minkowski, 1941). SNe are also distinguished with respect to the physical processes of the explosion in thermonuclear SNe and core-collapse SNe.

sequence masses of about 8 to 20–30 $M_\odot$. They are believed to form during a core-collapse supernova (SN) of type II, Ib or Ic (Fig. 2.2). For a review of the evolution and explosion of massive stars, see, e.g., Woosley, Heger & Weaver (2002), for spectroscopical SN classification see Minkowski (1941) and Turatto (2003).

While only $\sim$2000 neutron stars have been detected so far (Lorimer, 2005), estimates predict a number of about 10^8 neutron stars in our galaxy (Timmes, Woosley & Weaver, 1996). First important contributions to the theoretical conception of the neutron star idea came from Chandrasekhar (1931), and Landau (1932), raising the question about the ultimate fate of stars beyond white dwarfs. Shortly after the discovery of the neutron as an elementary particle (Chadwick, 1934), Baade & Zwicky (1934) proposed 'neutron stars' to be formed during a supernova event. First calculations of the neutron stars' structure (Chandrasekhar, 1931; Oppenheimer & Volkoff, 1939) constrained their masses (see table 2.1). The physics of neutron stars are discussed in various textbooks, e.g., Shapiro & Teukolsky (1983) or Lipunov (1992).

Neutron stars are characterized by very high densities, high gravity, fast rotation, and strong magnetic fields. Typical masses are 1.3 to $1.8\,M_\odot$ (see Fig. 2.3 for measured binary radio pulsar masses, Thorsett & Chakrabarty, 1999) compared to radii of the order of 10 km, yielding densities comparable to the densities of atomic nuclei. The exact equation of state for neutron stars, however, remains unknown. The high compactness of neutron stars leads to a surface gravity which is about 10^{11} times stronger than gravity on Earth. The fast rotation of neutron stars is traditionally explained by the conservation of the rotational angular momentum, $L = I\omega$, during the collapse of a normal star's core, where I is the moment of inertia and ω is the angular rotational velocity. The rotational energy increases with the compression as

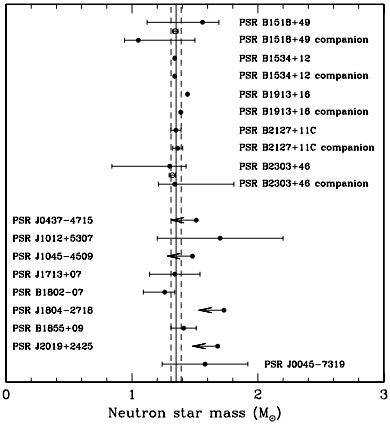

Figure 2.3: Mass measurements of radio pulsars in binary systems (Thorsett & Chakrabarty, 1999). The vertical lines indicate the regime of $M = 1.35 \pm 0.04\,M_{\odot}$.

$E_{\mathrm{rot}} = I\omega^2/2 \propto R^{-2}$ (R is the radius of the object; Lipunov, 1992). Recently, Blondin & Mezzacappa (2007) have suggested that the spin could instead be a result of the explosion itself, breaking with the hypothesis of a correlation of the neutron stars' spin to the spin of the progenitor stars. Similarly, the question whether the strong magnetic fields are linked to the progenitor stars' fields or whether they are generated mainly after the SN explosion is not solved yet (see section 3.1). The surface temperatures of neutron stars are believed to cool from initially about 10^{11} K to temperatures of 10^5–10^6 K on a time scale of less than 1000 years. The cooling is believed to occur via neutrino emission from the whole stellar body and from heat transport to the surface which results in thermal emission of photons. After cooling, neutron stars still exceed the surface temperature of the Sun by three orders of magnitude. For NS cooling theories, see, e.g., Tsuruta & Cameron (1966), Pethick (1992), Page (1998) and Yakovlev & Pethick (2004).

The real nature of the matter compressed within a neutron star and its interior are still highly enigmatic. A simplified model is the picture of a possibly superfluid and superconductive inner core, surrounded by a solid crust, which extends to about 1 km below the surface and contains atomic nuclei in an electron Fermi sea (Harding & Lai, 2006; Jones, 2004). Its composition may be changed by accretion of matter. Models for the interior further involve scenarios of free neutrons at the inner crust ($\rho > 4 \cdot 10^{11}\,\mathrm{g\,cm^{-3}}$), which may form Cooper pairs and turn superfluid below 1 MeV

Table 2.1: Mass constraints on the compact core of the progenitor star which assumes different final evolutionary states (as a WD, NS or BH), after derivations by Chandrasekhar (1931) and Oppenheimer & Volkoff (1939).

Mass	$\lesssim 1.4 M_\odot$	$1.4 M_\odot \lesssim M \lesssim 3$–$4\,M_\odot$	$M \gtrsim 4\,M_\odot$
Object	White Dwarf (WD)	Neutron star (NS)	Black Hole (BH)

and the disappearance of nuclei and the presence of protons, electrons, muons, more exotic particles and strange matter with progressing density in the inner core ($\rho > 2{\cdot}10^{14}\,\mathrm{g\,cm^{-3}}$; Harding & Lai, 2006). In the framework of this work, the macroscopic properties of neutron stars are more important than their inner structure. The observed spectra are dominated by the structure of the atmosphere or outer envelope of the neutron star. However, the inner structure is crucial for the mass-radius relation of the neutron star, which in turn determines the gravitational redshift of the radiation emerging from its surface (see section 2.6).

2.2 X-ray binaries

Accreting X-ray pulsars are neutron stars in binary systems, powering their X-ray emission by the accretion of matter from the companion star (see section 2.3). X-ray binaries contain a normal star and a compact object, orbiting each other. The compact object can be a neutron star or a black hole. The mass function of the system is calculated as a function of the orbital parameters as

$$f(M_\mathrm{P}, M_\mathrm{C}) = \frac{P_\mathrm{orb} v^3}{2\pi G} = \frac{(M_\mathrm{C} \sin i)^3}{(M_\mathrm{C} + M_\mathrm{P})^2}\,, \tag{2.1}$$

where $M_\mathrm{P,C}$ are the masses of the pulsar and the companion star, $x = a \sin i$ is the projected semi-major axis, P_orb is the binary period, i is the system's inclination and v is the observed velocity projected on the sky. The orbital period is obtained from the Doppler variations of the pulsar spin; the amplitude of the radial velocity curve gives x. Orbital periods of hours to months have been observed for accreting X-ray pulsars. For eclipsing systems, also the inclination can be measured ($i \sim 90^\circ$). The relative size of the components of X-ray binaries is illustrated in Fig. 2.4.

X-ray binaries are classified via the mass of the companion or donor star as Low-Mass X-ray Binaries (LMXBs: donor is a late-type star) and High-Mass X-ray Binaries (HMXBs: donor is an early-type star; Shore & van den Heuvel, 1994). Most

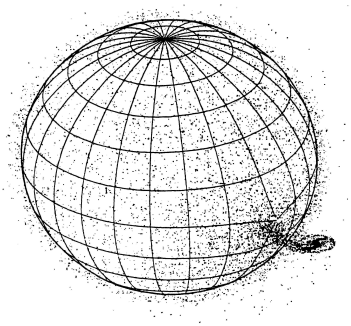

Figure 2.4: Sketch of an accreting X-ray binary. Figure by Dennerl (1991).

accreting X-ray pulsars belong to the class of HMXBs (Mereghetti & Stella, 1995, Fig. 2.5).

Accreting HMXB pulsars contain a donor star of type O or B of a mass $M \gtrsim 10M_{\odot}$. Due to their short lifetimes they contain a young neutron star, and have significantly higher magnetic fields ($\sim 10^{12}$ G) than LMXBs ($\sim 10^{8}$ G). HMXBs accrete from wind accretion, or sometimes from Roche lobe overflow, with the eventual formation of an accretion disk. Section 2.3 gives the details on accretion mechanisms for X-ray pulsars. The optical emission of the system mainly originates from the massive companion star which dominates the energy balance of the system. HMXBs are subdivided into systems containing evolved OB supergiants and into those containing main-sequence Be stars (Bildsten et al., 1997). More than half of the known accreting pulsars belong to the sub-class of Be/X-ray binaries (Bildsten et al., 1997), where the neutron star is in a highly eccentric orbit around its companion (Fig. 2.6). Be/X-ray binaries are observed through transient phases of X-ray outbursts. Two classes of outbursts have been observed: the periodically recurring type I ('normal') outbursts which are associated with accretion during the periastron passage (see Fig. 2.6), and the type II irregular activity with much higher luminosity ('giant outbursts'), observed at arbitrary orbital phases (Bildsten et al., 1997). The first X-ray transient discovered was Cen X-2 (Chodil et al., 1967; Francey et al., 1967). Examples for some long known sources which have recently shown outbursts are the Be/X-ray binaries V0332+53 and A0535+26 (see section 6.2). If the companion star in an evolved HMXB explodes and if the binary system survives this explosion, a double neutron star system may form. To date, there are five to eight detections of double neutron star binaries, the first of them being PSR B1913+16 (Hulse & Taylor, 1975).

LMXBs have a lower magnetic field than HMXBs. With the exception of some sources (Mereghetti & Stella, 1995) they are non-pulsating sources. In LMXBs the

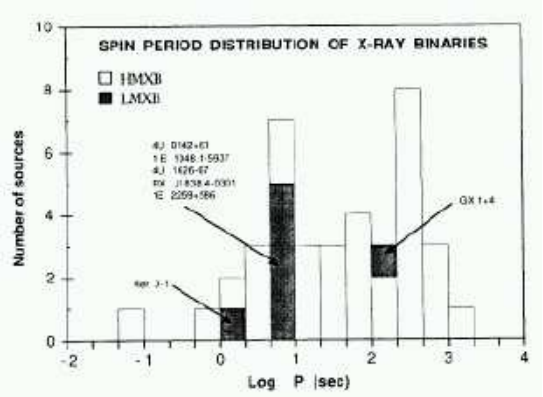

Figure 2.5: Spin period distribution of X-ray binaries (Mereghetti & Stella, 1995) for HMXBs and LMXBs.

companion star is of a type A or later and has a relatively small mass, $M \lesssim 1.2 M_{\odot}$, except for some special cases like e.g. Her X-1 or GX 1+4. LMXBs are typically powered by Roche lobe overflow. In X-rays, their phenomenology is dominated by emission from the compact object and from the accretion disk around it. In the optical waveband, the accretion disk and the X-ray heated surface of the donor star are observed.

X-ray bursts and quasi-periodic oscillations (QPOs) have been observed for several LMXBs (e.g., Lewin, van Paradijs & Taam, 1993; Wijnands, 2001; van der Klis, 2006). One scenario for the bursts are thermonuclear explosions, where accreted hydrogen, helium and carbon accumulate on the neutron star and eventually reach densities which trigger thermonuclear fusion processes, giving rise to a sudden huge energy release (Bildsten, Chang & Paerels, 2003). X-ray bursts have been seen to last from a few seconds to a few hours, exhibiting a peak luminosity of nearly $10^5\, L_{\odot}$. Low frequency QPOs (1–100Hz) and kHz QPOs (0.2–1.3 kHz) are observed as broad peaks in the power density spectra of LMXBs, with centroid energies in the Hz to kHz regime. Beat frequency models (BFMs; Alpar & Shaham, 1985; Lamb et al., 1985; Lamb & Miller, 2001) assume the accretion of local disk inhomogeneities at the magnetospheric radius (see 2.3) and at the sonic radius with a beat frequency to explain QPO signals. In relativistic precession models (RPMs; Stella, 2001), fundamental frequencies of the motion of matter near the neutron star are held responsible for QPOs.

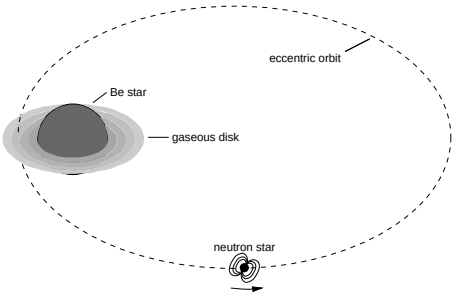

Figure 2.6: Be/X-ray binary system. Accretion with type I outbursts takes place when the neutron star crosses the disk of matter surrounding the Be star during periastron passage (Kretschmar, 1996).

Radio pulsars and magnetars

Accretion is just one of three known sources of energy for steady X-ray emission from neutron stars, the others being rotational energy loss or magnetic field decay. In this section the properties of two representative pulsar populations are discussed briefly: the well-studied class of rotation powered radio pulsars and the very recently established class of magnetars.

The first pulsar, discovered in 1967 by the astronomer Jocelyn Bell (Hewish et al., 1968), was the radio pulsar PSR 1919+21. Remarkably, shortly before this first actual pulsar discovery, Wheeler (1966) had already suggested that the Crab nebula might be powered by the rotation of a central neutron star. Two years later the rotation powered Crab pulsar was also discovered (Staelin & Reifenstein, 1968), supporting the rotating neutron star hypothesis observationally (Gold, 1969), and for the first time proving an association of a pulsar with a SN remnant. To date, around 1700 pulsars are known, biased in their concentration along the galactic plane. For a review, see e.g. Lorimer (2005). The rate of rotational energy loss by spin-down of a neutron star with mass M, radius R, and angular velocity Ω amounts to (Contopoulos & Spitkovsky, 2006)

$$L = \frac{2}{5} M R^2 \Omega \dot{\Omega} \,. \tag{2.2}$$

Rotation powered pulsars have pulse profiles of a more clear-cut and stable shape than the profiles of sources where accretion is involved. The connection between radio pulsars and accreting X-ray pulsars becomes interesting when considering the existence of two distinct populations of rotation powered pulsars: 'Normal' or 'classical pulsars' have observed periods of the order of one second, which increase as $\dot{P} \sim 10^{-15}\,\mathrm{ss}^{-1}$. 'Millisecond pulsars', on the other hand, have been observed spinning as fast as $1.5 \lesssim P < 30\,\mathrm{ms}$ and to spin down slower ($\dot{P} \sim 10^{-19} ss^{-1}$).

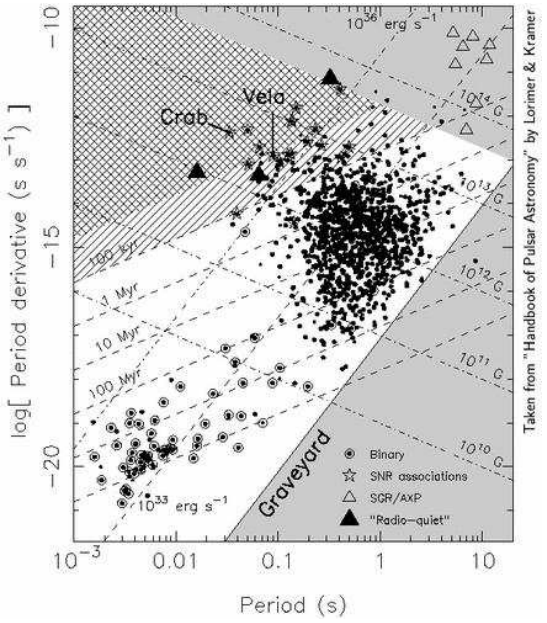

Figure 2.7: Period vs. period derivative diagram for different classes of rotation powered pulsars. Figure from Lorimer & Kramer (2004). The lines of constant magnetic field and age are marked and the region where no radio emission is observed ('graveyard') is indicated (compare Fig. 2.8).

The P-$\dot{P}$ diagram including different classes of rotation powered neutron stars is shown in figure 2.7. A possible scenario for the formation of millisecond pulsars assumes that they are formed in binary systems where they are spun up by accretion processes (compare Fig. 2.8 and Bildsten et al., 1997; Bhattacharya & van den Heuvel, 1991; Lamb & Yu, 2005). However, large differences in the magnetic field strengths $B \propto (P\dot{P})^{1/2}$ (see below) compared to the normal pulsars or the accreting X-ray pulsars still require a better understanding (e.g. Faucher-Giguère & Kaspi, 2006; Contopoulos & Spitkovsky, 2006).

A standard estimate of the magnetic fields of rotation powered, isolated pulsars is obtained via the measurement of their pulse periods, P, and period derivatives, $\dot{P}$, based on calculating the loss of rotational energy $dE_{\rm rot}/dt \propto -B^2\omega^4$, where $\omega = 2\pi/P$ is the angular frequency. The magnetic field is then given by (Bhattacharya &

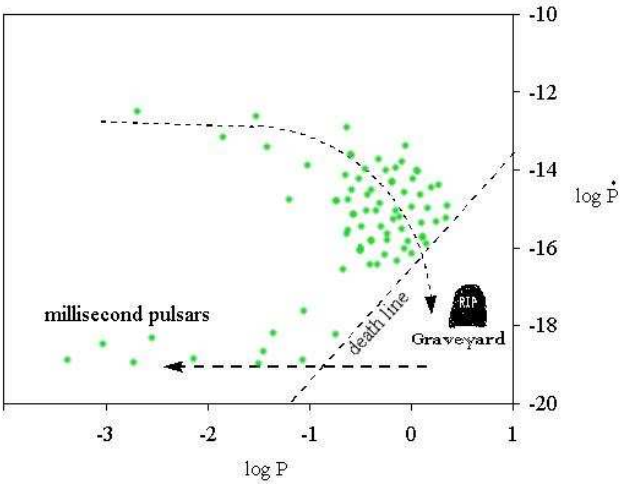

Figure 2.8: Evolutionary scenario for the formation of a millisecond pulsar (`http://www.astro.cornell.edu/academics/courses/astro201/pulsar_graph.htm`). An initially normal isolated pulsar, born as a fast rotator which powers its energy from rotation is observed to slow down until it crosses the 'death line' and its radio emission faints. If member of a binary system, it is spun up again by accretion once its companion has further evolved and ultimately produces a millisecond pulsar.

van den Heuvel, 1991; Ostriker & Gunn, 1969):

$$\frac{\dot{P}}{P} = \frac{8\pi}{3c^3}\frac{1}{P^2}\frac{R^4}{M}B^2\,. \tag{2.3}$$

Equation (2.3) implies magnetic field strengths of 10^{11}–10^{13} G for radio pulsars.

When accretion is involved, such derivations of the B-field are more complicated. Torque theory must be considered as a cause for changes of the period (Ghosh & Lamb, 1979b; Longair, 1981), and gives

$$-\frac{\dot{P}}{P} \propto PL^{6/7}M^{-2/7}R^{12/7}B_{\rm s}^{2/7}\,, \tag{2.4}$$

yielding approximate dipole magnetic field strengths of the order of 10^{12} G. Limits on how much a pulsar can be spun up may be derived from accretion torques, magnetic dipole radiation, and gravitational radiation (Chakrabarty, 2006). From gravitational radiation a limiting frequency was proposed from r-mode oscillation models (Andersson, 1998; Friedman & Morsink, 1998), as $\nu < 700$ Hz (Levin & Ushomirsky,

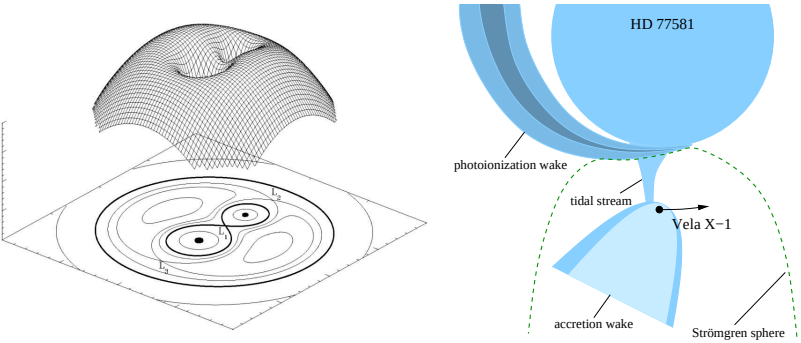

Figure 2.9: Accretion mechanisms in binary systems. Left: three-dimensional representation of the Roche potential of a binary system. Mass transfer occurs via the inner Lagrange point L_1. Figure from `http://www.astro.uu.nl/~sluys/Hemel/Informatie/Sterren/hoofdstuk6.html`. Right: Stellar wind accretion. Sketch of Vela X-1 (P. Kretschmar and J. Wilms, priv. com.).

2001). However the fastest spinning, securely detected pulsar presently known, which is a pulsar in the Terzan 5 globular cluster named PSR J1748-2446ad (Hessels et al., 2006), spins at 716 Hz, exceeding this limit. Gravitational wave studies are expected to shed more light, e.g., on the r-mode theories and on the possibility of the existence of pulsars with even shorter pulse periods (Hessels et al., 2006). Very recently, Kaaret et al. (2007) have even claimed the detection of 1122 Hz oscillations during an X-ray burst of the X-ray transient XTE J1739−285.

Magnetars are the most recently established class of neutron stars. The term 'magnetar' refers to a neutron star with an ultra-strong, supercritical[2] magnetic field of the order of 10^{14}–10^{15} G. The existence of magnetars was proposed by Duncan & Thompson (1992). Meanwhile, various magnetar sources have been detected to confirm their idea. A field strength of the order 10^{15} Gauss was claimed from the detection of a proton cyclotron scattering feature in the soft gamma ray repeater (SGR, Kouveliotou et al., 1998, 1999) SGR 1806−20 (Ibrahim et al., 2002, see section 3.3). Two classes of neutron stars, the anomalous X-ray pulsars (AXPs, see e.g., Mereghetti, 2001) and the SGRs are today believed to belong to this one class of objects (Woods & Thompson, 2006). AXPs were called this way because of their long not understood mysterious nature compared to X-ray pulsars. SGRs are gamma ray emitters believed to

[2]compared to the quantum critical field, $B_{\rm crit} \sim 44.14 \cdot 10^{12}$ G (see later).

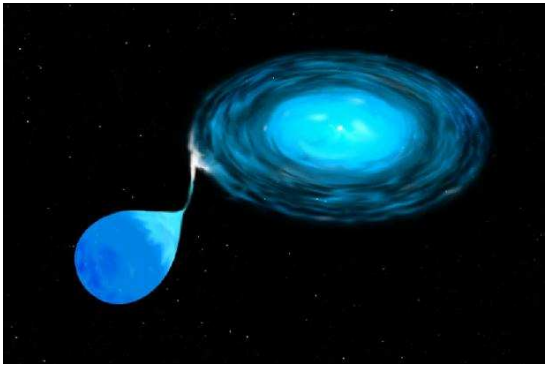

Figure 2.10: Artist's impression of an X-ray binary with the formation of an accretion disk (`http://hea-www.harvard.edu/~psr_snr/images/xrb.jpg`).

have extremely soft spectra, although recently hard X-ray components were detected in *INTEGRAL* data for both SGRs and AXPs (Mereghetti et al., 2005; Götz et al., 2006, 2007). Meanwhile a scenario has evolved in which a magnetar is believed to evolve from an initial SGR status to an AXP (Wilson, 2006).

2.3 Accretion mechanisms

"How is it that the sky feeds the stars?"
[Lucretius]

X-ray pulsars are literally fed by the accretion of matter from their companion star which is transferred onto the neutron star. Accretion is a very efficient mechanism of energy production, liberating an amount of energy ($\Delta E_{\rm acc} = GM\Delta M_{\rm acc}/R$) of typically 10^{20} ergs for each accreted gram of matter (for $M = 1\,M_\odot, R = 10\,$km). The mass accretion rate, $\dot{M}$, determines the luminosity of the system,

$$L = \frac{GM}{R}\dot{M} \sim 0.1\dot{M}\,. \tag{2.5}$$

Typical mass accretion rates are 10^{-11}–$10^{-9}\,M_\odot\,{\rm yr}^{-1}$; an upper limit on the mass accretion rate was estimated by Ostriker & Davidson (1973) as $10^{-7}\,M_\odot\,{\rm yr}^{-1}$. The maximum luminosity by accretion is reached when the radiation pressure equals the gravitational pressure of the star. For spherically symmetric accretion, one speaks of

the Eddington luminosity,

$$L_{Edd} = \frac{4\pi GM(m_{\rm p} + m_{\rm e})c}{\sigma_T} = 3.23 \cdot 10^4 \frac{M}{M_\odot} L_\odot \,. \tag{2.6}$$

X-ray pulsars with super-Eddington luminosities have been observed. This does not violate the pressure balance if one considers non-spherical accretion, which is expected for strong magnetic fields (see below).

When modeling accretion, the relevant scale to consider is the distance from the neutron star surface. At large distances, gravity dominates and magnetospheric stresses may be neglected. The distance is parameterized by the magnetospheric or Alfvén radius, denominating the radial distance where the ram pressure of the accretion flow equals the magnetic pressure. Inside the Alfvén surface magnetospheric effects dominate accretion.

2.3.1 Distant accretion flow

The mass transfer from the donor star towards the neutron star obeys different mechanisms for distinct system properties. The basic type of mechanism is determined by the distance at which gravitational capture of the matter by the neutron star takes place, and by its mean specific angular momentum at that distance. Close binaries are powered by Roche lobe overflow: matter directly streams from the companion star towards the compact object by crossing the inner Lagrange point of the effective gravitational potential ('Roche potential', see, e.g., Kopal, 1989, and Fig. 2.9, left), once the donor star has filled its Roche lobe. Strictly speaking, the Roche potential gives the effective potential of a binary containing two point masses in the corotating frame

$$F^{\rm Roche}(\vec{r}) = -G\frac{M_1}{|\vec{r} - \vec{r}_1|} - G\frac{M_2}{|\vec{r} - \vec{r}_2|} - \frac{1}{2}\left(\vec{\Omega} \times \vec{r}\right)^2 \,, \tag{2.7}$$

where M_1, M_2, $\vec{r}_1$ and $\vec{r}_2$ are the masses and positions of the components and $\vec{\Omega}$ is the angular velocity. Angular momentum is preserved and an accretion disk may form (Fig. 2.10).

In systems where the companion star has a strong stellar wind, matter can be accreted directly from this wind (Fig. 2.9, right). This mechanism was sometimes called quasi-spherical accretion but is today believed to be mostly focused wind accretion from a tidal stream. Observations of such systems are strongly influenced by absorption of radiation by this wind. Blondin (1994) and Blondin & Woo (1995) proposed a shadow wind and an X-ray excited, thermally driven wind component and visualized the complex velocity field structures of the binary systems. They simulated the stellar wind hydrodynamics for the luminous X-ray binaries Cen X-3 and SMC X-3. An

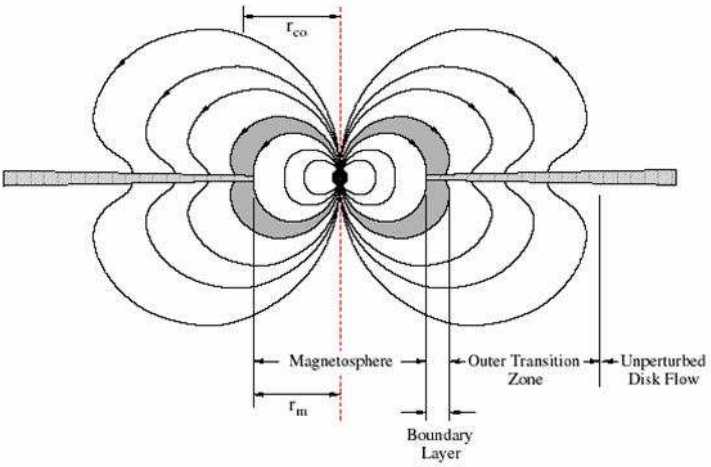

Figure 2.11: Accretion regimes (Ghosh & Lamb, 1978), schematically depicted for disk accretion. The corotation radius, $r_{\rm co}$, marking the distance where the angular velocity of the magnetosphere is equal to the Keplerian gas velocity, and the magnetospheric radius, $r_{\rm m}$ (see text), are indicated.

example for a strong wind accretor is Vela X-1 (compare section 6.2). The wind structure can be inferred from a rapidly varying light curve which is traced to variations of the absorbing column along the line of sight.

2.3.2 Magnetospheric accretion

Close to the neutron star surface, regardless of the distant accretion scenario assumed, the flow of matter is dominated by the strong magnetic field of the neutron star (Fig. 2.12). One speaks of magnetospheric accretion. For a far-field of a dipole $B_r(r) = (R/r)^3 B_{\rm s}$, the magnetospheric pressure decreases with the distance from the neutron star center r as

$$P_{\rm mag} \propto \left(\frac{R}{r}\right)^6 B_{\rm s}^2 \,, \tag{2.8}$$

where B_s is the surface magnetic field at $R = r$. Inside the magnetosphere its value becomes comparable to the ram pressure in the flow of matter. Lamb, Pethick & Pines (1973) determined the inner magnetospheric radius or Alfvén radius, $r_{\rm A}$, for radial infall from equating the energy densities of the magnetic field and the infalling matter,

$$\rho v_r^2(r_{\rm A}) = B_r^2(r_{\rm A})/(8\pi) \,, \tag{2.9}$$

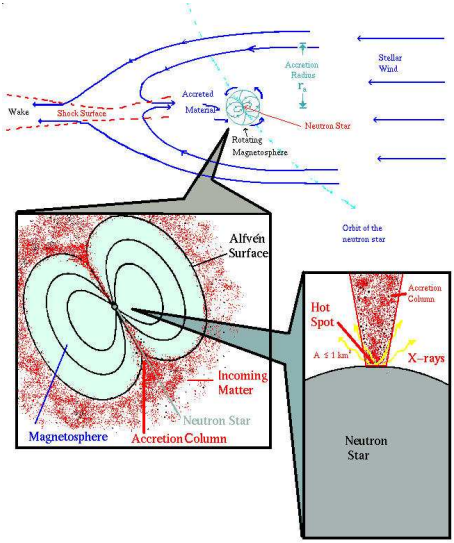

Figure 2.12: Magnetospheric accretion. Courtesy: I. Neguerela, based on Davidson & Ostriker (1973).

where the density of accreting matter is given by the continuity equation

$$\dot{M} = 4\pi r^2 \rho v_r \,. \tag{2.10}$$

The mass accretion rate is obtained from the luminosity by equation (2.5). Assuming that the velocity of the infalling matter equals the free-fall velocity

$$v_{\rm ff} = \sqrt{2GM/r}\,, \tag{2.11}$$

the Alfvén radius is obtained as

$$r_A = \left(\frac{B_s^4 R^{12}}{8\dot{M}^2 MG}\right)^{1/7} \propto 10^8 \cdot B_{12}^{4/7} R_6^{10/7} (M/M_\odot)^{1/7} L_{37}^{-2/7}\,, \tag{2.12}$$

where B_{12} is the magnetic field in units of 10^{12} G, $R_6 = R/10^6$ cm and $L_{37} = L/10^{37}$ erg s^{-1}. Typical neutron star parameters give $r_A \sim 10^3$ km $\sim$100 R. For the study of cyclotron lines it is important to stress that this value is far above the typically assumed height of the line forming region which is either placed at the surface or below a radiative shock front (Basko & Sunyaev, 1976; Becker, 1998). Therefore the mechanisms of accretion beyond the magnetosphere are less relevant for the study

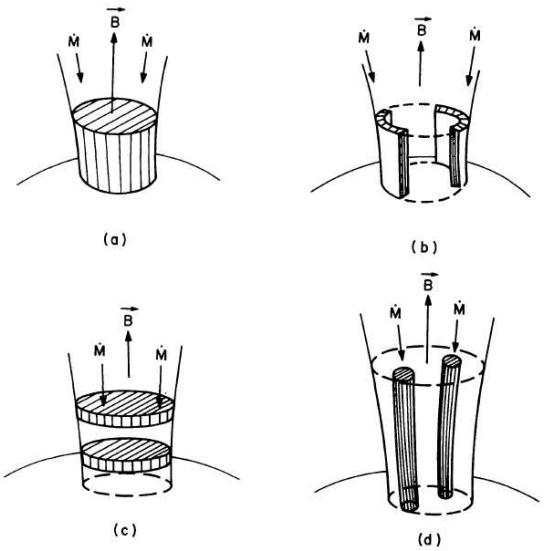

Figure 2.13: Scenarios of filling the accretion column. Filled column, hollow column, 'blob'- and 'spaghetti'-like structures. Fig. 11 from Mészáros (1984).

of cyclotron lines later in this thesis. Primarily, the processes inside the Alfvén surface have to be considered. Inside the Alfvén surface, the matter is funneled along the field lines onto the magnetic poles (Basko & Sunyaev, 1976). Free-fall velocities of the order of $\sim 0.5\,c$ can be reached. The concentration of the field lines towards the magnetic poles results in the formation of 'accretion columns' above the magnetic poles ('polar caps','hot spots') of the neutron star. Simple estimates of the radial extension, $r_{\rm cap}$, of those hot spots for the case of dipolar magnetic fields (Davidson & Ostriker, 1973) give $r_{\rm cap} = R^{3/2} R_{\rm A}^{-1/2} \sim 0.8\,$km. However, those are only rough estimates, and the real nature and dimensions of the accretion column or accretion mound is still an unsolved mystery. Hollow funnels, filled columns, and partially hollow columns have been proposed by different theoreticians. Early work by Mészáros (1984) on the filling geometry of the accretion column is shown in Figure 2.13. The filling of the column may indeed by linked to the type of distant accretion which decides on the way the matter couples to the field lines at the magnetospheric radius. The gas which couples to the field lines is thought to have temperatures of a few keV and to further cool down by radiation during its fast approach of the surface. Close to the surface, the infalling gas is suddenly stopped. Inverse Comptonization of soft photons in the decelerated plasma produces photons in the X- and gamma ray regime.

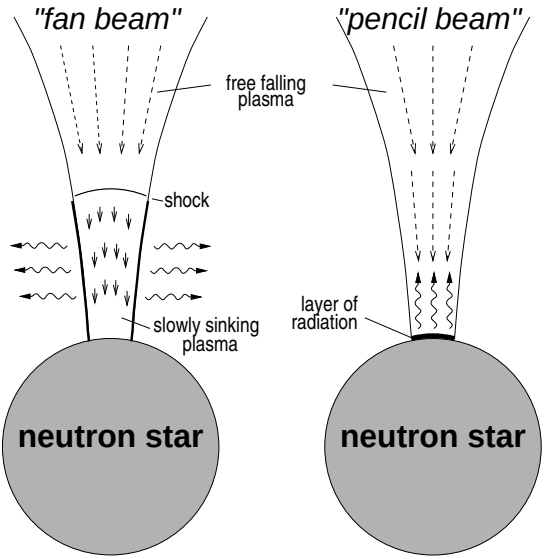

Figure 2.14: Simplified emission patterns. Left: 'fan beam' scenario. Right: 'pencil beam' scenario. Figure from Kretschmar (1996).

The emission characteristics of this radiation depends on the mass accretion rate, $\dot{M}$. For large $\dot{M}$, a shock front develops at some distance from the neutron star surface, which does not permit the upscattered photons to escape vertically from the accretion column, i.e., parallel to the B-field. As a result, a 'fan beam' emission pattern forms (Fig. 2.14, left). As was first shown by Basko & Sunyaev (1976), the critical luminosity for shock formation, L^*, is

$$L^* = 2.72 \cdot 10^{37} \left(\frac{\sigma_{\mathrm{T}}}{\sqrt{\sigma_{||}\sigma_{\perp}}} \right) \left(\frac{r_0}{R} \right) \left(\frac{M}{M_{\odot}} \right) \text{ erg s}^{-1} , \qquad (2.13)$$

where r_0 is the polar cap radius, σ_{T} is the Thomson scattering cross section and $\sigma_{||}$ and $\sigma_{\perp}$ are the energy averaged cross sections for the scattering of photons which propagate in parallel and perpendicular to the magnetic field direction (see Becker, 1998, and section 3.4). For small $\dot{M}$, on the other hand, i.e., for $L < L^*$, the radiation is emitted from an accretion mound such that most photons are emitted parallel to the B-field in a 'pencil beam' pattern (Fig. 2.14, right).

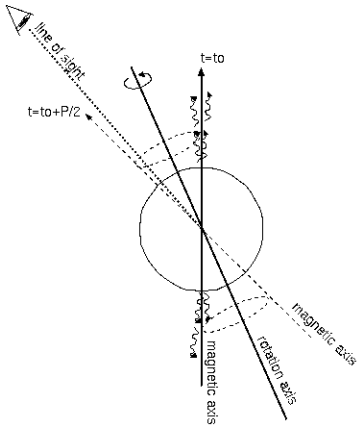

Figure 2.15: Lighthouse effect: when the rotation axis of a neutron star is not coaligned with the magnetic axis, the observer sees 'flashes' or pulses of light.

2.4 Pulsar mechanism and pulse profiles

The timing analysis of astrophysical sources is based on the analysis of their light curves, i.e., the detected source flux in a chosen energy band as a function of time. Light curves of X-ray pulsars are of clearly periodic nature. The periodicity of their flux variations, observed as pulsed emission, has initially motivated the term 'pulsar'. The emission characteristics of pulsars are caused by the neutron stars' strong magnetic fields which induce a beaming of the emergent radiation along or at a certain angle to the magnetic field vector. For X-ray pulsars different accretion scenarios inducing beamed emission have been described in section 2.3. An observer of a fast spinning neutron star for which the magnetic axis is not coaligned with its rotational axis (Wang & Welter, 1981), will detect pulses of radiation whenever one of the light beams hits his line of sight. This mechanism is commonly named the 'lighthouse effect' (Fig. 2.15).

Compared to isolated pulsars, accreting X-ray pulsars have a rather large duty cycle, $\gtrsim 50\%$. Their pulses are relatively broad such that they are predominantly seen in a high flux state. The pulse periods which have been determined for X-ray pulsars span a broad range from 10^{-2} to 10^{3} s. Folding the light curve of a source with its pulse period, one obtains a characteristic pulse profile for one period cycle. Its shape is representative of the flux dependence on the phase of rotation. The spectral properties may change dramatically with the phase. The pulse profile is the basic tool to perform and to interpret phase resolved spectroscopy. The formation of the complex structures and substructures of pulse profiles from accreting neutron stars, however, renders their

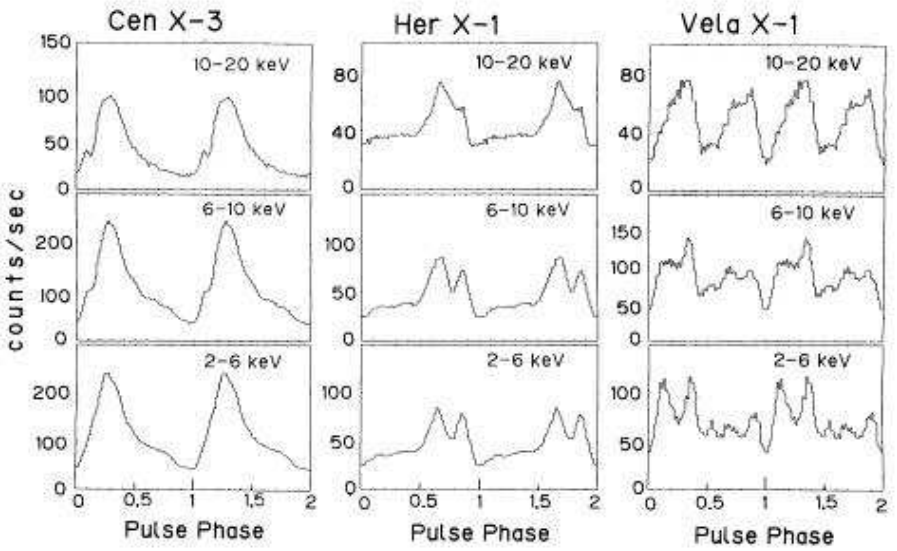

Figure 2.16: Pulse profiles for Cen X-3, Her X-1 and Vela X-1 from classical *Ginga* results (Nagase, 1989). The morphology of the pulse profiles varies for different sources and depends on the energy band of the observed flux. For more recent results, see, e.g., La Barbera et al. (2003), Kuster et al. (2002) and Bildsten et al. (1997).

interpretation a difficult task. The profiles vary significantly from source to source. Their morphology usually is also strongly dependent on the energy band chosen (see Fig. 2.16). They may change from one observation of a source to the next, possibly indicating a change in the source's geometry. Pulse shapes of quasi sinusoidal nature, asymmetric character, double-peaked structure or even five-peaked pulses have been found for various sources observed at different energy bands. A strong dependence of the opacity of the X-ray emitting region on angle and frequency yields a strongly anisotropic radiation pattern. The analysis of pulse profiles can probe the structure of the magnetosphere and the beam pattern (Wang & Welter, 1981; Blum & Kraus, 2000). Mészáros & Nagel (1985a) tried to infer the geometry of the accretion column from simulations of a set of pulse profiles. They pointed out that pulses simulated for fan beam scenarios seem to be too broad when comparing them to observational data and concluded that the phase dependence of the observed spectra fitted better with a pencil beam scenario. Mészáros & Riffert (1988) also pointed out, however, that a fan beam might appear as a pencil beam to a distant observer due to gravitational light bending (see later).

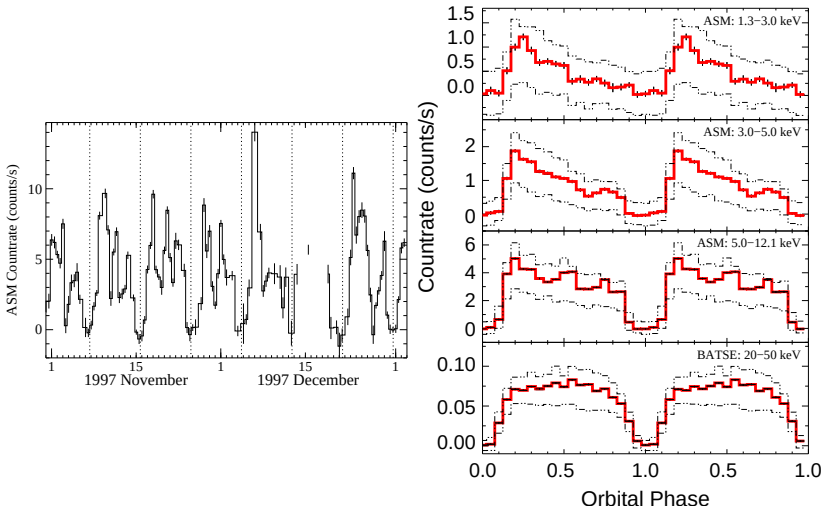

Figure 2.17: Light curve and orbital profiles for the stellar wind accretor Vela X-1. Left: Light curve (3–10 keV) detected by ASM on RXTE of Vela X-1 observed during two months (Nov–Dec 1997) is shown (J. Wilms, priv. com.) . Right: Orbitally and energy resolved profiles for the same observation by ASM and BATSE. The shape of the profiles changes with the energy range considered (J. Wilms, priv. com.).

Long-term history observations of X-ray pulsars have revealed the existence of medium and long term periodicities. Furthermore, systematic, secular changes of the pulse periods with the time are observed. On orbital time scales (typically days), the change in the flux can be attributed to the orbital period (see Fig. 2.17). Additional long-period variations of the flux have been detected for Her X-1, LMC X-4, and SMC X-1, among other sources (Levine & Jernigan, 1982; Staubert, Bezler & Kendziorra, 1983; Levine et al., 1991; Boyd & Smale, 2000; Boyd & Still, 2004; Boyd, Still & Corbet, 2004; Staubert et al., 2006; Klochkov et al., 2006). Secular changes of the pulse period mark its long-term variability. An overall shortening of the period (spin-up trend) is expected from the gain of angular momentum during the accretion process, which is transferred from the infalling matter to the neutron star. A disk-accreting pulsar experiences a spin-up torque, $N \sim \dot{M}\sqrt{GMr_{\mathrm{A}}}$ (Bildsten et al., 1997), which is also an upper limit for wind accretion. However, also the opposite effect, i.e., a lengthening of the period or spin-down trend has been observed for some sources, and spin-down and spin-up trends have also been found to alternate, often with a slow overall spin-up trend superposed (Bildsten, Chang & Paerels, 2003). Analyses of the spin-up and spin-down morphologies of X-ray pulsars probe their ac-

cretion mechanisms. While long-term spin-up/spin-down reversals are connected to the accretion torques (e.g., Fritz et al., 2006), shorter stochastic alternations may be associated with internal torques from crust to core interactions of the neutron star. First limiting frequencies were proposed from magnetospheric accretion analysis (Ghosh & Lamb, 1979a). Another mechanism to arrest the accretion torque spin-up could be angular momentum loss from gravitational rotation (Bildsten, 1998; Bildsten, Chang & Paerels, 2003).

2.5 Spectral properties

The phenomenology of X-ray pulsar continua can be roughly described by a power law ($\alpha \sim 1$) with an exponential high-energy rolloff (White, Swank & Holt, 1983; Tanaka, 1986). At energies below a tenth to a few keV, the spectrum is absorbed by the interstellar medium. At a few keV, most spectra exhibit also absorption features from metals in the interstellar gas or accretion flow. A 6.4–6.8 keV iron emission line is often observed. It indicates different ionization states of the matter, and is believed to form due to iron fluorescence transitions (Ohashi et al., 1984) in parts of the plasma which are probably located further out and which are cooler than the surface emission region. At intermediate energies, harmonic absorption features are observed in more than a dozen X-ray pulsars: cyclotron resonance scattering features. Being the focus of this work, their formation and their shapes will be discussed in a fully dedicated chapter (chapter 3) while this section focuses on the continuum component of X-ray pulsar spectra. Some older spectra for some different X-ray pulsars (Nagase, 1989) are depicted in Fig. 2.18; an example of a more recent broad-band spectrum observed by *Beppo-SAX* (A. Santangelo, priv. com., after dal Fiume et al., 2000) is shown in Fig. 2.19.

There are different phenomenological models in use for the observational analysis of X-ray pulsars. Neglecting, for the moment, low-energy absorption and any line features, the most simple model which qualitatively describes X-ray pulsar spectra at hard X-rays is an exponentially cutoff power law of the form

$$F(E) = A \cdot E^{-\alpha} \exp\left(-E/E_{\text{fold}}\right), \tag{2.14}$$

with the free parameters giving the power law normalization, A, the photon index, α, and the folding energy, E_{fold}. Often, when considering real observational data, however, more complex continuum models like, e.g. a power law with a Fermi-Dirac cutoff (Tanaka, 1986),

$$F(E) = A \cdot E^{-\alpha} \left[\exp\left(\frac{E - E_{\text{cut}}}{E_{\text{fold}}}\right) + 1\right]^{-1}, \tag{2.15}$$

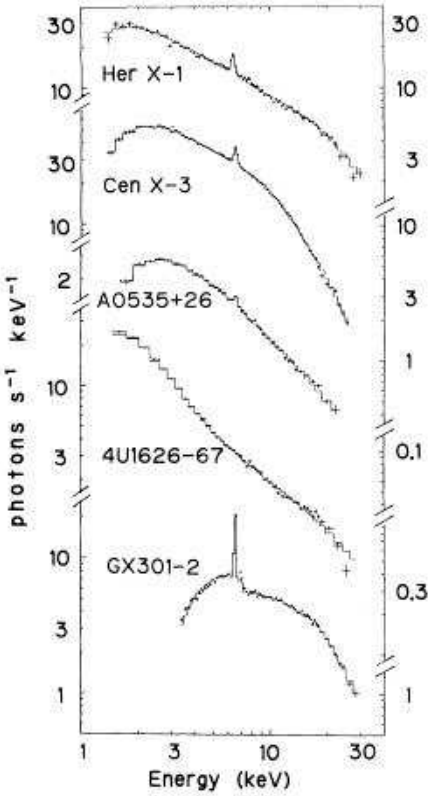

Figure 2.18: Phase-averaged energy spectra of five X-ray pulsars observed by Temma (Nagase, 1989) between April 1983 and April 1984.

a power law with a high-energy cutoff,

$$F(E) = AE^{-\alpha} \cdot \begin{cases} \exp\left(\frac{E_{\text{cut}}-E}{E_{\text{fold}}}\right) & \text{if } E \geq E_{\text{cut}} \\ 1 & \text{otherwise} \end{cases} , \tag{2.16}$$

or the 'npex' model (Mihara, 1995; Makishima et al., 1999), a negative and positive power law with a common high-energy cutoff,

$$F(E) = A(E^{-\alpha_1} + f \cdot E^{+\alpha_2}) \exp\left(-\frac{E}{E_{\text{fold}}}\right) , \tag{2.17}$$

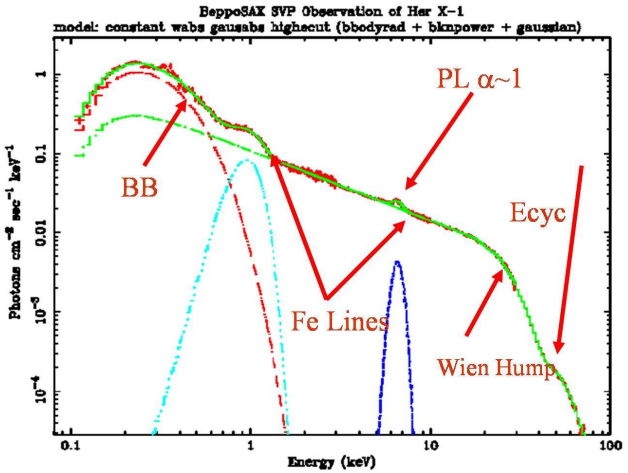

Figure 2.19: Broad-band *BeppoSAX* photon spectrum of Her X-1 (A. Santangelo, priv. com., based on dal Fiume et al. (2000). The colors indicate different spectral components.

are used. To date no model has been found to be favorable from a systematic study and a physical interpretation of the phenomenological fit parameters remains difficult. The necessity of a smooth transition between the power law and the exponential cutoff to avoid line-like features in the fit has been discussed by Kretschmar et al. (1997) and Kreykenbohm (2004).

Attempts to numerically or analytically derive the shape of X-ray pulsar spectra have been numerous (e.g. Mészáros, 1978; Nagel, 1980, 1981b,a; Mészáros et al., 1983; Mészáros & Nagel, 1985a,b; Burnard, Klein & Arons, 1988; Burnard, Arons & Klein, 1991; Becker, 1998; Becker & Wolff, 2005). However, no self-consistent, general model could be established due to the uncertainty of the highly complex underlying physics and structure of the accretion column and magnetosphere. Observers are therefore still restricted to interpret data with phenomenological approaches, like outlined above. There has been some renewed effort emerging recently for understanding the continua from physical radiation processes (Becker & Wolff, 2005, 2007). The state-of-art of modeling X-ray pulsar continua is represented by the work of Becker & Wolff (2007). They discussed the formation of the continuum emission from an accretion column accounting for bulk motion of the matter in the line forming region and considering a Comptonization scenario. Becker & Wolff (2007) proposed a velocity flow of the matter in the column which corresponds to stopping of the accre-

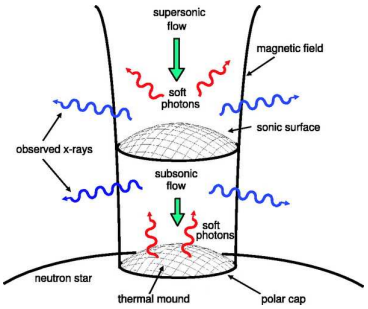

Figure 2.20: Schematic depiction of the seed photon production in the accretion column. Photons are produced by bremsstrahlung and synchrotron emission throughout the column and from a blackbody component from the surface of a thermal mound (Becker & Wolff, 2007).

tion flow in a radiation-dominated shock (Becker, 1998). This approach limits their discussion to luminous X-ray sources where the formation of this type of shock is expected. These authors calculated the response of the accretion column to the seed photons through Green's functions for the continuum formation. The seed photons (i.e., up-scattered soft photons) were assumed to originate from bremsstrahlung and synchrotron radiation from within the column, and from blackbody radiation from the bottom of the column (see Fig. 2.20). The photons then diffuse spatially outwards while undergoing thermal and bulk Comptonization processes. Folding the initial seed components with the Green's functions response, Becker & Wolff (2007) obtained the final contributions from the different seed radiation processes to the total spectrum. Fitting their model parameters to published phase-averaged spectra of the three sources Cen X-3, LMC X-4 and Her X-1 (for Her X-1, see figure 2.21), they obtained a qualitative agreement with the observational data. The authors found a strong predominance of the bremsstrahlung component for all sources. The cyclotron absorption features were only included in an approximate way.

2.6 Gravity

"Do not bodies act upon light at a distance,
and by their action bend its rays;
and is not this action (caeteris paribus) strongest at the least distance?"
[I. Newton in Opticks, 1704]

The high compactness of neutron stars implies that relativistic effects are relevant.

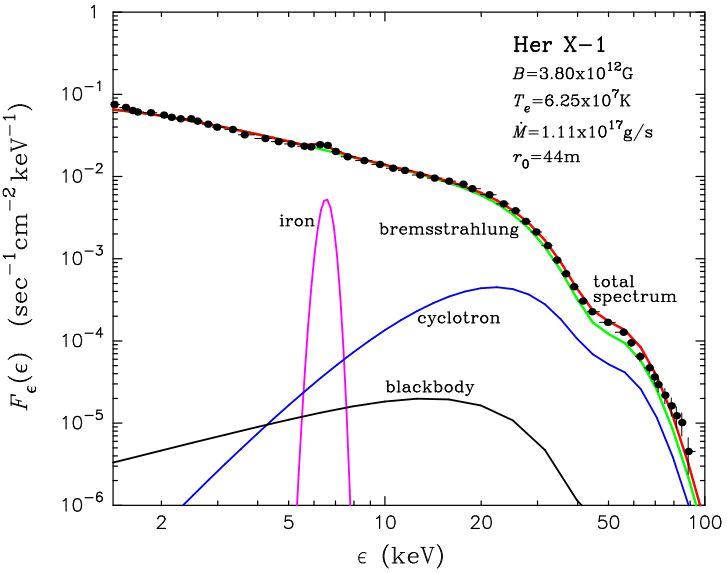

Figure 2.21: Theoretical X-ray pulsar spectrum fitted to Her X-1 by Becker & Wolff (2007). The individual components of the continuum spectrum are shown, where a cyclotron line feature is approximately included. The bremsstrahlung component strongly dominates the total spectrum. The component which is indicated as 'cyclotron' emission is most commonly called synchrotron radiation; the latter terminology is the one adopted in this work.

Radiation from X-ray pulsars is therefore observed at gravitationally redshifted energies. A distant observer sees the light which is emitted at a certain wavelength λ from the neutron star's surface at a longer wavelength $\lambda + \Delta\lambda$. The relative displacement implicitly defines the gravitational redshift,[3] $z = \Delta\lambda/\lambda$. For neutron stars, the surface gravitational redshift is usually approximated by the formula for a non-rotating, uncharged, spherically symmetric mass in the Schwarzschild spacetime as

$$z = \frac{1}{\sqrt{1 - R_\mathrm{S}/R}} - 1\,. \tag{2.18}$$

[3]More than two centuries ago, Michell (1784) already proposed that light from high-gravity stars would be weakened, based on Newton's conception of light deflection by gravity (Newton, 1704). Effects of gravity on light were further discussed by Laplace (1796), who predicted the existence of Newtonian black holes, which he named 'dark stars', Soldner (1804), who proposed that the gravitational effect on light would introduce a bending of light by massive objects, and independently by Einstein (1911) as part of his theory of general relativity. Today, with the confirmation of the existence of black holes, and with direct observations of gravitational lensing, the gravitational redshift and light deflection are well-established phenomena in astronomy and cosmology.

$R_S = 2GM/c^2$ is the Schwarzschild radius, given by the gravitational constant G, the speed of light c and the mass M of the gravitational source with radius R. For the canonical NS mass ($M = 1.4\,M_\odot$), $R_S \sim 4.5$ km. For X-ray pulsars, z is needed for an unambiguous determination of their surface magnetic fields from cyclotron line detections, as the observed energies of the CRSFs scale both with B and $1/(1+z)$ (compare eq. 3.1, and see section 3.2). Unfortunately, different models for the interior structure of neutron stars (see section 2.1) currently lead to very different equations of state $M(R)$, corresponding to different values of z, which observers are challenged to measure from atomic or spectral lines[4]. As long as no unique M-R relation is known for X-ray pulsars, a reasonable range for the redshift can be obtained by solving equation (2.18) for typical neutron star masses $M = 1.3$–$1.8\,M_\odot$ and radii $R \sim 1$–$1.5\,R_6$ ($R_6 = 10^6$ cm). Eq. (2.18) yields the rather large range of $z = 0.16$–0.46 for the gravitational redshift of neutron stars. Usually, observers assume $M/M_\odot = 1.4, R_6 = 1$, corresponding to $z \sim 0.3$ for the spectral analysis of X-ray pulsars.

Light deflection bends the orbits of the photons radiated from the surface of a neutron star and increases its surface visibility. This effect is important for the understanding of its emission characteristics, in particular when analyzing pulse profiles which result from gravitationally bent beam patterns (Blum & Kraus, 2000). The effect of gravitational light bending can be assessed quantitatively by calculating the orbit of a single photon. The Schwarzschild metric can be used for solving the geodesic equations for a photon's four momentum to obtain its trajectory in the Schwarzschild coordinates t, r, θ, ϕ (Kraus, 1998). Choosing as convention the equatorial plane for

[4]For some sources, such measurements have been realized. Cottam, Paerels & Mendez (2002) determined the redshift from the energy displacement of photospheric absorption lines in the X-ray burst spectra of the LMXB EXO 0748−676 as $z = 0.35$. However, this method premises that (a) spectral lines are resolved, and (b) that one knows for certain the nature and initial energy of those lines. Bildsten, Chang & Paerels (2003) proposed to confirm this redshift measurement by also considering Fe abundances and spallation. From a calculation of the exact line profiles, accounting for the star's spin and full relativistic effects, Bhattacharyya, Miller & Lamb (2006) predicted a theoretical accuracy of 5 % for the determination of M/R even for broad and skewed lines. If no suitable spectral lines are found, estimates of M and R by other means have to be sought to vice versa estimate the gravitational redshift of the star. Independent determination of M and R in any case requires an approach beyond the redshift measurements. Recently, Zhang et al. (2007) presented three approaches to access the M-R relation for neutron stars, including the redshift determination. The other two methods are the determination of the apparent radius from the blackbody luminosity and blackbody temperature and the analysis of kHz quasi periodic oscillations. The authors point out that any two of these three methods would in principle suffice to determine M and R independently for sufficiently good measurements of the corresponding quantities. They propose approximate constraints for the masses and radii of three sources: 1E 1207.4−5209, Aql X-1 and EXO 0748−676, implying redshifts of $z \sim 0.1$–0.4, and suggest possibly corresponding types of equations of state for the interior neutron star structures. Approaches to measure neutron star masses and radii are manifold, extending from simple considerations on binary dynamics to gravitational wave studies.

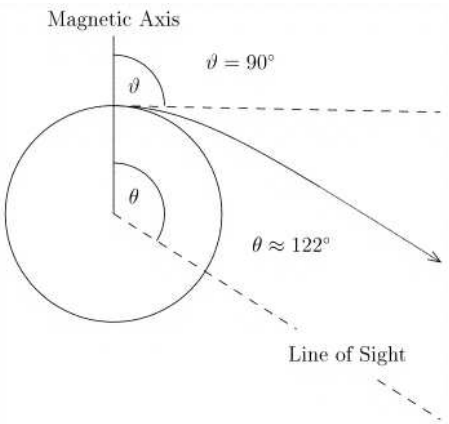

Figure 2.22: Light deflection by a neutron star. The effect on a photon emitted perpendicular to the magnetic axis of the neutron star at one pole is shown, as observed by an observer at a large distance, for $R/R_{\rm S} = 2.8$. Figure from Blum & Kraus (2000).

the photon orbit ($\theta = 0$) one obtains for (ϕ, r)

$$\phi(r) = \phi_0 \pm \int_{r_0}^{r} \frac{b\,dr}{r^2\sqrt{1 - b^2/r^2(1 - R_{\rm S}/r)}}\,, \tag{2.19}$$

where b is the impact parameter of the trajectory. As this integral cannot be solved by analytical means, numerical solutions are usually applied to study light deflection (Kraus, 1998). Fig. 2.22 illustrates the deflection of a photon emitted perpendicular to the neutron star surface.

Many investigations of the effect of light bending on the observational properties of accreting X-ray pulsars have been carried out. Riffert et al. (1993) discussed the effect of gravitational light bending by fitting simplified local emission models to the pulse profiles of Cen X-3, IE 2259+586, and GS 1840+00. Like in non-relativistic approaches (e.g., Leahy, 1991) these authors used non-symmetric magnetic poles to account for the asymmetry in the pulse profiles. However, they found significant differences in the pulse shapes compared to the non-relativistic case. Bulik et al. (1995) applied relativistic model calculations of magnetized neutron star atmospheres to fitting phase resolved spectra of 4U 1538−52 and Vela X-1. Similar to Riffert et al. (1993), they suggested non-antipodally located magnetic poles either due to an off-center or to a bent magnetic axis and alternatively proposed a strong non-dipole component of the magnetic field. Kraus et al. (1996) and Blum & Kraus (2000) have presented a decomposition method which they applied to reconstructing the basic

features of the pulse profiles of Cen X-3 and Her X-1. However, no general model for pulse profiles has so far emerged. From all theoretical models it has become evident that gravitational bending can have a considerable influence on the shape of the pulse profiles and on phase resolved spectra, in particular due to the mixing of contributions to the radiation from both magnetic poles. Due to the enhanced surface visibility of the neutron star, mixing may occur at practically all phases of observations, especially if one assumes a distorted dipole field with asymmetric pole locations.

CHAPTER 3

Cyclotron line formation in strong magnetic fields

"The present situation in physics is as if we know chess, but we don't know one or two rules."

[Richard Feynman]

3.1 Neutron star magnetic fields

Accreting X-ray pulsars can have surface magnetic fields of the order of 10^{12} Gauss. These fields are a million times stronger than the maximum field strength which has been produced in a laboratory on Earth ($85\,\mathrm{Tesla} \lesssim 10^6\,\mathrm{Gauss}$), which is in turn about another million times larger than the magnetic field of Earth ($\sim 0.5\,\mathrm{G}$) itself. See, e.g., Harding & Lai (2006) for a review of the physics of strongly magnetized neutron stars.

Those strong magnetic fields of accreting X-ray pulsars dominate their observational signatures, giving rise to their pulsar characteristics and governing the accretion of matter which produces the energy radiation. Neutron star magnetic fields measured to date span a wide range of at least 10^8 to 10^{15} Gauss (Reisenegger et al., 2005). The strength of the magnetic field can be a distinctive feature of phenomenologically different neutron star categories. Fig. 3.1 illustrates the differences of field strengths for (classical and millisecond) radio pulsars, accreting X-ray pulsars and magnetars. The magnetic field strengths can be derived either from pulsar timing or from the detection of cyclotron resonant scattering features by spectroscopical means. While pulsar timing is restricted to the approximate calculation of a presumed dipolar field component, it will be shown later that the analysis of cyclotron lines provides an elegant tool to probe the magnetic field structure in the X-ray emitting region of a neutron star's magnetosphere.

The origin of the magnetic fields is still a matter of hot debate in the scientific community. Two basic scenarios have been proposed for the formation of neutron

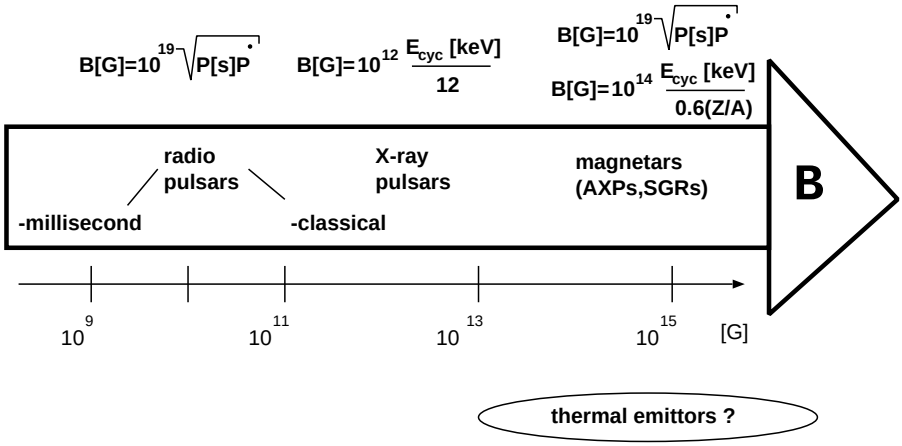

Figure 3.1: Magnetic fields of different classes of pulsars. The dipole and surface magnetic field strengths are estimated from timing (P,$\dot{P}$) or from electron and ion cyclotron lines (see text).

star magnetic fields (Reisenegger, 2003; Reisenegger et al., 2005; Harding & Lai, 2006):

- Fossil field hypothesis. The magnetic field results from an amplification of the progenitor's magnetic field during the collapse. Practically all stars are believed to possess some magnetic field at all evolutionary stages, which persists on very long time scales and with the magnetic field lines frozen into the plasma. The configuration of the magnetic field can thus be changed by changing the macroscopic structure of the plasma. Due to magnetic flux conservation, $\Phi = \pi R^2 B$, the magnetic field of the progenitor star is expected to increase during its collapse into a neutron star as $B \propto R^{-2}$. This theory is supported by the fact that magnetic fluxes of neutron stars have been found to be very similar to the ones of magnetic white dwarfs (Ruderman, 1972), hinting at a common origin of the fields.

- Neutron star dynamos. Thompson & Duncan (1993) presented a scenario in which neutron star magnetic fields are generated by a convective dynamo immediately after the formation of the proto-neutron star. The authors claimed that convection is inevitable due to entropy gradients which form during the phase of rapid neutrino cooling (see section 2.1), holding this statement as an argument against fossil field theories, as the fluid motions would change significantly the lower moments of the field. Their model is based on magnetic dipole

braking (Pacini, 1967; Gunn & Ostriker, 1969; Duncan & Thompson, 1992). Other dynamo theories had been brought forward previously, e.g., by Flowers & Ruderman (1977) and Blandford & Romani (1988).

While simplified models of neutron stars usually assume a dipolar magnetic field structure (Gunn & Ostriker, 1969), pulse profile analysis (Shakura, Postnov & Prokhorov, 1991; Bulik et al., 1995; Blum & Kraus, 2000) and some theories on the field origin (e.g., Urpin, Levshakov & Iakovlev, 1986; Blandford, Applegate & Hernquist, 1983; Arons, 1993; Hankins & Eilek, 2006) hint at possibly more complicated structures like distorted dipoles, the presence of quadrupole moment components, or other non-dipolar magnetic field gradients. As no unique understanding has evolved so far from theory to shed light on the real origin and structure of neutron star magnetic fields, good measurements of the field strength are of fundamental importance.

3.2 Line formation in magnetized accreting neutron stars

The only direct method to determine the magnetic field of neutron stars is the observation of cyclotron resonance scattering features (CRSFs). As opposed to estimates from pulsar timing (compare section 2.4) this technique directly probes the surface magnetic field strength without any a priori assumptions on the field structure. The presence of electron cyclotron lines in X-ray pulsars was first predicted by Gnedin & Sunyaev (1974) – a few years before their actual discovery (Trümper et al., 1978; Wheaton et al., 1979, section 3.3). CRSFs are observed as absorption lines in the spectra of many accreting X-ray binaries. Their line energies are directly related to the magnetic field strength, and may be estimated from a simple expression ('12-B-12 rule'), relating B_{12}, the surface magnetic field strength in units of 10^{12} G, to the energy of the fundamental cyclotron line, E_{cyc}, as:

$$E_{\mathrm{cyc}} = \frac{\hbar e B}{m_{\mathrm{e}} c} = 11.6\,\mathrm{keV}\,B_{12}\,. \tag{3.1}$$

Analysis of their line shapes additionally can probe the local B-field structure and the accretion geometry, rendering cyclotron line analysis an invaluable tool for understanding the physics of magnetized X-ray pulsars.

Cyclotron lines form as a result of scattering processes of high-energy photons during their passage through the relativistic electron plasma in the accretion column. The scattering cross section is resonant at energies corresponding to the separation of the Landau levels, which are the discrete energy levels of the electrons: when the strength of the magnetic field approaches the critical field strength, $B_{\mathrm{crit}} = (m^2c^3)/(e\hbar) = 44.14 \cdot 10^{12}$ G, the de Broglie radius of a plasma electron becomes comparable to its

Larmor radius. Quantum mechanical treatment (see section 3.4) of the electrons' motion perpendicular to the magnetic field lines (Mészáros, 1992; Daugherty & Harding, 1986) reveals a quantization of the electron momenta $p_\perp/(m_\mathrm{e}c) = n(B/B_\mathrm{crit})$. This translates into discrete energy levels, where the fundamental Landau level is given by the 12-B-12 rule (Eq. 3.1) and the higher harmonics have n times this energy. For photon-electron scattering, relativistic effects lead to a slightly anharmonic spacing of the resonant photon energies. Due to the large scattering cross section at the resonances and due to the quasi-harmonic spacing of the thermally broadened Landau levels, photons of energies close to the Landau level energies may not escape the line-forming region unless inelastic scattering has slightly changed their energy. Consequently, absorption features in the photon spectrum are observed at

$$E_n = m_\mathrm{e}c^2 \frac{\sqrt{1 + 2n\frac{B}{B_\mathrm{crit}}\sin^2\theta} - 1}{\sin^2\theta} \frac{1}{1+z}\,, \tag{3.2}$$

where m_e is the electron rest mass, c the speed of light, θ the angle between the incident photon direction and the magnetic field vector, and z is the gravitational redshift at the radius of the line-forming region. Note that the cyclotron lines are enumerated, in the following, starting at $n = 1$, and are referred to as the first or fundamental line at the energy $E_\mathrm{cyc} = E_1$, followed by the second, third, fourth, etc. harmonics ($n = 2, 3, 4, \cdots$). In the literature, they are sometimes also labeled fundamental, first, second, third, etc. harmonic lines. The thermal motion of the electrons parallel to the magnetic field lines broadens the observed line features.

3.3 Observational data

Overview

In 1976, the first cyclotron line was detected in the X-ray spectrum of Her X-1 (Trümper et al., 1977). First interpreted as an emission feature at 53 keV, the line was later proposed to be in absorption with theoretical arguments by Nagel (1981b). Fig. 3.2 shows data from the discovery observation. Since the discovery of the Her X-1 cyclotron line, more sources exhibiting CRSFs have been observed (e.g., Heindl et al., 2004; Staubert, 2003; Coburn et al., 2002; Santangelo et al., 2000). However, cyclotron lines are not seen for all accreting X-ray pulsars, the causes of which are not clear. Different source geometries or magnetic field structure might render at least the fundamental line not observable (O. Nishimura, priv. com.). At the time of writing, at least 15 accreting pulsars with securely detected cyclotron lines with magnetic fields in the range of $1\text{–}5 \cdot 10^{12}$ G are known. Table 3.1 lists accreting X-ray pulsars for which cyclotron line features have been observed to a good level of significance

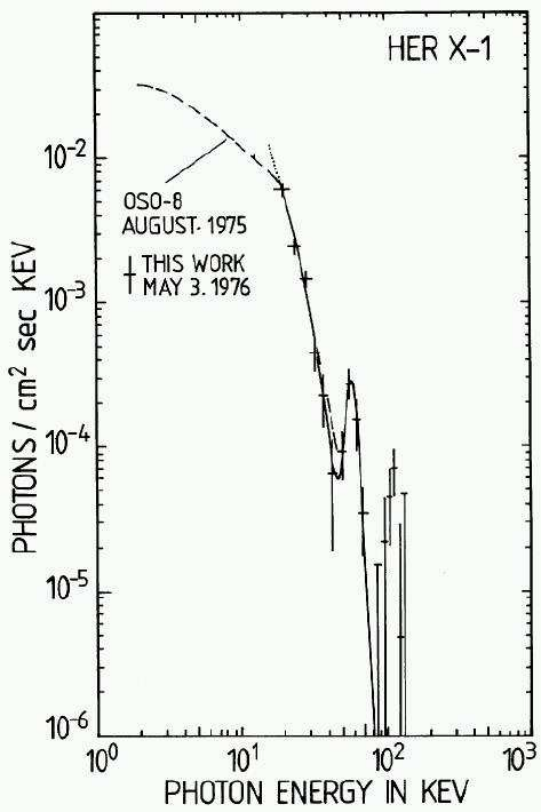

Figure 3.2: First cyclotron line detection in the spectrum of the accreting X-ray pulsar Her X-1 (Trümper et al., 1978). The cyclotron feature was interpreted as an emission feature at 53 keV at that time.

(Heindl et al., 2004; Kreykenbohm, 2004). For other sources, e.g., LMC X-4 or OAO 1657−415, speculations about cyclotron line features were so far not corroborated by recent observations (Tsygankov & Lutovinov, 2005; Barnstedt et al., 2007) by the Rossi X-ray Timing Explorer (*RXTE*) and the International Gamma Ray Astrophysics Laboratory (*INTEGRAL*). For several sources, more than one feature has been detected. The first source where more than two CRSFs were detected was 4U 0115+63 (White, Swank & Holt, 1983), followed by the detection of multiple lines in the spectra of Vela X-1, A0535+26, 4U 1907+09 and V0332+53. The record holder with respect to the number of lines detected is 4U 0115+63 (Heindl et al., 1999;

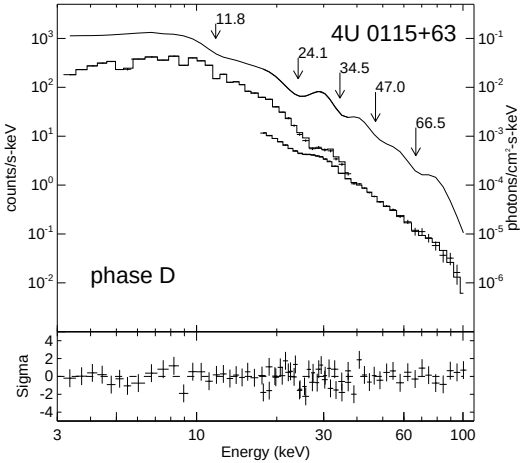

Figure 3.3: Detection of five CRSFs for 4U 0115+63. The data and the unfolded model are shown. Figures from (Heindl et al., 2004)

Santangelo et al., 1999) where five CRSFs were found (Heindl et al., 2000, Fig. 3.3).

CRSF sources are regular targets of observations. The progress over the last decades in energy resolution of instruments on satellites like *BeppoSAX*[1], *RXTE* and, more recently, *INTEGRAL* has led to excellent observational data of many interesting objects with complex cyclotron line features and has made high-quality phase resolved spectroscopy possible. As a result, many interesting characteristics of CRSFs are known today, awaiting a deeper explanation than given by the simple picture of line formation which was outlined in the previous section. More interesting results are expected from the recently launched Japanese *Suzaku*[2] satellite in the future. Some key results from observational studies are:

1. The profile of the fundamental line is resolved, is non-Gaussian, and exhibits a complex shape (e.g., Pottschmidt et al., 2005).

2. The second harmonic appears deeper than the fundamental line (e.g., Nagase et al., 1991; Cusumano et al., 1998; Santangelo et al., 1999).

3. Significant variations of the line parameters of the CRSFs with the pulse phase are observed for some sources (e.g., for Vela X-1, Cen X-3, and GX 301-2

[1] Satellite per Astronomia X, "Beppo" in honor of Giuseppe Occhialini.
[2] Suzaku is a mythical, divine bird symbolizing renewal.

Table 3.1: List of accreting X-ray pulsars with significantly observed cyclotron resonance scattering features extended from Heindl et al. (2004); Kreykenbohm (2004).

Source	E_n [keV]	References
4U 0115+63	14, 24, 36, 48, 62	Wheaton et al. (1979, *HEAO-1*)
		Heindl et al. (1999, *RXTE*)
		Santangelo et al. (1999, *BeppoSAX*)
4U 1907+09	18, 38	Makishima & Mihara (1992)
		Cusumano et al. (1998, *BeppoSAX*)
4U 1538−52	20	Clark et al. (1990, *Ginga*)
GS 1843+00	20	Mihara, Makishima & Nagase (1995, *Ginga*)
Vela X-1	24, 52	Kendziorra et al. (1992, *Mir-HEXE*)
		Kreykenbohm et al. (2002, *RXTE*)
V0332+53	26, 49, 74	Makishima et al. (1990a, *Ginga*)
Cep X-4	30	Mihara et al. (1991, *Ginga*)
Cen X-3	28	Santangelo et al. (1998, *BeppoSAX*)
		Heindl & Chakrabarty (1999, *RXTE*)
X Per	29	Coburn et al. (2001, *RXTE*)
MXB 0656−072	33	Heindl et al. (2003, *RXTE*)
XTE J1946+274	36	Heindl et al. (2001, *RXTE*)
4U 1626−67	37	Orlandini et al. (1998b, *BeppoSAX*)
		Heindl & Chakrabarty (1999, *RXTE*)
GX 301−2	37	Mihara (1995, *Ginga*)
Her X-1	41	Trümper et al. (1978, *Ballon-HEXE*)
A 0535+26	46,102	Kendziorra et al. (1992, 1994, *HEXE*)
		Maisack et al. (1997, *CGRO*)

La Barbera et al., 2003; Suchy et al., 2007, Fig. 3.4) while other sources have relatively stable lines over the phase (e.g., V0332+53).

4. Correlations between observed line and continuum parameters have been proposed, in particular, correlations between the cyclotron line energy and the cut-off energy ($E_{\rm cyc}$ vs. $E_{\rm cut}$) and a correlation of the fundamental line width and depth ($\sigma_{\rm cyc}$ vs. $\tau_{\rm cyc}$) (Coburn et al., 2002; Heindl et al., 2004).

5. The line ratios are not necessarily harmonic. The deviations from the harmonic energies in some spectra are too large to be explained only by the basic relativistic corrections implied by Eq. (3.2) (e.g., 4U 0115+63, Santangelo et al., 1999)

6. The line position of the fundamental CRSF can vary with the source luminosity. Negative (Mihara, 1995; Mowlavi et al., 2006; Nakajima et al., 2006; Tsy-

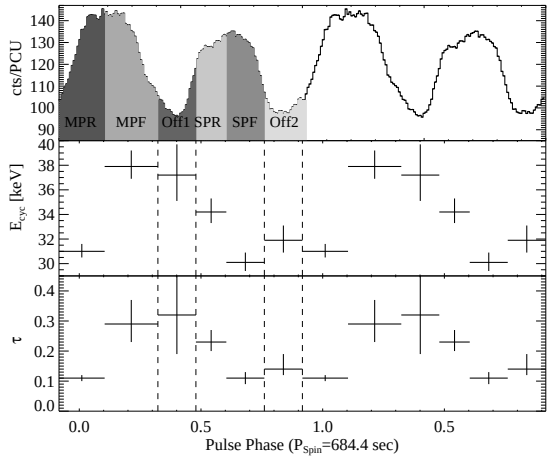

Figure 3.4: Pulse profile and the observed variation of the line position and line depth of the fundamental cyclotron line from phase resolved spectroscopy of GX 301−2 (Heindl et al., 2004).

gankov et al., 2006) and positive (La Barbera et al., 2005; Staubert et al., 2007) linear energy-to-luminosity correlations have been found.

Although cyclotron lines are detected in many sources, a deeper understanding of their shapes is lacking. At present there is no physical model applicable to the analysis of CRSFs in X-ray pulsar spectra. The observations are therefore modeled with phenomenological line shapes, generally by including a multiplicative absorption term

$$F(E) = \mathrm{CONT}(E) \cdot \exp\left(-\tau(E)\right), \tag{3.3}$$

where CONT is the continuum function, and where the most simplest approach to model $\tau(E)$ are Gaussian (`gauabs`, e.g. Soong et al., 1990) or Lorentzian (`cyab`, Tanaka, 1986; Makishima et al., 1990b; Mihara et al., 1990) shapes:

$$\mathrm{GAUABS}(E) = \exp\left(1 - I\exp\left(-\frac{(E-E_0)^2}{2\sigma^2}\right)\right), \tag{3.4}$$

where E_0 is the line energy and σ the line width, or

$$\mathrm{CYAB}(E) = exp\left[-\frac{D(WE/E_{\mathrm{cyc}})^2}{(E-E_0)^2+W^2}\right], \tag{3.5}$$

where D is the Thomson optical depth for $E \gg E_0$ and W gives an artificial line broadening. Sometimes, analysis is also performed overlaying several Gaussians

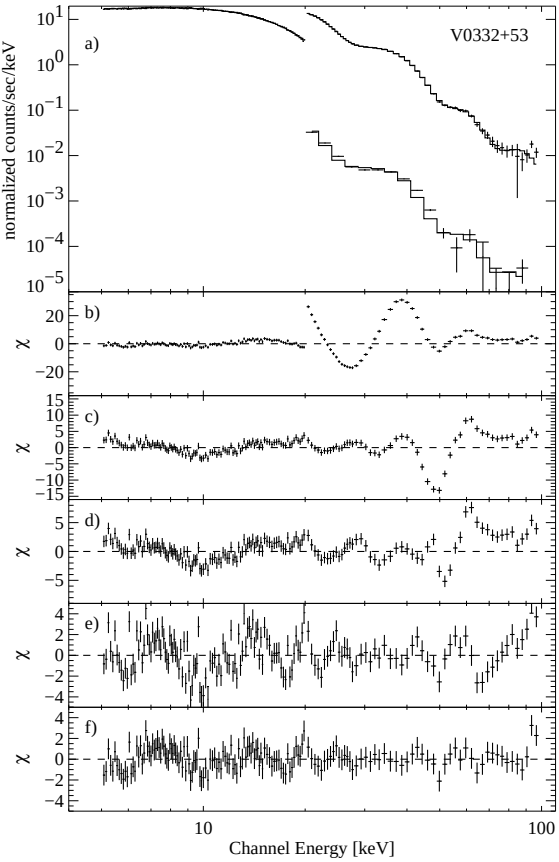

Figure 3.5: (a) Spectrum and best-fit model of V0332+53 from *INTEGRAL* observations (Kreykenbohm et al., 2005). Three lines at ∼26, 47 and 72 keV are detected. The lower panels show the residuals for (b) fitting only the continuum with a powerlaw and high energy rollof, (c) including one Gaussian at 26.6 keV, (d) another one at 47.1 keV, (e) a third one at 30 keV to improve the fundamental shape, and (f) a fourth one at 71 keV.

to reproduce the shape of the fundamental line (e.g., Kreykenbohm et al., 2005; Pottschmidt et al., 2005, Fig. 3.5).

An additional difficulty for the analysis of CRSF is the uncertainty of the underlying continuum shape. The physical processes of the continuum production have been outlined before. Summarizing, the total spectral shape in the X-ray band is described

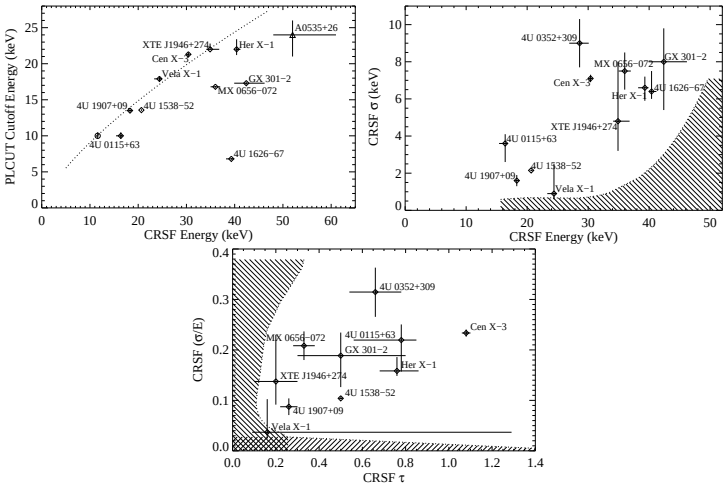

Figure 3.6: Correlations of different line and continuum parameters as proposed e.g. by Coburn et al. (2002) for a sample of accreting X-ray pulsars. Left: Plot of the high-energy cutoff versus the position of the fundamental CRSF; middle: line width versus position; right: ratio of line width to energy versus lide depth. Figures from Coburn et al. (2002).

by the continuum component, roughly a power law with an exponential cutoff, a usually strong Fe Kα line, low energy absorption by high $N_{\rm H}$ and one or more CRSFs. The Fe Kα line generally does not influence the observable properties of the CRSFs because the observed line energies are well above its energy. The choice of continuum can have a certain influence on the line components of the model, in particular if a line is only detected at a low level of significance. Therefore, solid results from observational data are generally tested for different continua to ensure the significance of the CRSF detections as well as the obtained constraints on the line parameters. Some effort has been made to link continuum parameters to line parameters for their physical interpretation (Mihara, 1995; Coburn et al., 2002; Heindl et al., 2004). Fig. 3.6 shows three plots suggesting a correlation of the cyclotron line energy to the high energy cutoff of the continuum, a line-to-width correlation and a width-to-depth correlation of the fundamental line (Coburn et al., 2002).

An intriguing issue which recently has received renewed interest is the question if there is a relation of the resonance energy of CRSFs with respect to the luminosity of a source. First, an anti-correlation of the luminosity to the energy of the fundamental feature, $E_{\rm cyc}$, was observed for some sources (Mihara, Makishima & Nagase, 1998), which was confirmed from monitoring the flux variation during an outburst

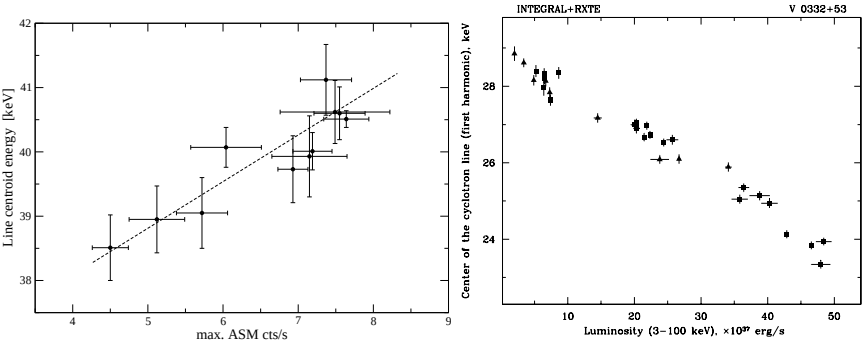

Figure 3.7: Luminosity dependence of the fundamental CRSF. Left: Plot of the centroid cyclotron line energy of Her X-1 versus the maximum flux during the corresponding 35 day Main-On from *RXTE/ASM* observations, fitted by a linear curve of slope 0.66 ± 0.10 keV/(ASM cts/s) (Staubert et al., 2007). Right: Cyclotron line energy versus source luminosity for V0332+53, observed during its 2004/2005 outburst by *RXTE* (squares) and *INTEGRAL* (triangles) (Tsygankov et al., 2006).

of V0332+53 by Mowlavi et al. (2006), Tsygankov et al. (2006, Fig. 3.7, right) and Nakajima et al. (2006). On the other hand, Staubert et al. (2007) recently reported a positive correlation of $E_{\rm cyc}$ with the luminosity from long-term observational data analysis of Her X-1 (Fig. 3.7, left). Some other sources do not show any evidence for any such correlation, an example being the transient source A0535+26 (Caballero et al., 2007). Current explanations suggest a variation of the height of the X-ray emitting region in the accretion column with a changing accretion rate (Mihara, Makishima & Nagase, 1998). Staubert et al. (2007) furthermore proposed that the positive and negative correlations could be explained by distinct accretion regimes, namely sub- and super-Eddington accretion, which imply physically different conditions in the accretion column, in particular determining the presence or absence of a shock (see section 2.3).

A note on cyclotron lines in GRBs and magnetars

At the beginning of cyclotron line studies, there were several claims of detections of cyclotron line features not only in the spectra of accreting X-ray pulsars but also for gamma-ray bursts (GRBs; Mazets et al., 1981). The accumulation of more observational data has, however, cast some doubt onto those detections; for instance the *BATSE* observatory never detected any such feature in GRB spectra (R. Rothschild, priv. com.). However, much of the theoretical work of cyclotron line formation which is applicable to accreting X-ray pulsars was originally motivated by the analysis of

spectral features in GRBs.

For X-ray pulsars, and also – if existent – for GRBs, the observed CRSFs arise from resonant scattering of photons with electrons during the propagation of the radiation through the electron plasma. In the last years, also a different class of CRSFs has been claimed to be observed (Ibrahim et al., 2002): proton cyclotron lines in the spectra of magnetars (e.g., Zane et al., 2001). The high magnetic fields of magnetars prevent the detection of electron cyclotron lines in their spectra. Instead, as the line energy scales also with the mass of the scattering partner as $E_{\rm cyc,ion} = 0.635(Z/A)B_{14}$ keV, where $Z/A \sim 1$ for a proton-electron plasma (Potekhin & Lai, 2007), proton cyclotron lines for magnetars can in principle be observed in the keV range. In the framework of this thesis, exclusively electron cyclotron lines in X-ray binaries are discussed.

3.4 Theory of line formation

3.4.1 Quantization of electrons in a strong magnetic field

The motion of an electron in a constant magnetic field is derived. Early works on this topic can be found, e.g., in publications by Kennard (1927), Fock (1928) and Landau (1930) for the non-relativistic case, and by Rabi (1928), Plesset (1930), and Johnson & Lippmann (1949) for a discussion of relativistic wave functions. The derivations presented here follow Landau (1979), Rabi (1928) and Johnson & Lippmann (1949).

Non-relativistic, QM approach

The non-relativistic Landau states for the motion of a charged particle in an external electromagnetic field may be derived as the stationary states ($\hat{H}\psi = E\psi$) of the Schrödinger equation for the Hamiltonian,

$$\hat{H} = \frac{1}{2m}\left(\hat{p} - \frac{q}{c}A\right)^2 - \hat{\mu}B + q\phi\,, \tag{3.6}$$

where m and q are the rest mass and charge of the particle respectively, A and ϕ are the vector and the scalar potential of the magnetic field of strength B, and the corresponding wave function $\psi = \psi(x, y, z, \sigma, t)$ is a function of the particle's coordinates, spin and time. Equation (3.6) may be understood as the quantum mechanical limit of the analogous classical Hamilton function, where the canonical momentum has been replaced by the momentum operator $\hat{p} = i\hbar\nabla$ and where the extra term $\hat{\mu}B$ arises, accounting for the magnetic moment of particles which possess a spin.

In the following, a constant magnetic field in z direction is assumed ($A_x = -By$ and $A_y = A_z = 0$). The operator for the magnetic moment is given by $\hat{\mu} = \frac{\mu}{s}\hat{s}_z$. The z-component of the spin operator $\hat{s}_z$ commutes with $\hat{H}$ and can be replaced by

its eigenvalue $s_z = \sigma$, denoting the particles spin and $-s \leq \sigma \leq s$. For electrons, $s = 1/2$. The Hamiltonian (3.6) then becomes

$$\hat{H} = \frac{1}{2m}\left[\left(\hat{p}_x - \frac{qB}{c}y\right)^2 + p_y^2 + p_z^2\right] - \frac{\mu}{s}\sigma B\,. \tag{3.7}$$

The x and z components of $\hat{p}$ also commute with the Hamiltonian. The energy states of the particle are calculated as eigenstates of the Hamiltonian with the ansatz:

$$\psi = \exp\left(\frac{i}{\hbar}p_x x + p_z z\right)\chi(y)\,. \tag{3.8}$$

From (3.7) follows

$$\chi'' + \frac{2m}{\hbar^2}\left[\left(E + \frac{\mu\sigma}{s}B - \frac{p_z^2}{2m}\right) - \frac{m}{2}\omega_B^2(y - y_0)^2\right]\chi = 0\,, \tag{3.9}$$

with the abbreviations $y_0 = -cp_z/qB$ and $\omega_B = |q|\,B/mc$. Formally, equation (3.9) has the form of the Schrödinger equation for a harmonic oscillator with frequency ω_B, and with the term in the square brackets taking over the role of the energy of the oscillator with eigenstates $(n + 1/2)\omega_B$ ($n = 0, 1, 2, \cdots$). Therefore, the energy levels of a particle in a homogeneous magnetic field, ('Landau levels'), are given by

$$E_n = \left(n + \frac{1}{2}\right)\hbar\omega_B + \frac{p_z^2}{2m} - \frac{\mu\sigma}{s}B\,. \tag{3.10}$$

For electrons, $q = e$ and $\mu/s = -\,|e|\,\hbar/mc$. The Landau levels,

$$E_n = \left(n + \frac{1}{2} + \sigma\right)\hbar\omega_B + \frac{p_z^2}{2m}\,, \tag{3.11}$$

are degenerate in its quantum states $n, \sigma = 1/2$ and $n + 1, \sigma = -1/2$.

Relativistic approach

The relativistically correct relation for the Landau levels is obtained from the solution of the Dirac equation in the presence of a magnetic field. The eigenfunctions, Φ, are solutions of the Dirac Hamiltonian (Johnson & Lippmann, 1949)

$$H = c\alpha \cdot \pi + \beta mc^2\,, \tag{3.12}$$

where $\pi = p + eA/c$ is the generalized momentum operator, and α and β may be expressed in terms of the 2×2 identity matrix I and the Pauli matrices σ_j ($j = 1, 2, 3$) by substituting

$$\beta = \begin{bmatrix} I & 0 \\ 0 & -I \end{bmatrix}\,, \qquad \alpha_{\mathbf{j}} = \begin{bmatrix} 0 & \sigma_j \\ \sigma_j & 0 \end{bmatrix}\,. \tag{3.13}$$

The corresponding energy eigenvalues ($H\Phi = E\Phi$) are (Johnson & Lippmann, 1949)

$$\begin{aligned} E_n &= \pm \left(c^2p^2 + m^2c^4 + 2ne\hbar cB\right)^{1/2} \\ &= \pm \left(c^2p^2 + m^2c^4 + m^2c^4 2nB/B_{\rm crit}\right)^{1/2} , \end{aligned} \tag{3.14}$$

determined by the principal quantum number $n = l+1/2(s+1) = 0, 1, 2, \cdots$, where $l = 0, 1, 2, \cdots$ is associated with the parallel momentum component to the field, and $s = \pm 1$ denotes the spin (up/down) state of the electron in each Landau state. In the ground state ($n = 0$), only the spin-down state is allowed.

3.4.2 Cross sections for magnetic Compton scattering

In the following, the scattering processes which photons may undergo with the quantized Landau electrons are discussed. The calculation of the strongly frequency and angle dependent cross sections, however, is a formidable task. Explicit derivations of the full QED expressions for the relativistic magnetic Compton cross sections have been performed independently by Daugherty & Harding (1986), Bussard, Alexander & Mészáros (1986) and Mészáros (1992). The cross section matrix elements which are used by the Monte Carlo code and described later in chapter 4, are calculated via a separate code by Sina (1996) which is based on the Sokolov-Ternov formalism (Sokolov & Ternov, 1964, 1968). The total cross sections are calculated from their integration over a one-dimensional thermal electron distribution (Alexander & Mészáros, 1989; Harding & Daugherty, 1991; Araya & Harding, 1996, 1999; Araya-Góchez & Harding, 2000). The resulting cross section profiles will be further discussed in chapter 4 when introducing the model setup. This section reviews some general relevant properties of the magnetic cross sections, starting with a few words about early and recent approximative work.

Early results on the cross-sections have been presented, e.g., by Canuto, Lodenquai & Ruderman (1971) and Ventura (1979). Fig. 3.8 shows the strong frequency dependence of the magnetic cross sections as obtained from a cold-plasma approximation (Ventura, 1979). No higher harmonics occur due to the cold plasma limit, which Ventura (1979) proposed to extend for an application to accreting X-ray pulsars. Fig. 3.8, however, illustrates the dependence on the photon polarization: while the extraordinary photons are highly resonant, the ordinary mode photons are unaffected[3]. The ordinary-mode photons and electrons undergo continuum scattering, approximated by (Arons, Klein & Lea, 1987; Becker, 1998)

$$\sigma_{\rm ord}(E, \theta) = \sigma_{\rm T} \left[\sin^2\theta + k(E)\cos^2\theta\right] , \tag{3.15}$$

[3]The ordinary and extraordinary modes are distinguished from the electric field vector: while for ordinary photons, the electric field vector lies in the plane formed by the magnetic field vector and the photon propagation direction, for extraordinary photons, it is orientated perpendicular to this plane (Becker & Wolff, 2007).

while both continuum and resonant interaction in the case of the extraordinary photons gives (Arons, Klein & Lea, 1987; Becker, 1998)

$$\sigma_{\rm ext}(E,\theta) = \sigma_{\rm T} k(E) + \sigma_l \phi_l(E, E_{\rm cyc}, \theta)\,, \tag{3.16}$$

where $\sigma_{\rm T}$ is the Thomson cross section, and

$$k(E) = \begin{cases} 1 & E \geq E_{\rm cyc} \\ (E/E_{\rm cyc})^2 & E \leq E_{\rm cyc} \end{cases}\,, \tag{3.17}$$

ϕ_l is the line profile function, normalized to unity, and

$$\sigma_l = 1.9 \cdot 10^4 \sigma_T \, B_{12}\,. \tag{3.18}$$

The directional dependence of photon scattering with respect to the magnetic field can be approximated for energy and mode-averaged cross sections if the mean energy of the photons, $\langle E \rangle$, is sufficiently small compared to the cyclotron energy (Wang & Frank, 1981; Becker, 1998; Becker & Wolff, 2007) for photons moving in parallel or perpendicular to the magnetic field vector as

$$\sigma_{||} \sim \sigma_{\rm T} \left(\frac{\langle E \rangle}{E_{\rm cyc}} \right)^2\,, \tag{3.19}$$

and

$$\sigma_{\perp} \sim \sigma_{\rm T}\,. \tag{3.20}$$

A good approximation of the relativistic QED cross sections for scattering processes to the ground Landau state ($l = 0$) was given by Gonthier et al. (2000). Using the Johnson & Lippmann (1949) wave functions they presented spin-averaged analytical results for sub- and supercritical magnetic fields and compared them to exact solutions and to other approximations (see Fig. 3.9).

Electron transition rates

The following derivation closely follows Harding & Preece (1987). As it was shown in section 3.4.1, the state of an electron in a strong magnetic field is completely described by the three quantities (n, s, p), where n is the principal quantum number denoting its Landau state ($n = 0, 1, 2, \cdots$), $s = \pm 1$ give the spin state of the electron, and p is its parallel momentum component to the field. A photon is described by its energy ω and by its angle of propagation θ with respect to the magnetic field vector.

An electron in an initially excited Landau level ($n > 0$, s, p) can undergo a transition to a lower Landau state ($n' < n$, s, p) by emission of a photon. The photon's

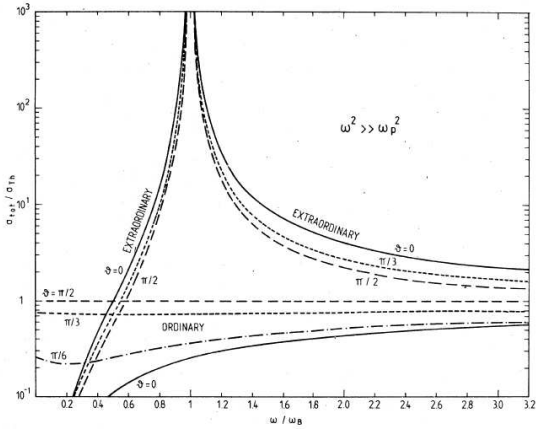

Figure 3.8: Fig. 2 from Ventura (1979). Frequency dependence of magnetic scattering cross sections. The ordinary-mode photons are unaffected. No peaks at higher harmonics (cold plasma limit), nor the temperature broadening is included.

energy and its angle of propagation with respect to the magnetic fields are given from the kinematics by

$$\omega = \frac{(E - p\cos\theta) - \sqrt{(p\cos\theta - E)^2 - 2m^2 B/B_{\rm crit}(n-n')\sin^2\theta}}{\sin^2\theta}\,. \qquad (3.21)$$

Emitting a photon under an angle θ with respect to the magnetic field, the electron itself will change its parallel momentum suffering a recoil along the field direction:

$$p' = p - \omega\cos\theta\,. \qquad (3.22)$$

The probability for an electron transition from a state (n, s, p) to another state (n', s', p') is calculated from the integration of its differential transition rate, i.e. the probability to emit a photon of energy ω and at angle θ (Harding & Preece, 1987),

$$R^{s,s'}_{n,n'}(\theta) = \frac{e^2}{2\pi}\int(\Phi_\parallel + \Phi_\perp)\delta(E - E' - \omega)\omega d\omega\,, \qquad (3.23)$$

over energy and angle. The integration over energies yields

$$R^{s,s'}_{n,n'}(\theta) = \frac{\alpha}{2\pi}\frac{\omega(E-\omega)(\Phi_\parallel + \Phi_\perp)}{(E - p\cos\theta - \omega\sin^2\theta)}\,, \qquad (3.24)$$

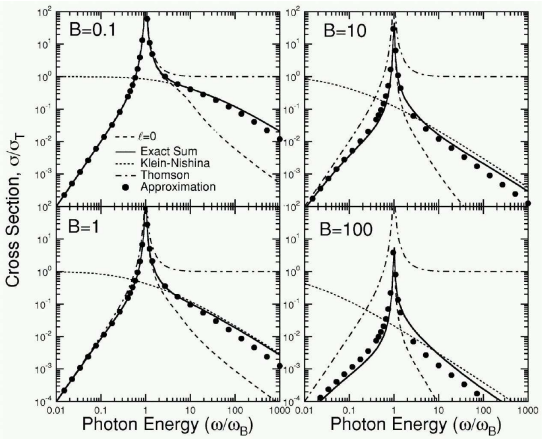

Figure 3.9: Analytic approximation of QED cross sections. The total cross section in Thomson units as a function of the incident photon energy in units of the cyclotron energy is shown for $B/B_{\rm crit} = 1 \cdot 10^{-1\cdots 2}$. Fig. 2 from Gonthier et al. (2000).

while the integration procedure over angles must be done numerically. Harding & Preece (1987) have done extensive calculations of transition rates up to Landau states $n = 500$. The Φ denote the first-order matrix elements for photons which are polarized parallel and perpendicular to the plane of B and the wave vector k. Expressions for these matrix elements have been derived by different authors. Sokolov & Ternov (1968) found that they are of the form (see appendix of Harding & Preece, 1987)

$$\Phi_{\parallel} = \alpha_1^* \alpha_1 \tag{3.25}$$

$$\Phi_{\perp} = |\alpha_2 \cos\theta - \alpha_3 \sin\theta|^2 \ , \tag{3.26}$$

with the star denoting the complex conjugate. The explicit expressions for transverse polarization are the following:

$$\alpha_1 = \frac{i}{4}(A_3' A_4 + A_4' A_3)[B_3' B_4 I_{n,n'-1}(x) - B_3 B_4' I_{n-1,n'}(x)] \,,$$

$$\alpha_2 = \frac{1}{4}(A_3' A_4 + A_4' A_3)[B_3' B_4 I_{n,n'-1}(x) - B_3 B_4' I_{n-1,n'}(x)] \,,$$

$$\alpha_3 = \frac{1}{4}(A_3' A_3 + A_4 A_4')[B_3' B_3 I_{n-1,n'-1}(x) + B_4 B_4' I_{n,n'}(x)] \,,$$

where

$$A_3 = \left(1 + \frac{p}{E}\right)^{1/2}, \qquad A_4 = s\left(1 - \frac{p}{E}\right)^{1/2},$$
$$B_3 = \left(1 + s\frac{m}{p_0}\right)^{1/2}, \qquad B_4 = s\left(1 - s\frac{m}{p_0}\right)^{1/2},$$
$$p_0 = (E^2 - p^2)^{1/2}, \qquad x = \frac{\omega^2 \sin^2\theta}{2m^2 B/B_{crit}},$$
$$\text{and} \quad I_{m,l}(x) = \frac{\sqrt{l!}}{\sqrt{m!}} e^{-x/2} x^{(m-l)/2} L_l^{m-l}(x).$$

Absorption versus scattering

Harding & Daugherty (1991) compared the cross sections for resonant scattering and for absorption in order to find the conditions under which the full complex scattering cross section can be approximated well by the much more simple absorption cross sections. Considering relativistic decay rates and near-critical magnetic fields, they found the shape of the scattering cross sections to agree relatively well with their first order absorption approximation at the resonance energies. However, the non-resonant scattering terms were found to differ significantly, especially near higher harmonics (compare Fig. 3.10). For the analysis of cyclotron line shapes, it is important to understand how these scattering profiles give rise to the final line shapes, observed "in absorption". While the complex line shape of the fundamental line results from complicated scattering between different Landau level states, the higher harmonics are 'almost' absorption features as the electron transition rates at low fields are biased preferring the decay in single perpendicular momentum quanta (Araya & Harding, 1999).

3.5 Numerical models

There are two very different approaches to modeling the radiative transfer in the accretion column: solving finite difference equations and Monte Carlo simulations. Both model types have to make assumptions on the basic geometry of the line-forming region (compare section 2.3) and on (radiation processes yielding) the seed photon spectrum (compare section 2.5). The emergent spectra after the propagation of the seed photons through the line-forming region are then calculated for different viewing angles.

In section 2.3, different model approaches for the physics in the accretion column were discussed. Although many attempts have been made to assess the structure of

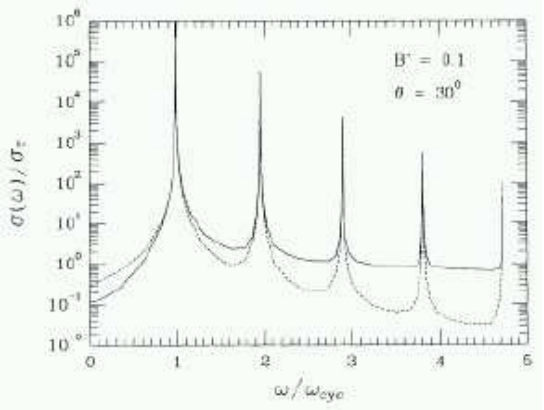

Figure 3.10: Scattering (solid line) and absorption (dashed line) cross sections. Fig. 1 from Harding & Daugherty (1991)

the accretion column and the region of X-ray emission and line formation, most of its properties remain rather enigmatic up to date. As a general scenario, the picture of an accretion column or funnel is widely accepted, in which the matter from the accretion flow is confined frozen to the magnetic field lines, while the radiation can escape. The incident radiation or seed continuum (compare section 2.5) is believed to result from up-scattered blackbody, synchrotron and predominantly bremsstrahlung photons within the accretion mound and column (Becker & Wolff, 2005). For numerical modeling, cylindrical and plane-parallel slab geometries are usually assumed to model a line-forming region above or at the neutron star surface (compare Fig. 3.11). The source of seed photons is generally placed either at the mid-axis of the cylinder and at the mid-plane of the slab for internal illumination ('1-1 geometry'), or at the bottom of the slab for external illumination ('slab 1-0 geometry', Freeman et al., 1999; Isenberg, Lamb & Wang, 1998b). While in the 1-0 geometry photons which return to the source plane after scattering are absorbed ('reflected photon flux'), in the 1-1 geometry photons may cross the source plane and the reflected and the transmitted flux are symmetric. Those geometrical constraints will be further discussed in chapter 4 when introducing the model approach taken in this work.

Solving difference equations

Motivated by the Her X-1 line detection, Nagel (1980, 1981b) presented a solution of the radiation transfer equation for static neutron star atmospheres, using a two-stream approximation for just one angle of emergent radiation. Having first suggested a line-

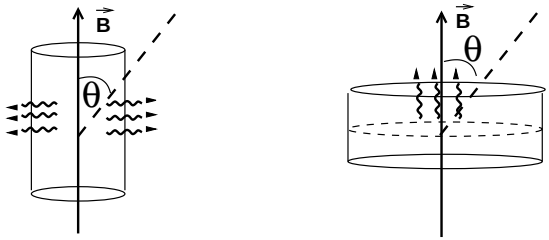

Figure 3.11: Two simplified orthogonal cases to modeling the line-forming region in the accretion column are shown. Left: cylindrical geometry. Right: slab geometry. Photons escape with an angle θ with respect to the magnetic field vector.

formation mechanism for a cyclotron emission feature (Nagel, 1980), in their later paper considering Comptonization effects, Nagel (1981b) then favored the Her X-1 line to appear in absorption. Some years later, Mészáros & Nagel (1985a,b) employed refined Feautrier methods to solve the radiative transfer for four and eight angles. They performed two sets of calculations, treating effects of anisotropy and Comptonization separately. For the combined effects of anisotropy and Comptonization, Mészáros & Nagel (1985a) compared model predictions for different geometries (slab and cylinder geometry with internal or external illumination) and discussed variations with the angle of the emergent spectra. Mészáros & Nagel (1985b) also modeled pulse shapes. From both studies, they favored the slab geometry as an emission scenario. Their approach was later refined by the inclusion of higher harmonics (Alexander & Mészáros, 1991) and by including radiation pressure and temperature corrections in the atmosphere (Bulik et al., 1992, 1995). Recently, the influence of a non-uniform magnetic field in the line-forming region on the formation of CRSFs has been investigated with similar techniques by Nishimura, who predicted the variations of the line ratios of the CRSFs for the case of a dipolar (Nishimura, 2003) and for a linearly varying (Nishimura, 2005) magnetic field.

Monte Carlo simulations

Yahel (1979) was the first to use Monte Carlo simulations for simulating the CRSF formation in the atmosphere of a magnetized neutron star. He considered the formation of pulse profiles and X-ray spectra and found that the Her X-1 feature could indeed be produced as a consequence of resonant scatterings of extraordinary polarized photons. Two years later, Pravdo & Bussard (1981) calculated angle-dependent pulsar spectra, including relativistic corrections to the Compton cross section and considering polarization dependence. Focusing on the continuum spectral shape they found a

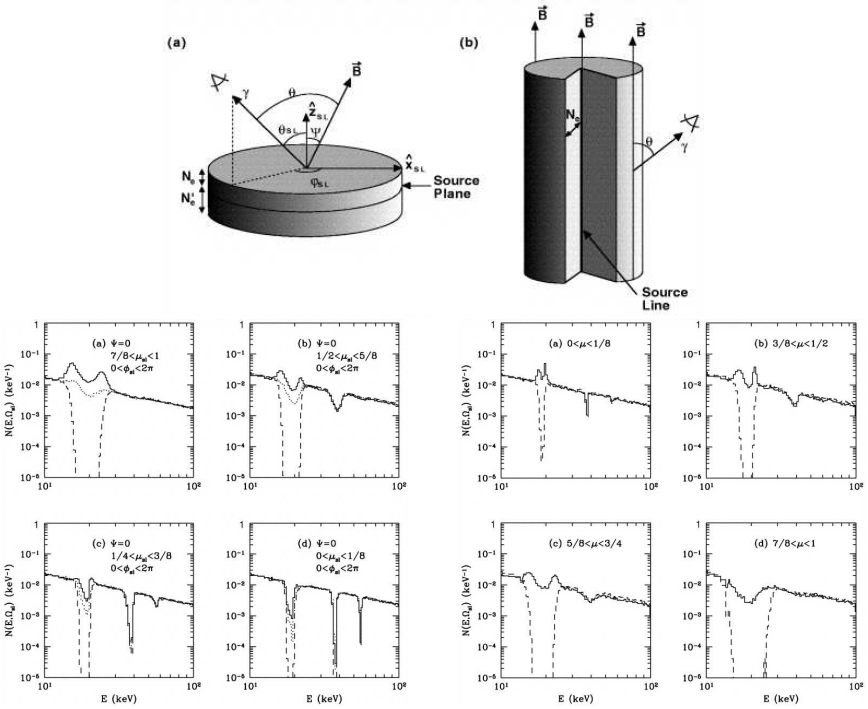

Figure 3.12: Figs. 1, 7 and 19 from Isenberg, Lamb & Wang (1998b). Top: (a) Slab geometry with magnetic field direction at an angle to the slab normal. The slab is infinite in extent. $N_{\rm e}$ is the column depth between the source plane and the top surface; $N'_{\rm e}$ is the column depth between the bottom surface and the source plane. (b) Cylindrical geometry with magnetic field parallel to cylinder axis. The cylinder is infinite in length. $N_{\rm e}$ is the column depth between the photon source, located along the cylinder axis, and the surface. Bottom left: Spectra for $\Phi = 0$ and several viewing angles. $B_{12} = 1.7$ and $N_{\rm e,21} = N_{\rm e}/10^{21} = 1.2$. Monte Carlo spectra for the 1-1 (solid lines) and 1-0 (dotted lines) geometries are shown, as well as relativistic absorption spectra with finite natural line width (dashed lines). Bottom right: cylindrical line-forming region with magnetic field $B_{12} = 1.7$ oriented along the cylinder axis. The column density from the cylinder axis to the surface is $N_{\rm e,21} = 1.2$. Monte Carlo spectra for scattering (solid lines) and absorption (dashed lines) are shown.

hardening of the spectra towards the magnetic equator. Wang et al. (1989) performed Monte Carlo simulations for the geometry of a plane-parallel slab with the slab normal parallel to the B-field vector, and the plasma being illuminated from below. Results from a generalized model, where the slab normal may have any direction with respect

to the B-field were discussed by Isenberg, Lamb & Wang (1998a,b, Fig. 3.12). For the case where the slab normal is perpendicular to the magnetic field vector, their results are comparable to assuming a cylinder geometry for the line-forming region. Isenberg, Lamb & Wang (1998b) distinguished between line shapes of optically thin and optically thick matter. As one key result these authors found that the line wings disappear either for the 1-1 geometry and optically thick media or for the 1-0 geometry and optically thin media. However, none of these scenarios could explain the observed fundamental shallow and broad features due to the high equivalent width of the fundamental in both cases.

Inspired by the detection of up to two cyclotron lines[4] at 45 and 100 keV (Kendziorra et al., 1994) and at 100 keV (Grove et al., 1995) during subsequent outbursts of the transient source A0535+26 in 1989 and 1994, Araya and Harding presented a new set of Monte Carlo simulations for very hard spectra of X-ray pulsars with near-critical fields (Araya & Harding, 1996, 1999; Araya-Góchez & Harding, 2000) to model the 100 keV line (assumed to be the fundamental line). For a low-density plasma and hence low continuum optical depths, they produced spectra for slab 1-1 and cylinder geometry of a plasma threaded by near-critical magnetic fields and discussed the influence of parameters as geometry, optical depth and anisotropy of the photon source on the line shapes. The results presented in this work are based on their approach. The development and improvements of the new model approach taken here are discussed in the next chapter.

[4] Recently it was shown that both lines claimed by Kendziorra et al. (1994) are present in the source data (Kretschmar et al., 2005; Wilson & Finger, 2005; Inoue et al., 2005; Caballero et al., 2007).

CHAPTER 4

Model design

4.1 Aims

The key objective of this work is to obtain a physically motivated model for CRSF formation which is directly comparable to observational data. Firstly, such a comparison is fundamental when testing and reconsidering the validity of the model. Secondly, only an easy applicability of the final-stage model to real observational data provides the means for a systematic investigation of the manifold properties of CRSF sources.

4.2 Methods

In order to achieve the desired flexibility, the CRSF model, presented in the following, is based on Monte Carlo simulations. The Monte Carlo simulations are realized using a revised, generalized version of a code which was originally developed by Araya & Harding (1996, 1999) and Araya-Góchez & Harding (2000). A new key feature of the current modeling is a Green's functions approach to obtain independence from any continuum model assumed. The original implementation of an internally irradiated slab geometry is generalized to include also the case of illumination from the bottom. More information on the Monte Carlo implementation and details of the Green's function approach are given in Sect. 4.4 and in the appendix. Due to the variety of sources to be modeled and the uncertainty of the general physical picture, calculations are performed on a large multidimensional parameter grid. All simulation results are merged into archives in the form of FITS tables[1] which are available to the scientific community. Line features for X-ray pulsar spectra for different physical settings (as outlined in the next section) within a preset parameter scope may be produced from these tables with a special convolution and interpolation model, also implemented as

[1] Flexible Image Transport System: standard astronomical data format (see, e.g., `http://fits.gsfc.nasa.gov`).

a local model for the spectral analysis software package *XSPEC* (Arnaud, 1996) and other analysis packages such as ISIS (Houck & Denicola, 2000).

4.3 Physical setting

The formation of cyclotron line features in a static neutron star atmosphere is simulated. Magnetospheric accretion is assumed to yield a line-forming region which is spatially confined to a region at or above the neutron star surface. The seed photons are propagated through this medium, where they interact with the quantized plasma electrons via resonant scattering processes. The physical conditions in the line-forming region and its geometrical structure are prescribed by a set of parameters (Araya & Harding, 1999), which are discussed in the next paragraphs.

4.3.1 Magnetic field [B]

As a first approximation, the magnetic field is assumed to be uniform on the scale of the line-forming region. The field strengths simulated are between $1 \cdot 10^{12}$ and $7 \cdot 10^{12}$ Gauss, chosen to encompass the whole range of B-fields found in accreting X-ray pulsar spectra up to date. Sect. 5.3 describes a possible generalization to non-uniform magnetic fields.

4.3.2 Plasma electrons [T_e, $f(p_\mathrm{e})$, n]

A low-density thermal plasma is considered. While relatively low densities justify the approach to neglect collisional interactions ($n_\mathrm{e} \ll 8 \cdot 10^{27} B_{12}^{7/2}\,\mathrm{cm}^{-3}$; Lamb, Wang & Wasserman, 1990) and photon polarization ($n_\mathrm{e} \ll 10^{22} B_{12}^{4}\,\mathrm{cm}^{-3}$; Lamb, Wang & Wasserman, 1990; Gnedin, Pavlov & Shibanov, 1978), the thermal plasma approximation is motivated by the strong photon-electron coupling at the resonances (Araya & Harding, 1999). All electrons are assumed to be initially in their fundamental Landau state $n = 0$. This assumption is justified by the very high cyclotron radiative decay rate (per electron) for sub-critical fields

$$r_\mathrm{rad} = 3 \cdot 10^{15}\, B_{12}^{2}\,\mathrm{s}^{-1} \tag{4.1}$$

compared to the collisional excitation rate

$$r_\mathrm{col} = 5 \cdot 10^{8} (n_\mathrm{e}/10^{21}\mathrm{cm}^{-3})\, B_{12}^{-3/2}\,\mathrm{s}^{-1} \tag{4.2}$$

(Latal, 1986; Bonazzola, Heyvaerts & Puget, 1979). For their motion parallel to the B-field vector, a thermal distribution of the electrons is assumed. Their parallel momenta

p_e are given by a relativistic Maxwellian distribution

$$f(p_\mathrm{e})dp_\mathrm{e} \propto \exp\left(-\frac{m_\mathrm{e}c^2(\sqrt{1+\left(\frac{p_\mathrm{e}}{m_\mathrm{e}c}\right)^2}-1)}{kT_\mathrm{e}}\right)dp_\mathrm{e}\,, \tag{4.3}$$

where T_e is the parallel electron temperature and k is the Boltzmann constant. In the literature, T_e is often linked to the strength of the magnetic field (e.g. Lamb, Wang & Wasserman, 1990; Isenberg, Lamb & Wang, 1998b; Araya & Harding, 1996, 1999; Araya-Góchez & Harding, 2000). Lamb, Wang & Wasserman (1990) inferred a value of the equilibrium Compton temperature due to resonant scattering of $kT_\mathrm{e} \sim 0.27 \cdot E_\mathrm{cyc}$ from the numerical analysis of detailed thermal balance in a strongly magnetized atmosphere ($\tau_T \ll 1 \ll \tau_\mathrm{cyc}$, $N_{\mathrm{e},21} < 6$). This proposed relation is taken into account in order to determine the order of magnitude of the parallel plasma temperature, but T_e is left as a free parameter in the simulations to keep the new model's flexibility (see also Sect. 5.4). A slowly sinking plasma where bulk plasma motion may be neglected is assumed. If bulk motion contributes, a Doppler-shift of the resonance energies is expected. The effects of bulk motion are discussed in detail, e.g., by Weth (2001).

4.3.3 Optical depth [τ_T]

The Thomson optical depth τ_T of the plasma is prescribed. The optical depth for cyclotron scattering τ_cyc relates to the Thomson optical depth as

$$\tau_\mathrm{cyc} = \frac{\sigma_\mathrm{cyc}}{\sigma_\mathrm{T}}\tau_\mathrm{T}\,, \tag{4.4}$$

implying a scattering optical depth τ_cyc which is up to a factor of 10^5 larger than τ_T at the resonances of σ_cyc. Fig. 4.1 shows the thermally averaged cross section $\langle\sigma_\mathrm{cyc}\rangle/\sigma_\mathrm{T}$ as a function of energy and angle, calculated as a second order QED process (Sina, 1996). Besides a highly resonant behavior of the cross section at the Landau energies, Fig. 4.1 also illustrates the angle-dependent relativistic shift in the resonances as well as the thermal broadening of the profiles. Line features are calculated for Thomson optical depths between $\tau_\mathrm{T} = 1 \cdot 10^{-4}$ and $\tau_\mathrm{T} = 3 \cdot 10^{-3}$ (Araya & Harding, 1999). Depending on the plasma geometry, the resulting mean free path of a photon in the line-forming region is different for the same trajectory. The simulated Thomson optical depths correspond to electron column densities $N_\mathrm{e} = \tau_\mathrm{T}/\sigma_\mathrm{T}$ between $1.5 \cdot 10^{20}\,\mathrm{cm}^{-2}$ and $4.5 \cdot 10^{21}\,\mathrm{cm}^{-2}$. Unfortunately, the densities which describe the accreted plasma are very poorly restricted (Isenberg, Lamb & Wang, 1998b). The values assumed here are comparable to values suggested in other recent numerical or analytical studies. For instance, column densities of $N_\mathrm{e} \sim 10^{21}$–$10^{22}\,\mathrm{cm}^{-2}$ are

assumed by Nishimura (2003, 2005), and values of $N_{\rm e} \sim 10^{22}\,{\rm cm}^{-2}$ are inferred by Becker & Wolff (2007) for the sources Her X-1, LMC X-4, and Cen X-3.

4.3.4 Geometry [cy, sl11, sl10]

Two basic geometries of the line-forming region are distinguished, motivated by the complementary 'standard' pictures of accretion depicted in Fig. 2.14 (see also section 2.3 and Basko & Sunyaev, 1976): for the case of flow stopping through nuclear collisions at the surface, the geometry of a thin, plane-parallel slab is adopted (Mészáros et al., 1983; Harding et al., 1984). Radiative shocks or shocks from collisionless instabilities, on the other hand require a cylindrical shape of the X-ray emitting region (e.g., Becker & Wolff, 2007, and references therein). The heights of slab atmospheres are expected to be significantly smaller (Lamb, Pethick & Pines, 1973; Wang, Wasserman & Salpeter, 1988) than typical radii, $h \ll r_0$, of the accretion mound (Ostriker & Davidson, 1973; Becker & Wolff, 2007). For cylindrical geometries, Becker & Wolff (2007), who investigated a more complicated shock structure with a velocity flow gradient, found height to width ratios, h/r_0, of the emitting region for several X-ray pulsars of the order 10^2. The simulations also suggest that practically all photons escape before reaching such boundaries, justifying the assumption of infinite extended plane-parallel line-forming regions. For the cylinder, in agreement with previous studies, an internally irradiated plasma with the photon source located at the cylinder axis (Araya & Harding, 1999; Araya-Góchez & Harding, 2000) is assumed, being the most simple approach to the matter. Two locations of the source plane, are considered for the slab. The scenario of a line formation region above an isotropically emitting source is realized by a bottom-illuminated slab (Freeman et al., 1999; Isenberg, Lamb & Wang, 1998b; Wang, Wasserman & Salpeter, 1989). Slater, Salpeter & Wasserman (1982) argued from Monte Carlo simulations that placing the photon source at the midplane of a plane-parallel slab is representative of the scenario of line formation in an isothermal, semi-infinite atmosphere. The two slab geometries will be referred to as slab 1-1 and slab 1-0 geometry from now on, where the numbers $1 : x$ represent the ratios of the column densities, $N_{\rm e}$, the photons see in the opposite escape directions. The emergent radiation components are referred to as the 'transmitted flux' and 'reflected flux' (Freeman et al., 1999). For 1-0 geometry, the reflected flux is absorbed at the neutron star surface. For the case of the photon source located at a the slab midplane, the column densities are equal ($x = 1$) and transmitted and reflected flux are symmetric (compare figure 3.12).

The optical depth which the photons see in direction θ when covering an optical depth $\Delta\tau_{\rm T}$ along the slab normal or perpendicular to the cylinder depends on the

geometry as:

$$\Delta\tau_{\rm T}(\theta) = \frac{\Delta\tau_{\rm T}}{\sin\theta} \quad \text{(cylinder geometry)} \tag{4.5}$$

$$\Delta\tau_{\rm T}(\theta) = \frac{\Delta\tau_{\rm T}}{\cos\theta} \quad \text{(slab geometry)} \ . \tag{4.6}$$

4.4 Technical realization

The resonant scattering processes between incident photons and plasma electrons are simulated using Monte Carlo simulations. The scattering processes lead to the formation of cyclotron line features. The current code like the original code by Araya & Harding uses a separate code by Sina (1996) for the calculation of the relativistic cross sections. Resonant scattering with electrons up to the fourth harmonic is included.

The current code comprises technical modifications such as an improved angular and energy resolution and increased statistics. More important, the geometrical constraints are also relaxed to include the scenario of a bottom illuminated slab (1-0 geometry) which was not investigated by Araya & Harding (1996, 1999) and Araya-Góchez & Harding (2000).

The key difference of the new code for the actual modeling of cyclotron lines in X-ray pulsar spectra is a Green's functions approach, i.e., the calculation of the probabilities for photon energy redistribution instead of the calculation of a total spectrum of all photons for an initial seed photon spectrum. In each Monte Carlo run 10000 photons of the same incident energy, $E_{\rm in}$ are inserted. For each photon a random angle $\theta_{\rm in}$ ($\cos(\theta_{\rm in}) \in (-1, 1)$) with respect to the magnetic field direction is picked repeatedly, at which it is propagated through the plasma (see below). The probabilities for the photon redistribution into different energy and angular bins after the passage of the plasma are calculated from all final states of escaped photons. The initial angular distribution of the photons is assumed to be isotropic. The relevant energy range $\{E_{\rm in}\}$ for cyclotron line formation is assessed as follows: using the 12-B-12 rule and assuming quasi-harmonic spacing of the cyclotron lines (see eqs. 3.1 and 3.2), the energy range containing the first four Landau levels can be fixed by applying a normalization to the magnetic field, E/B_{12}. Due to the link of resonant energy and magnetic field, the choice of this scale is important. First of all, it gives an optimized resolution of the CRSF features in the same way for different magnetic fields. Even more important, the choice of this scale is fundamental for later interpolation of the Green's functions: as the resonant energies are directly linked to the magnetic field, an interpolation of the line shapes in E/B_{12}-space ensures consistent results. For $E_{\rm in}[\text{keV}]/B_{12} \in [6, 48]$, a grid of Green's functions $G(E_{\rm in} \rightarrow E_{\rm out}, \theta_{\rm out})$ was obtained. $E_{\rm in}$ is sampled by 161 Monte Carlo runs, the resolution of the redistributed

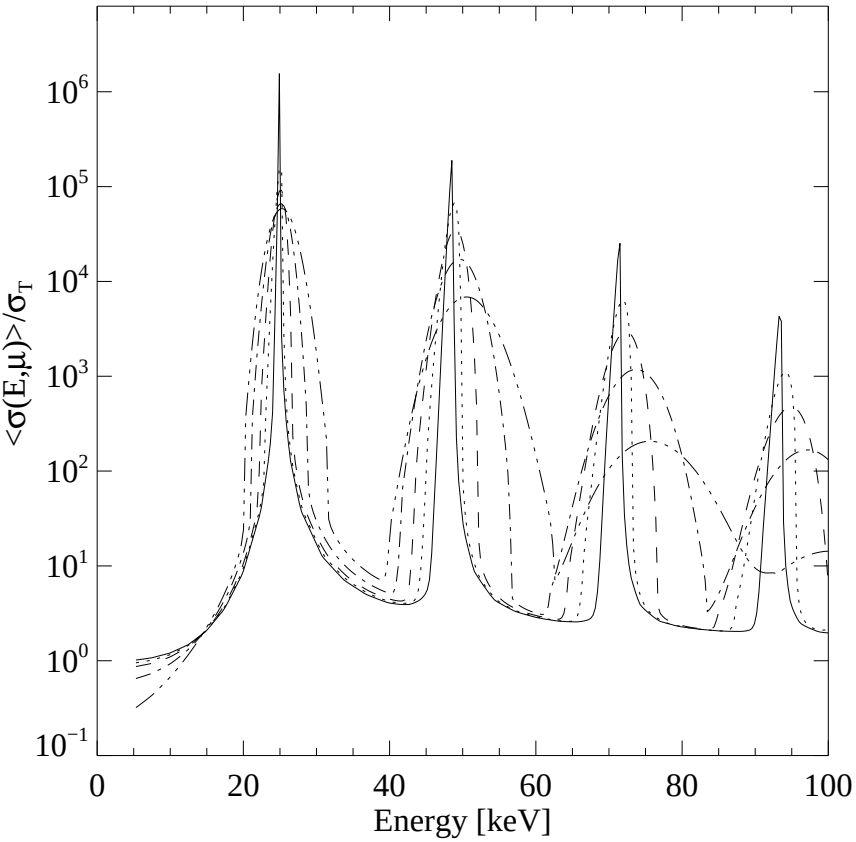

Figure 4.1: Cross sections for $B/B_{\rm crit} = 0.05$ and $kT_{\rm e} = 3\,{\rm keV}$, thermally averaged over the sampled electron momenta, and in units of the Thompson cross section $\sigma_{\rm T}$. The resulting profiles are shown for different angles θ of the photon's direction with respect to the magnetic field vector. Solid, dotted, dashed, dash-dotted and dash-and-triple-dotted lines: $\cos\theta = 0.005$, 0.200, 0.375, 0.625 and 0.875. Figure based on Araya & Harding (1999).

energies $E_{\rm out}$ is given by an internal energy binning of 640 bins.

Each Monte Carlo photon is injected into the plasma with an initial energy $E_{\rm in}$ and at an initial direction $\theta_{\rm in}$. The photon is then propagated according to its mean free path, $1/(n_{\rm e}\,\langle\sigma(E_{\rm in},\cos\theta_{\rm in})\rangle\,)$, and an electron is picked as a scattering partner. The

Table 4.1: Parameter grid.

parameter	$B/B_{\rm crit}$	$kT_{\rm e}$ [keV]	μ	$\tau_{\rm T}$	$E_{\rm in}/B_{12}$	geo
lower bound	0.03	2.5	0	$1 \cdot 10^{-4}$	6	-/-
upper bound	0.15	20	1	$3 \cdot 10^{-3}$	48	-/-
N(points)	10	5	8	4	161	3 (cy, sl11, sl10)

electron is characterized by its parallel momentum, $p_{\rm e}$ (Eq. 4.3), and its Landau state n. According to the scattering cross section (obtained from interpolation of previously calculated and tabulated values as a function of B), the state of the electron-photon pair changes from its incident configuration $(E^{(0)}, \theta^{(0)}) + (p_{\rm e}^{(0)}, n^{(0)})$ to a different state $(E^{(1)}, \theta^{(1)}) + (p_{\rm e}^{(1)}, n^{(1)})$. The new mean free path of the photon is calculated and the photon is propagated further. If the electron remains in an excited Landau state $n' > 0$ after scattering (absorption and instantaneous radiative decay), another photon is emitted with $(E^{(2)}, \theta^{(2)}) + (p_{\rm e}^{(2)}, n^{(2)})$ and processed further. This photon spawning can produce up to three secondary photons. Once a photon has escaped from the plasma, its contribution to the output spectrum is stored. Fixing the input angular distribution of the incident photons to be isotropic for a large part of the present work is done for reasons of simplicity, and in order to keep the computational expenses reasonable. However, a smaller grid in B and $T_{\rm e}$ of angle dependent Green's functions $G(E_i, \theta_m \rightarrow E_j, \theta_k)$ has also been calculated for selected geometries, to discuss the generalization to arbitrary angular photon distributions (see section 5.2.2). Polarization of the photons is not included, however, polarized photons should yield a comparable picture (Wang, Wasserman & Salpeter, 1988) for the low-density regime chosen.

Calculations were performed in six-dimensional parameter space for a non-regular grid of points $[B/B_{\rm crit}, T_{\rm e}, \mu, \tau_{\rm T}, E_{\rm in}, \text{geo}]$ within the ranges listed in table 4.1. The current parameter grid is resolved into $\sim 6{\cdot}10^6$ grid points requiring a simulation time of the order of 10^5 CPU hours on 2 GHz workstations. The resolution was chosen such that the variation of the Green's functions between two points is sufficiently small to allow for interpolation. Hence, CRSFs can be predicted by the convolution of a continuum spectrum for any parameter combination on this grid as follows: First, the corresponding Green's functions G* are obtained by linear interpolation in all parameters except the geometry on E/B_{12}. Sets of Green's functions $\{G^*(E_i \rightarrow E_j, \theta_k)\}_j$ for several different example input energies E_i and a fixed physical setting are shown in Figs. 4.2 and 4.3. Second, the emergent photon flux $F^{\rm em}(E_j, \theta_k)$, i.e., the number of photons per keV in the $j^{\rm th}$ energy bin and $k^{\rm th}$ angular bin (binned

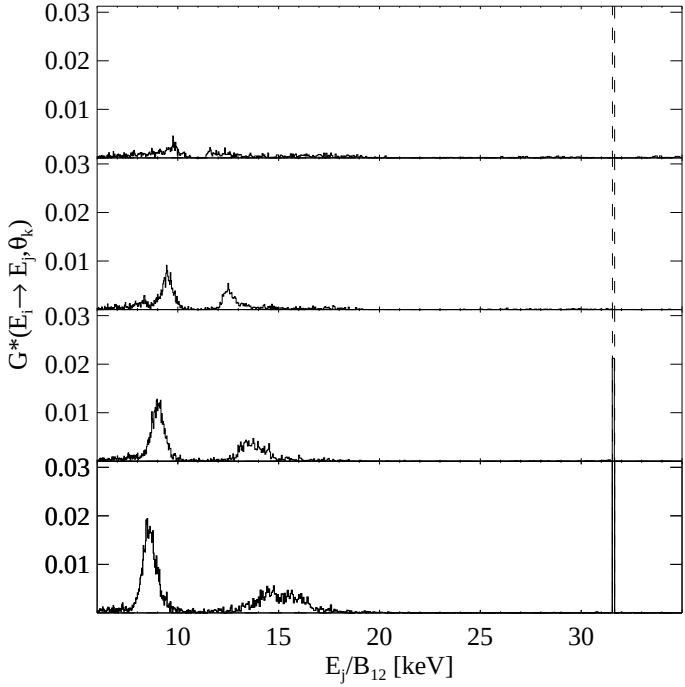

Figure 4.2: Green's functions plotted for one input energy $E_i/B_{12} = 31.6\,\mathrm{keV}$ (dashed lines) against all output energies $\{E_j\}_j$, and into four (of eight) $\cos\theta$ bins ($\cos\theta \in [0.125, 0.250)$, $[0.375, 0.500)$, $[0.625, 0.750)$, $[0.875, 1.0)$ from top to bottom). The physical setting is as follows: slab geometry, $B/B_{\mathrm{crit}} = 0.06$, $kT_{\mathrm{e}} = 5\,\mathrm{keV}$, $\tau_{\mathrm{T}} = 3 \cdot 10^{-3}$. E_i is chosen to simulate photon input at the third harmonic line. Most photons are redistributed by photon spawning to the wings of the fundamental line.

in $\cos\theta$) can be calculated, as a function of the (isotropic) incident continuum flux F^{cont} by convolving F_{cont} with this interpolated set of Green's functions (compare appendix)

$$F^{\mathrm{em}}(E_j, \theta_k) = \frac{\sum_i G^*(E_i \to E_j, \theta_k)\, F^{\mathrm{cont}}(E_i) \Delta E_i}{\Delta E_j}\,. \tag{4.7}$$

Note that because of this approach CRSFs for arbitrary continuum shapes can be calculated without rerunning the simulations. For illustrative purposes, in the following the most simple phenomenological continuum model, a power law with a high-energy rolloff (Eq. 2.14), is used for folding spectra with the CRSF Green's functions.

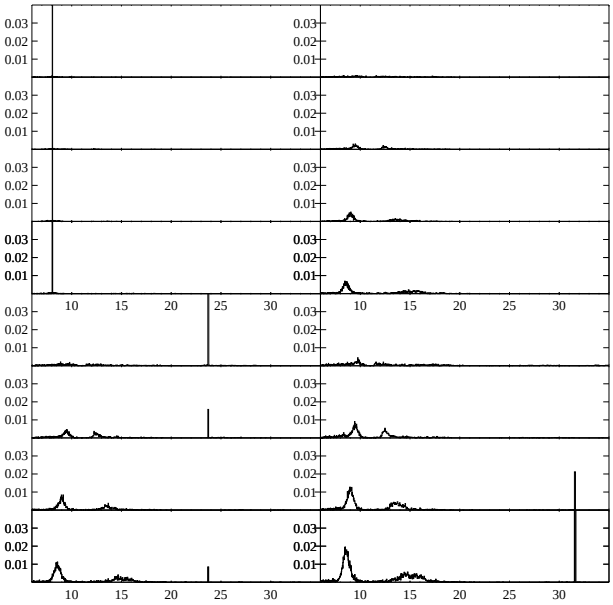

Figure 4.3: Same as figure 4.2 but for different input energies $E_{\rm in}/B_{12}/{\rm keV} = 8.1$ (top left), 11.5 (top right), 23.8 (bottom left), and 31.6 keV (bottom right). The values of $E_{\rm in}$ correspond to photon input below the first harmonic, and in the first, second and third CRSF features.

4.5 Consistency check and modeling progress

After the code revision and the development of the Green's function convolution model, the current predictions were compared to the results from the original code. Fig. 4.4 shows a direct comparison of the line shapes obtained from the current model version to the spectra obtained by Araya & Harding (1999); Araya-Góchez & Harding (2000). While the panels of reduced resolution confirm the internal consistency, the high-resolution results clearly demonstrate the progress of modeling line shapes. Technical improvements in this analysis with respect to the earlier results are the following: the line shapes were calculated with higher statistics of effectively $1.6 \cdot 10^6$ Monte Carlo photons per folded spectrum (increased from $5 \cdot 10^4$). They are better resolved in energy, being calculated on a grid of 640 energy bins instead of 80 for the relevant energy range. The angular resolution was increased from four to eight

angular bins of μ. The chosen statistics give a well resolved picture of the line shapes, however, the centroid of the second harmonic would require even better statistics for continuum optical depths of $\tau_{\mathrm{T}} \sim 3 \cdot 10^{-3}$. Theoretical predictions from the current model status are discussed in the next chapter.

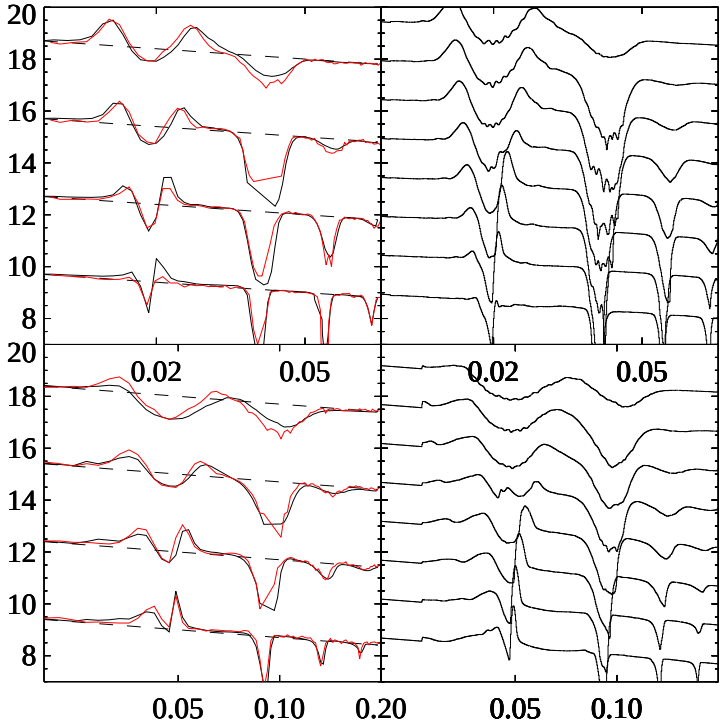

Figure 4.4: Modeling progress. Line shapes obtained from the revised Green's function model and spectra produced by the original MC code (Araya & Harding, 1996, 1999; Araya-Góchez & Harding, 2000) are plotted on the same scale. Left: The new data (black lines) is rebinned to the angular and energy resolution of the original data (red lines). Regions of photon depletion (Araya-Góchez & Harding, 2000) were connected by lines, accounting for the apparent discrepancies, e.g., in the top left panel, second plot from the top, second harmonic. Top left: slab geometry, $B/B_{\rm crit} = 0.04$, $kT_{\rm e} = E_{\rm cyc}/4$, 80 energy, 4 angular bins. Setting corresponds to Fig. 1, top left, in Araya-Góchez & Harding (2000). Top right: same setting with higher resolution of new data. Bottom left: $B/B_{\rm crit} = 0.1$, $kT_{\rm e} = E_{\rm cyc}/4$, 80 energy, 4 angular bins. Setting corresponds to Fig. 5, top right, in Araya-Góchez & Harding (2000). Bottom right: same setting with a higher angular and energy resolution (current model data).

CHAPTER 5

Theoretical predictions

In this section theoretical predictions from the Monte Carlo simulations are made (Schönherr et al., 2007b). Their implications on observed properties of cyclotron lines are discussed. Special emphasis is placed on the study of the line parameters, i.e. line position, line width and line depth, of the fundamental CRSF. The line shapes are shown for full spectra, which were chosen to be of a simplified power law shape with a high-energy rolloff (Eq. 2.14) with a power law index of $\alpha = 1$–2 and a folding energy $E_{\rm fold} = 40$ keV for illustrative purposes. The choice of this rather high folding energy compared to observational results facilitates the investigation of emission wing features (see later), as it leads to a pronounced contribution from high-energy photon spawning to the CRSFs (see section 5.5). More realistic spectra for X-ray pulsars are shown in chapter 6.

5.1 Geometry and optical depth

Figs. 5.1, 5.2 and 5.3 show full spectra folded with the convolution model for a fixed magnetic field, $B/B_{\rm crit} = 0.05$, and parallel temperature, $kT_{\rm e} = 3$ keV, for slab and cylinder geometries, for two different values of $\tau_{\rm T}$ and for different angular bins of the emergent angle θ of the photons (see chapter 3, Fig. 3.11). Although the second harmonic is not fully described in its core, the calculations clearly show that the second harmonic is more pronounced than the fundamental one, in agreement with observational findings (Cusumano et al., 1998). The fundamental CRSF has a more complex, broad and shallow shape, often with emission wings. The line profiles have distinct shapes for different geometries, especially concerning the line wings of the fundamental feature which are strongest for the internally illuminated plasmas (see later). Such strong wings are expected as a consequence of the injection of the source photons at the mid-plane of a slab (1-1 geometry) and at the mid-axis of a cylinder. For slab geometry, e.g., Isenberg, Lamb & Wang (1998b) and Nishimura (2005) showed comparisons of the slab 1-1 and the slab 1-0 geometry, and pointed out that these wings can be understood as the leftovers of one strong emission feature forming from

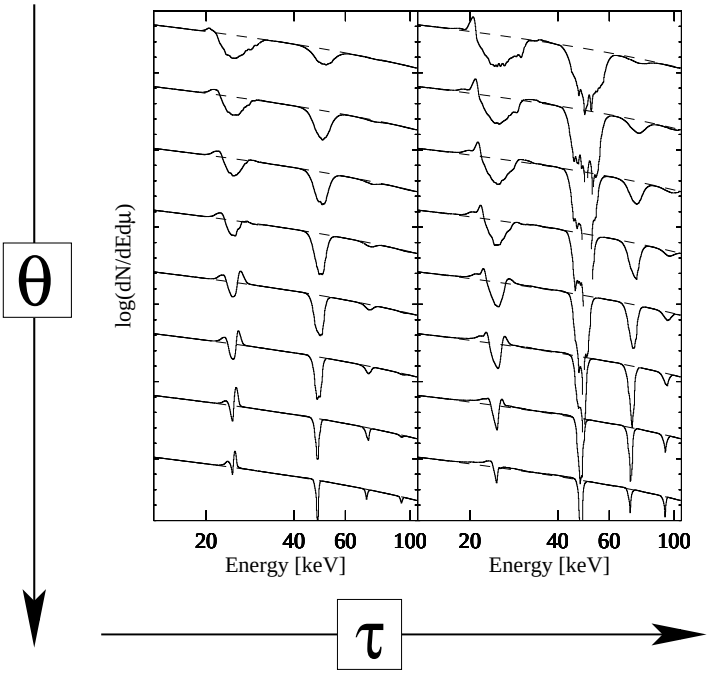

Figure 5.1: Line profiles for cylinder geometry as a function of angle and optical depth. Left: continuum optical depth $\tau_{\rm T} = 3 \cdot 10^{-4}$; right: $\tau_{\rm T} = 3 \cdot 10^{-3}$. The emergent spectra from all eight angular bins are shown (bottom to top: $\mu = \cos\theta \in (0.000, 0.125)$, $[0.125, 0.250)$, $[0.250, 0.375)$, $[0.375, 0.500)$, $[0.500, 0.625)$, $[0.625, 0.750)$, $[0.750, 0.875)$, $[0.875, 0.1000)$). In both panels, $B/B_{\rm crit} = 0.05$ and $kT_{\rm e} = 3.0$ keV. The continuum photon flux is assumed to have a power law distribution with photon index $\alpha = 2.0$ and an exponential high energy cutoff at the folding energy $E_{\rm fold} = 40$ keV.

photons crossing the source plane, which then becomes an absorption feature from scattering processes in the outer layers of the line-forming region. For very small optical depths, $\tau_{\rm T} = 10^{-4}$, this initial emission feature can be confirmed by the Monte Carlo simulations presented here. Observations of sources with CRSFs have not been seen to exhibit such strong emission wings. Fig. 5.4 illustrates the difference of the line shapes when considering a slab illuminated at the midplane or at the bottom. In Sect. 6.4, the observability of those features with modern instrumentation will be further commented on.

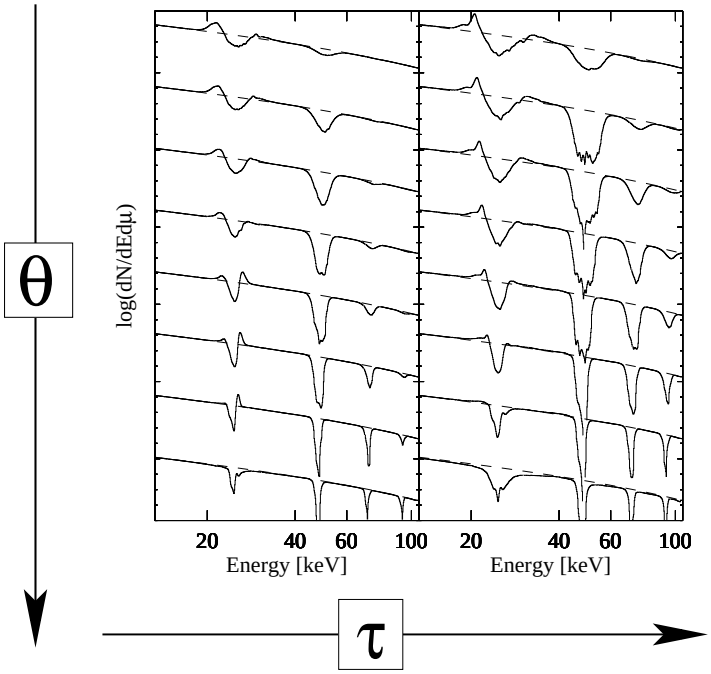

Figure 5.2: Same as Fig. 5.1 for slab 1-1 geometry.

5.2 Angular redistribution

5.2.1 Isotropic photon injection

Photons are injected isotropically into 20 angular bins[1] in $\cos\theta$. Although the distribution of the initial photon directions is isotropic, a high degree of anisotropy arises after the photons have been propagated through the plasma due to a highly anisotropic scattering cross section (compare Fig. 4.1). Fig. 5.5 shows the angular redistribution of the photons for both geometries and for different values of the optical depth. Internally the code keeps track of twenty $\cos\theta$ bins. For illustration, the angular redistribution resolved into eight final bins is shown. For $\tau_{\rm T} = 3 \cdot 10^{-4}$ there is a trend of an overall redistribution towards smaller θ for slab geometry and a reverse trend for cylinder geometry. For a larger optical depth, $\tau_{\rm T} = 3 \cdot 10^{-3}$, these trends increase for

[1]The binning is chosen such that it resolves the angular redistribution fine enough while being computationally reasonable.

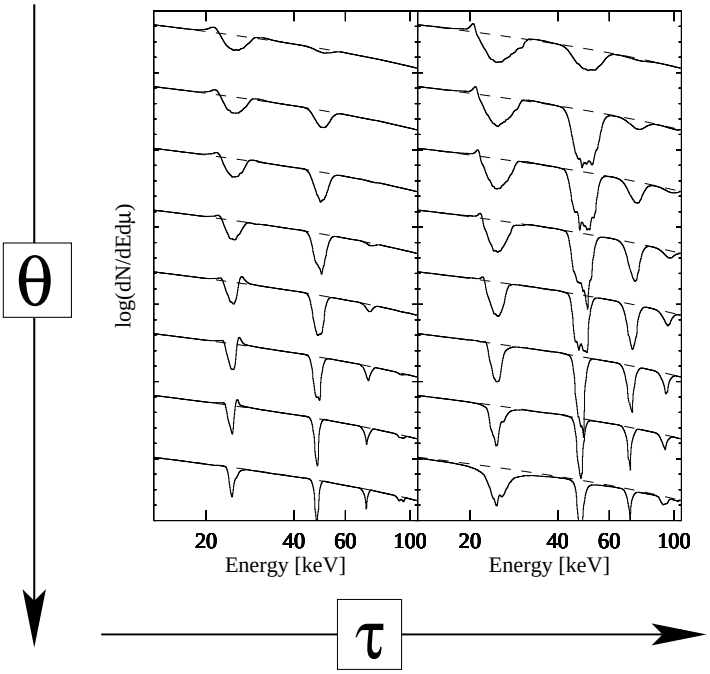

Figure 5.3: Same as Fig. 5.1 for slab 1-0 geometry.

slab and decrease for cylinder geometry, where the curve in Fig. 5.5 flattens. Those results are conform with the picture of the formation of a broader 'fan' and more sharply beamed 'pencil' beam emergent radiation for cylinder and slab geometries. This can be understood from the dependence of the scattering cross sections on the angle (see Fig. 4.1) which implies that there is a general trend of a photon redistribution by scattering towards smaller angles, i.e. larger $\cos\theta$, regardless of geometry. The larger the optical depth a photon must pass, the more scatterings take place and the more dominant this effect becomes. This fact can also account for a less prominent trend in the slab 1-0 geometry compared to the 1-1 geometry, as photons which experience many scatters by various crossings of the source plane are thermalized, biasing the emerging radiation. For a fixed optical depth $\tau_{\rm T} = 1 \cdot 10^{-3}$ similar plots were shown resolved into all twenty bins by Araya-Góchez & Harding (2000). For $\tau_{\rm T} \sim 8 \cdot 10^{-4}$, the angular photon redistribution of the line photons was discussed by Isenberg, Lamb & Wang (1998b). Due to the redistribution of the photons with

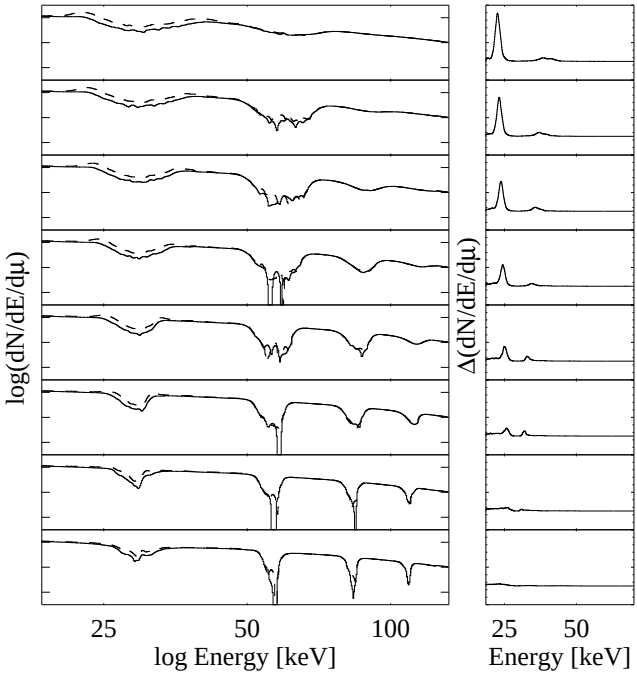

Figure 5.4: Comparison of slab 1-1 and 1-0 geometry. Left panel: folded spectra for 1-1 (dashed line) and 1-0 (solid line) geometry and for eight angular bins in double logarithmic representation. Right panel: Difference of spectra (1-1)-(1-0) at energies around the fundamental line in linear representation. Note the strong emission wings for the 1-1 geometry. In all plots, $B/B_{\rm crit} = 0.06$, $kT_{\rm e} = 5\,{\rm keV}$, $\tau_{\rm T} = 3 \cdot 10^{-3}$, and μ increasing from bottom to top (see Fig. 5.1).

respect to their angle, also the cyclotron line shapes vary significantly. Fitting the fundamental feature with the continuum spectral function multiplied with a Lorentzian in absorption for the absorption feature and two Lorentzians in emission for the emission wings gives the line parameters. Fig. 5.6 shows the position, the line width and the line depth of the fundamental CRSF versus the emergent angle of the photons, as obtained from these phenomenological fits.

The line position of the fundamental CRSF varies little with the viewing angle and thus cannot account for the amount of change in line positions observed for some

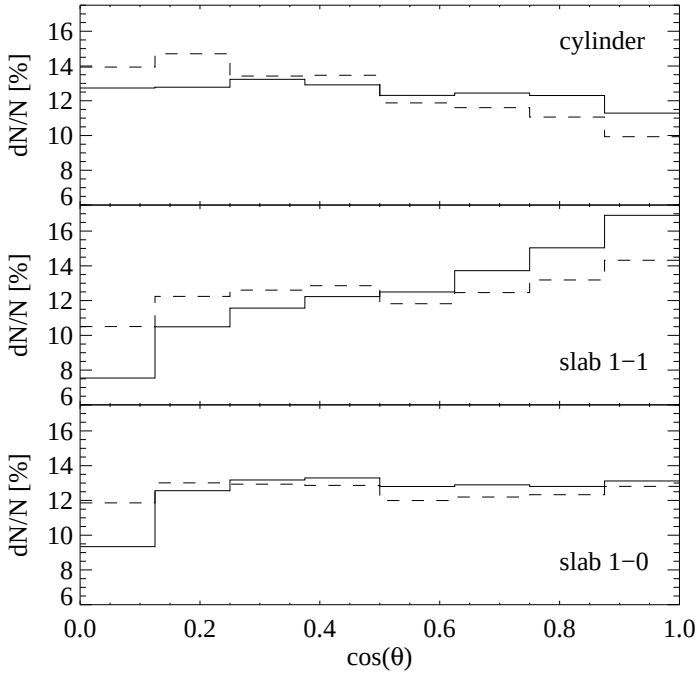

Figure 5.5: Angular redistribution of the photons. For isotropic photon injection, the percentage of the emitted photon flux into eight angular bins for the spectra in Figs. 5.1, 5.2 and 5.3 is shown. Top: cylinder geometry, middle: slab 1-1 geometry, bottom: slab 1-0 geometry. Solid lines: $\tau_{\rm T} = 3 \cdot 10^{-3}$, dashed lines: $\tau_{\rm T} = 3 \cdot 10^{-4}$.

sources with the phase. Therefore, different explanations have to be sought. A possible explanation could be that the photons which escape the line-forming region into the direction of the observer during different rotational phases of the system, have passed through regions of different magnetic field strengths. These differences again could be either due to small-scale B-field gradients of a locally non-dipolar field (see later), or possibly due to a change of the geometry of the system. The choice of a static line-forming region, however, might also be a too simplified assumption. Weth (2001) has proposed that the bulk motion of the plasma can Doppler-shift the fundamental line considerably, yielding differences of up to 30% in minimum and maximum line energies. However, from Becker & Wolff (2007), a slowly moving plasma beyond

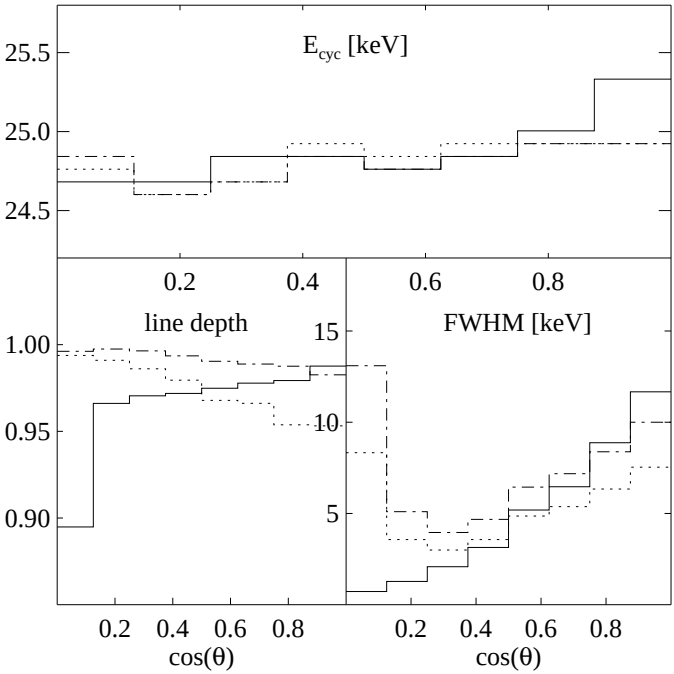

Figure 5.6: Variation of the line parameters of the fundamental CRSF with the angle of emission. Solid lines: cylinder geometry, dashed lines: slab 1-1 geometry, dash-dotted lines: slab 1-0 geometry. All values are obtained from fits of the line shapes depicted in Figs. 5.1, 5.2, and 5.3, and for a Thompson optical depth of $\tau_{\rm T} = 3 \cdot 10^{-3}$.

the shock is expected.

The line depth increases with $\mu = \cos\theta$ in the case of cylinder geometry, and decreases for slab geometry. This is understood from Eqs. (4.5) and (4.6), as they predict the largest optical depth for small θ for cylinder, and for large θ for slab geometry. For cylinder geometry, the line width increases clearly with μ as expected from the angle-dependence of relativistic Doppler broadening (see Eq. 5.2 below), which is reinforced by the increasing optical depth with μ. The decreasing optical depth with angle for slab geometry instead suppresses the trend of the line broadening with μ. From observational studies (compare Fig. 3.6 in section 3.3), different intercorrelations of the line parameters have been proposed. Among others, a positive correlation

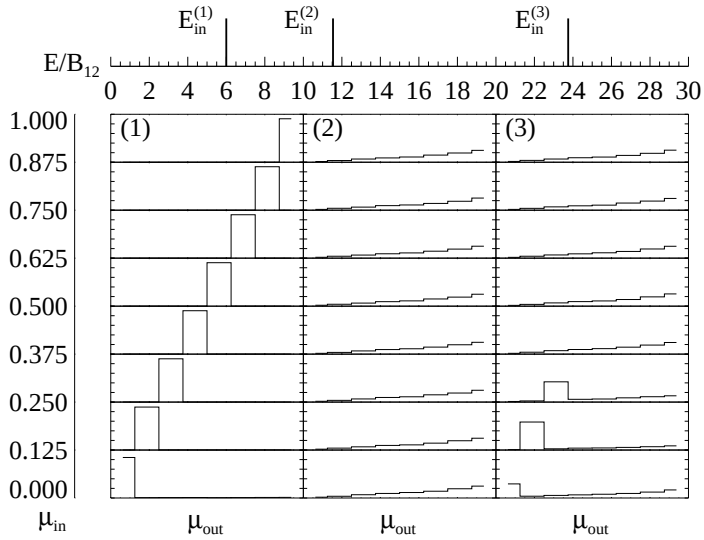

Figure 5.7: Angular redistribution of photons from monoenergetic and unidirectional injection. (1) injection at energies outside the resonance, (2) injection at energies in the line core of the fundamental, (3) injection in the second harmonic, near the wing. The matrix of input and output angle is shown, where the height of the function indicates the percentage of photons emerging from a certain $\cos\theta$ bin.

of the line depth with the line width, scaled by the cyclotron energy was proposed by Heindl et al. (2004). If this suggestion holds true, the results from Fig. 5.6 support the scenario of a cylindrical geometry of the line-forming region.

5.2.2 Non-isotropic photon injection

In the scope of this work, isotropic photon injection is assumed for the analysis of the line shapes. The changes of the line-shapes for anisotropic photon injection have been studied by Araya-Góchez & Harding (2000) assuming simplified initial photon distributions, e.g. an emission cone or fan beam, parallel or perpendicular to the magnetic field vector. However, no unique understanding of the angular distribution of the seed photons has been agreed on so far for the beam patterns (compare sections 2.4, 2.5 and 2.6) from theoretical modeling. Studies of the continuum processes like the one of Becker & Wolff (2007) hopefully will help to shed more light on this matter. Consider-

ing radiation processes in general (see section 2.5), however, anisotropy of the initial photon distribution is expected to be a rather realistic assumption. To qualitatively test the effects of beamed photon injection, therefore, the Green's functions, generalized to arbitrary angular photon distributions, $G^*(E_{\rm in}, \mu_{\rm in} \rightarrow E_{\rm out}, \mu_{\rm out})$, have been calculated for a small parameter sample (fixed $B/B_{\rm crit} = 0.03$ and $kT_{\rm e} = 2.5\,$keV, slab 1-1 geometry).

Figure 5.7 shows angular redistribution functions for monoenergetic and unidirectional photon injection. The percentage of emergent radiation into different angular bins is shown for photons which have been injected at different angular bins and at different input energies in or near the lines. Photons which are injected far outside the resonance ($E_{\rm in}^{(1)}$) do not undergo any scattering processes and, as expected, are not redistributed into different angles. Photons which are injected at energies in the core of the fundamental resonance ($E_{\rm in}^{(2)}$) suffer so many scatterings that their strong final angular redistribution is independent from their initial angle of injection. The redistribution of those resonance photons resembles the total photon redistribution shown in Fig. 5.5 for isotropic photon injection and slab 1-1 geometry. Photons which are injected at energies corresponding to the wing of the second harmonic ($E_{\rm in}^{(3)}$) are completely redistributed for large μ but partly remain in their initial angular bin for small μ. These results indicate that the change of the line features for anisotropy should be mainly seen due to contributions from the line wings which is in agreement with spectral features shown by Araya-Góchez & Harding (2000).

5.2.3 Mixing different angular contributions

For a distant observer at a viewing angle $\tilde{\theta}$, gravitational light deflection may change considerably the photons' directions (compare section 2.6). The enhanced surface visibility and possibly asymmetric magnetic pole geometries also render an observation of radiative contributions from both magnetic poles probable. The variation of the viewing angle $\tilde{\theta}$ with respect to one magnetic pole (i=1,2) with the rotation of the neutron star (rotation angle Φ) is (Kraus et al., 2003, see Fig. 5.8):

$$\cos\tilde{\theta} = \cos\theta_0 \cos\theta_i + \sin\theta_0 \sin\theta_i \cos(\Phi - \Phi_i) \tag{5.1}$$

where θ_0 is the angle between the rotational axis and the line of sight, $\theta_{1,2}$ indicate the polar angle locations of the two magnetic poles with respect to the rotational axis, and Φ_i defines the rotational phase where the axis through pole i passes closest to the line of sight (Kraus et al., 2003). The corresponding change in flux generates the observed pulse profile. When neglecting the effect of gravitational bending, this angle $\tilde{\theta}$ is identical to the intrinsic angle θ of the escaping photons with respect to the magnetic field. Otherwise, photons which are observed under this angle have intrinsically emerged the line-forming region at a different angle which has to be calculated

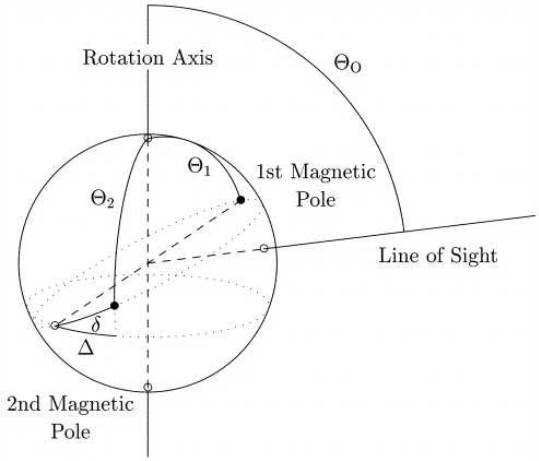

Figure 5.8: Possible scenario of a neutron star geometry with a distorted dipole geometry. The angles θ_0, θ_1 and θ_2 indicate the locations of the rotational axis and of the two magnetic poles.

numerically, and under the assumption of a geometry of the poles parameterizing the system (e.g. Kraus et al., 1995; Blum & Kraus, 2000, Fig. 5.8). Numerical calculations of X-ray pulsar continua and cyclotron line shapes which take into account this effect of gravitational light bending for simplified geometries have been realized, e.g., by Riffert & Mészáros (1988) and Mészáros & Riffert (1988). However, similar to the issue of seed photon angular distribution, no general picture has emerged so far for the geometry of beam patterns from both magnetic poles.

The MC model which is used here as introduced in chapter 4 does not include gravitational light deflection. Therefore a toy model approach was taken to illustrate the qualitative effects of mixing radiation contributions from two magnetic poles on the cyclotron line shapes. In Fig. 5.9, the effects of mixing two contributions of radiation, where the photons reaching the observer are governed by differently varying intrinsic escaping angles $\mu_{1,2}$ with phase, are illustrated. For the calculation of the sum of the observed spectra, it was assumed that both sources contribute equally into the direction of the line of sight of the observer. The single contributions and the sum of contributions is depicted for different phases of the observation. Clearly, mixing spectra from different angles will change the initial shapes of the lines. It is most interesting to note, however, that mixing two-pole spectra might effectively lead to more broad and shallow lines and can smear out the emission wings.

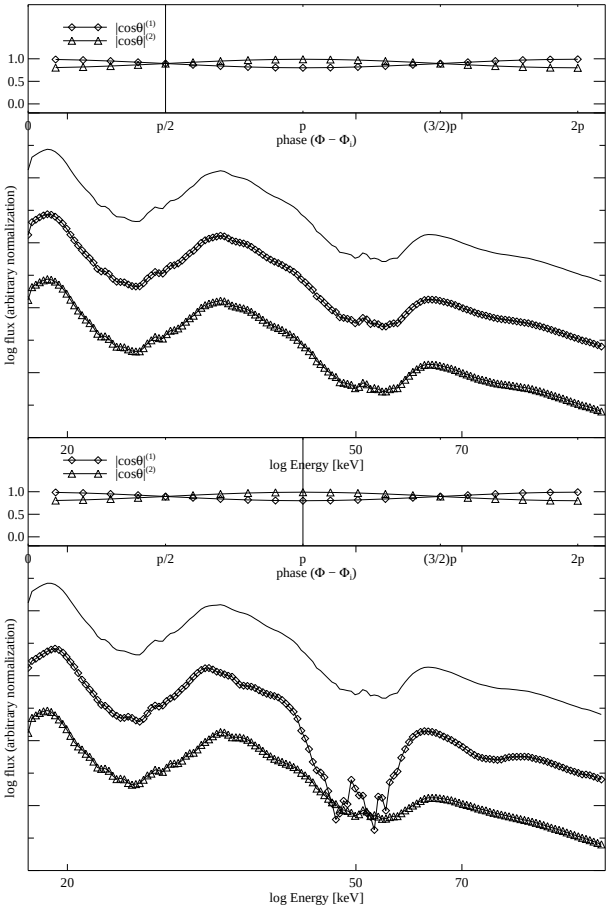

Figure 5.9: Effects of two-pole contributions. For a toy model geometry, the emerging spectra from two magnetic poles (diamonds and triangles) into the direction of the line of sight of an observer are shown together with the sum of both spectra (solid lines). The upper and lower panels represent two different rotational phases of the neutron star. The assumed variation of the observing angle with phase for both poles is illustrated in the small panels. The assumed values of the phase are indicated by the horizontal lines.

5.3 Line energies vs. magnetic field strength B

5.3.1 Uniform magnetic field

Line profiles for different magnetic field strengths and otherwise fixed parameters are shown in Fig. 5.10. The figure clearly shows the approximately linear progression of the centroid line energies towards higher energies with increasing magnetic field strength expected from equation (3.1). No significant change in the shape of the line ratios, however, is observed for magnetic fields varying between 5% and 8% of the critical magnetic field (Fig. 5.10). The relativistically correct line ratios for a uniform field are implied by Eq. (3.2). For some sources, e.g., V0332+53 (Pottschmidt et al., 2005) an agreement of the observed line ratios with the relativistic formula has been found.

5.3.2 Non-uniform magnetic field

As mentioned above, there are also sources for which the line energies of the harmonics are much less harmonically spaced than what can be accounted for by relativistic effects. One possible explanation is a model in which the magnetic field is varying locally within the line-forming region. Estimates of the dipole magnetic field of pulsars from torque theory and measurements of the surface magnetic field from CRSF detection hint at a magnetic field of more complex structure than a simple dipole. As the exact nature of the magnetic field is unknown, different scenarios for non-dipole magnetic field structure have been investigated (Blandford, Applegate & Hernquist, 1983; Urpin, Levshakov & Iakovlev, 1986; Arons, 1993). Besides magnetic field gradients which arise due to dipole variations with the height of the magnetosphere, surface field variations can result, e.g., from small-scale crustal field structures (Blandford, Applegate & Hernquist, 1983), or thermomagnetic field evolution effects (Urpin, Levshakov & Iakovlev, 1986). Nishimura (2005) recently presented a study of the line ratios for a line-forming region of slab geometry threaded by a magnetic field which linearly varies with the height. His approach was based on a model by Gil, Melikidze & Mitra (2002) who assumed the presence of a star-centered dipole from a fossil field in the core superposed by a crust-anchored dipole anomaly. Applying Feautrier methods to solve the radiative transfer, Nishimura (2005) found that the line ratios significantly increase if the B-field decreases upwards, and decrease vice versa. This toy model was adapted for a first study of magnetic field spread with the Monte Carlo approach taken here.

With some simplifying assumptions considering the geometry and the angular redistribution for the case of a non-constant B-field, this model confirms the trend of line ratio changes. An example is shown in Fig. 5.11, where cyclotron lines for a constant, a linearly decreasing, and a linearly increasing magnetic field are compared. The line shapes for a field gradient are obtained by multiple folding of a seed pho-

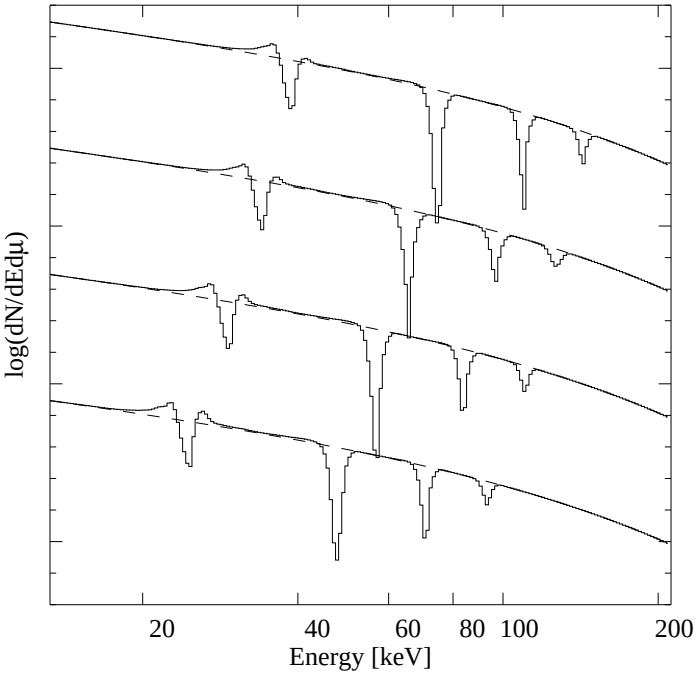

Figure 5.10: Line profiles for different values of the magnetic field strength. The B-field increases from bottom to top: $B/B_{\rm crit} = 0.05, 0.06, 0.07, 0.08$. We assume cylinder geometry, a constant temperature $kT_{\rm e} = 3$ keV, an optical depth $\tau_{\rm T} = 3 \cdot 10^{-3}$ and a viewing angle θ as $\mu = \cos\theta = 0.25$. The continuum spectrum has the shape of a power law with photon index $\alpha = 2.0$ and with an exponential cutoff at the energy $E_{\rm fold} = 40$ keV.

ton spectrum with the Green's functions, corresponding to the assumption of discrete steps of magnetic field variation for small $\Delta\tau_{\rm T}$ (compare Fig. 5.12). This approach of course implies an isotropic photon distribution again after each $\Delta\tau_{\rm T}$ step, which is not a correct physical assumption but still permits a qualitative assessment of B-field gradients. For the non-constant magnetic field, a linear variation of the field strength in discrete steps within the line-forming region of up to 10% was assumed. The fundamental line appears widely unchanged in shape and position, as it is formed in the upper scattering layers, where the non-constant B-field was set to have the same value as the constant one. Line photons which have been scattered out of the line of sight

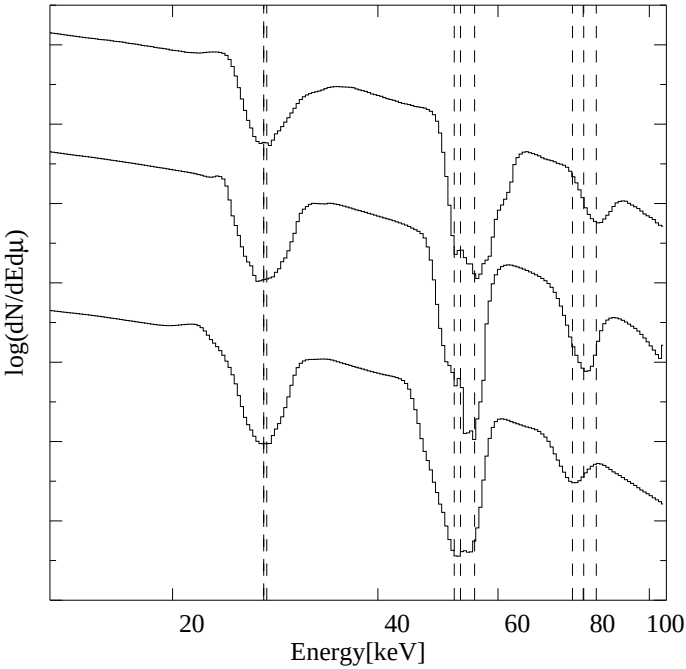

Figure 5.11: Comparison of CRSFs for a uniform and a non-uniform magnetic field in a line-forming region of slab geometry. Bottom: $B/B_{\rm crit} = 0.05 \rightarrow 0.055$, Middle: $B/B_{\rm crit} =$ const. $= 0.055$, Top: $B/B_{\rm crit} = 0.06 \rightarrow 0.055$. Results are shown for $\mu = \cos\theta = 0.6$. Otherwise the same setting as in Fig. 5.10 is used. The vertical dashed lines mark the line positions obtained from a phenomenological fit (continuum multiplied by three Lorentzians in absorption for the lines and two Lorentzians in emission for the emission wings of the fundamental line) of the first three CRSFs. The structure in the second line is assumed to be of statistical nature.

or redistributed in energy in lower layers are replaced by spawned photons from scattering in higher layers. By contrast, the higher harmonic lines change in position and shape. Here, contributions from all layers of different depth are important for the final line profile. Absorption features from photons at low layers are not refilled. Hence, with the change of the resonant energies with the height of the line-forming region, the lines become wider (proportional to the amount of variation in B) and their final centroid energy is shifted. From fitting Lorentzians to the first three lines, the line

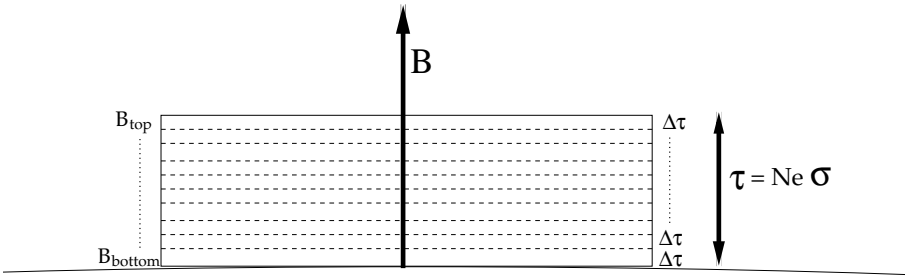

Figure 5.12: Toy model for a magnetic field gradient. Discrete thin slabs of different magnetic field strength and a small optical depth $\Delta\tau_{\rm T}$ are considered. The photons are propagated through the first slab slice by folding the continuum spectrum with the Green's functions for energy redistribution and $B_{\rm bottom}$; the emergent spectrum is folded again for the next value of B, and so on.

energies and line ratios for a constant, an increasing and a decreasing magnetic field could be obtained. Table 5.1 lists the fitted line positions and the fitted line ratios. The theoretical values of the line energies and line ratios after Eq. (3.2) are shown for completeness. As expected, these values are similar to the fitted ones for a constant magnetic field, although not identical, as the non-Gaussian and non-Lorentzian line shapes especially of the fundamental restrict the fit quality.

Larger deviations of the line ratios can be accounted for by assuming B-field variations of more than 10%. Line ratios of strongly non-harmonic nature have been observed. For 4U 0115+63, the observed spacing of the line energies is smaller than expected, yielding line ratios of ($2.8 \pm 0.05 : 1.9 \pm 0.05 : 1$, Santangelo et al., 1999) or ($2.71 \pm 0.13 : 1.73 \pm 0.08 : 1$, Heindl et al., 1999) for the first three harmonics.

Table 5.1: Comparison of line positions and line ratios from the fits of the spectra shown in Fig. 5.11. The line energies are given in keV. For the case of a constant magnetic field, the line energies are also calculated from Eq. (3.2).

$B/B_{\rm crit}$	$1^{\rm st}$	$2^{\rm nd}$	$3^{\rm rd}$	line ratios
$0.050 \rightarrow 0.055$	27.20	51.76	77.16	$2.84 : 1.90 : 1$
0.055	27.20	52.87	80.14	$2.95 : 1.94 : 1$
$0.060 \rightarrow 0.055$	27.49	55.45	83.61	$3.04 : 2.02 : 1$
0.055 (Eq. 3.2)	27.62	54.35	80.27	$2.91 : 1.96 : 1$

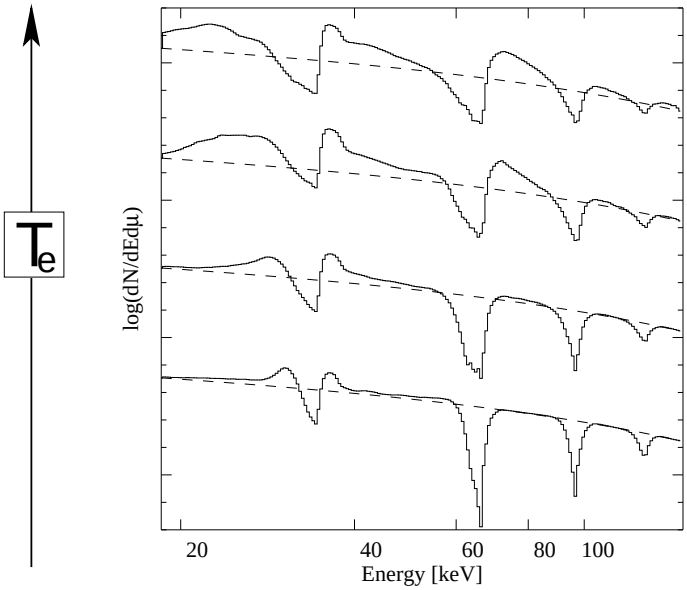

Figure 5.13: Variation of the line shapes with the plasma temperature ($kT_{\rm e} = 5, 10, 15, 20$ keV from bottom to top). Spectra are shown for a magnetic field $B/B_{\rm crit} = 0.07$ and otherwise the same parameters as in Fig. 5.10.

These deviations are comparable or slightly larger than the ones obtained for an increasing magnetic field in the example setting corresponding to Fig. 5.11. From the observational results, the line ratio changes can be attributed solely to the position of the fundamental line while the higher harmonics still obey a harmonic spacing. This behavior is in accordance with the obtained values for the line ratios for both an increasing or a decreasing magnetic field, due to the special role of the fundamental CRSF outlined above. An example for a source where the line ratios may be larger than what is expected from Eq. (3.2) is Vela X-1, where Kreykenbohm et al. (1999, 2002) have found a coupling of the first harmonic energy to the fundamental line energy $\gtrsim 2$ in *RXTE* data.

5.4 Influence of the plasma temperature

The line width is determined by the energy and angle-dependent shape of the scattering cross section and smeared out due to thermal Doppler broadening. In Fig. 5.13, cyclotron line shapes are depicted for a varying parallel electron temperature, T_e, for cylinder geometry and fixed parameters B and $\cos\theta$. The hotter the plasma, the wider and the more asymmetric become the lines. The width of the lines results from a combination of the natural line width and Doppler broadening (Harding & Lai, 2006). Doppler broadening gives a Full Width Half Maximum of (Trümper et al., 1977; Mészáros & Nagel, 1985a)

$$\Gamma_\mathrm{FWHM} = \sqrt{\frac{8\ln(2)kT_\mathrm{e}}{m_\mathrm{e}c^2}}|\cos\theta|\,E_\mathrm{cyc}\,. \tag{5.2}$$

For increasing $\cos\theta$ the line shapes become more asymmetric. In the simulations the plasma temperature is a free parameter. The approximate relation from theory (Lamb, Wang & Wasserman, 1990; Isenberg, Lamb & Wang, 1998b, compare chapter 4),

$$kT_\mathrm{e} = E_\mathrm{cyc}/4\ (\tau_\mathrm{cyc} \gg 1)\,. \tag{5.3}$$

would correspond to a temperature for the depicted setting ($E_\mathrm{cyc} \sim 30\,\mathrm{keV}$) of at least $6\,\mathrm{keV}$, i.e., somewhere in between the bottom spectrum and the second spectrum from the bottom in Fig. 5.13.

5.5 Continuum shape and photon spawning

The shape of the cyclotron lines is sensitive to the continuum shape. In particular, the fundamental line shape and its emission features vary significantly. For better illustration, the case of internally irradiated plasmas is investigated where the emission wings are strongest. The dependence of the line shapes on the continuum can be understood when considering the photon redistribution in energy, especially due to photon spawning. Figure 5.14 shows the change of the line profiles for a flat input continuum spectrum, when allowing only for electron transitions between the ground Landau state to the first Landau level, or for photon-electron scattering leading to up to three harmonics. In the former case, a single absorption line forms. The more harmonic scatterings are allowed for, the more lines form, while the fundamental and lower harmonics become shallower with growing emission wings. Integrating the photon flux only over the energy range including just the fundamental line and its emission wings ($E \leq 18\,\mathrm{keV}\,B_{12}$), gives the percentage of spawned photons in the spectra. The spawned photons account for as much as 34, 64, 73 % ($n \leq 2, 3, 4$) of

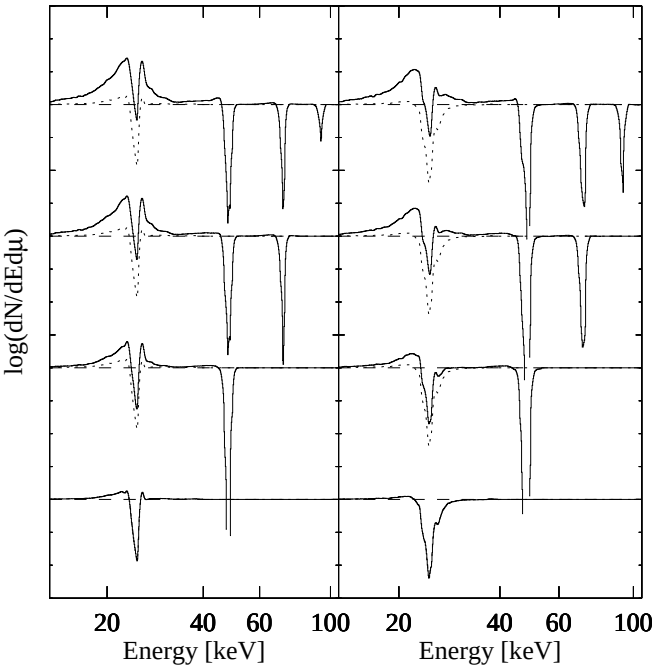

Figure 5.14: Changes of the line profiles considering one to three harmonics for the scattering processes (bottom to top). The bottom graph is overplotted in all cases as a dotted line to guide the eye. The input continuum spectrum (dashed line) is flat and therefore overemphasizes the effects of emission wings. Left panel: cylinder geometry; right panel: slab 1-1 geometry. In both panels, $kT_{\rm e} = 3\,{\rm keV}$, $\cos\theta \in [0.125, 0.250)$, $\tau_{\rm T} = 3 \cdot 10^{-3}$ and $B/B_{\rm crit} = 0.05$.

the flux for cylinder and for 11, 32, 43 % of the flux for slab 1-1 geometry. Considering the whole energy range, the percentage of spawned photons is 25, 52, 65 % of the total flux for cylinder and 3, 15, 25 % of the total flux for slab 1-1 geometry. It is important to stress that these numbers are representative of the extreme and fairly unrealistic case of a flat input continuum. However, they illustrate well that the line shapes change with the spectral hardness of the incident continuum, where harder spectra exhibit more emission features near shallower lines. Line profiles for a power law with photon index $\alpha = 1$ with exponential rolloff at different folding energies $E_{\rm fold} = 5, 15\,{\rm keV}$, and for a pure power law continuum spectrum are shown in Fig.

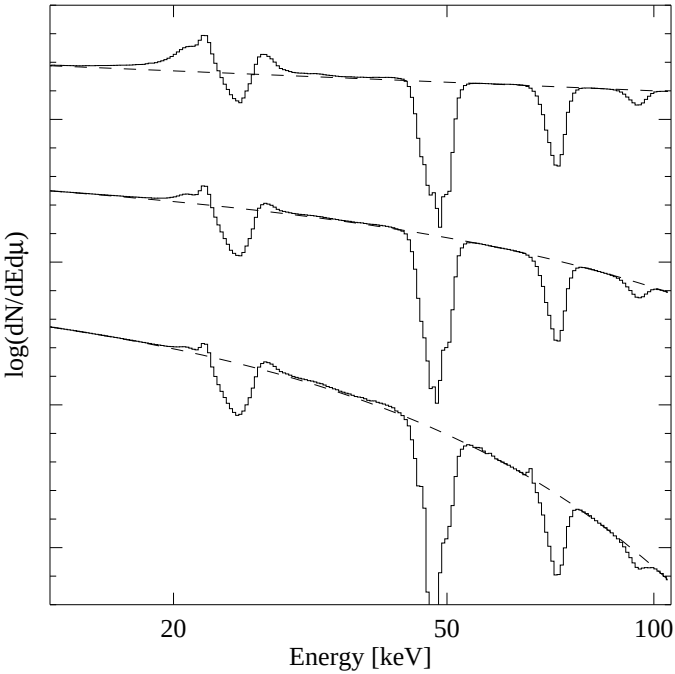

Figure 5.15: Line profiles for different continua. All continua have the general form of a power law with a photon index $\alpha = 1.0$ (top). In the middle and bottom plots, the spectra have an additional high energy cutoff at the folding energies $E_{\rm fold} = 15\,{\rm keV}$ for the middle and $E_{\rm fold} = 5\,{\rm keV}$ for the bottom plot. We show the results for cylinder geometry, $kT_{\rm e} = 3\,{\rm keV}$, $\cos\theta \in [0.375, 0.500)$, $\tau_{\rm T} = 3 \cdot 10^{-3}$, and $B/B_{\rm crit} = 0.05$.

5.15. In this case, the number of photons around the first line increases by a factor of 1.1 and 2.2 for the two harder spectra with respect to the softer one.

CHAPTER 6

Comparison with observations

A major aim of this work is a direct comparison of the simulated line features with observational data beyond the theoretical predictions, which were discussed in the last chapter. Such comparisons have been attempted before (e.g., Mészáros, 1984), however, only for very restricted data sets, and not in a way such that they could be generalized for observational applications.

The approach taken here is threefold: First, a short overview is given over some current X- and gamma-ray observatories and instruments, which provide data of cyclotron line sources, and a selected sample of sources is introduced. Second, synthetic spectra are calculated for these sources on the basis of their observational characteristics. The issue of observability of the line features by today's instruments is discussed. Third, a general model application, based on the numerical simulations, is introduced which allows for systematic fitting of real observed source data. This model can be provided to the scientific community by its implementation for the fitting analysis software package *XSPEC*. Fit results from three sources out of the sample are obtained and the implications of the obtained parameters for modeling cyclotron lines are discussed.

6.1 Instruments

When comparing synthetic spectra to real observational data, one always encounters a basic difficulty: the observed data points depend not only on the physical source properties but also on the instrumental characteristics. The instrumental response function and the source luminosity limit the detectability of less prominent features in spectral data. For the case of accreting X-ray pulsars, in particular the high-energy part of the spectrum suffers from low statistics due to their high-energy roll-offs (compare section 2.5). Background radiation affects the data. In order to compare the synthetic spectra to real observed source data, it is therefore necessary to fold the theoretical model spectrum with the corresponding instrumental response.

At present, three main X- and gamma-ray observatories are in operation: the Rossi

Table 6.1: Instrumental characteristics of *RXTE*, *INTEGRAL* and *Suzaku* (*RXTE*: `http://heasarc.gsfc.nasa.gov/docs/xte/`; *INTEGRAL*: `http://sci.esa.int`; *Suzaku*: `www.astro.isas.ac.jp/suzaku`).

	RXTE	*INTEGRAL*	*Suzaku*
energy range	*PCA*: 2–60 keV *HEXTE*: 15–250 keV	*IBIS*: 15 keV–10 MeV *SPI*: 20 keV–8 MeV	*XIS*: 0.2–12 keV *HXD*: 10–600 keV
$\Delta E/E$	*PCA*: $<$ 18%@6keV *HEXTE*: 15%@60keV	*IBIS*: 9 keV@100 keV *SPI*: 2.3 keV@1.3 MeV	*XIS*: 130 eV@6 keV *HXD*:4 keV ($<$ 60 keV)
effective area	*PCA*: $\sim 6500\,\mathrm{cm}^2$ *HEXTE*: $2\times800\,\mathrm{cm}^2$	*IBIS*: $\sim 3000\,\mathrm{cm}^2$ *SPI*:$\sim 500\,\mathrm{cm}^2$	*XIS*: $\lesssim 390\,\mathrm{cm}^2$ *HXD*: 160–260 cm^2
FOV	*PCA*: 1° *HEXTE*: 1°	*IBIS*: $9^\circ \times 9^\circ$ *SPI*: 16°	*XIS*: $17.8' \times 17.8'$ *HXD*: $34' \times 34'$ ($\lesssim$ 100 keV)
angular resolution	*PCA*: 1° *HEXTE*: 1°	*IBIS*: $12'$ *SPI*: 2.5°	*XIS*: $2'$ *HXD*: $34'$
timing accuracy	*PCA*: 1μs *HEXTE*: 8μs	*IBIS*: $\sim$ 1 ms *SPI*: 129μs	*XIS*: 8 ms–8 s *HXD*: 61 μs

X-ray timing explorer (*RXTE*, launch date: 12-30-1995), the International Gamma ray Astrophysics Laboratory (*INTEGRAL*, launch date: 10-17-2002), and the Japanese high-energy observatory *Suzaku*[1] (launch date: 07-10-2005). Accreting X-ray pulsars are regular targets of observation by the instruments of those satellites. Additional to new observational data, a large amount of archival data of accreting X-ray pulsars has been accumulated during the last decades. Among past instruments and satellites are the High Energy X-Ray Experiment (*HEXE*, on a balloon and on MIR flights), *Ginga*[2], the High-Energy Astronomy Observatories (*HEAO*), the Compton Gamma-Ray Observatory (*CGRO*), and the Italian-Dutch satellite *BeppoSAX*. In the scope of this work, spectra extracted from *INTEGRAL*, *RXTE*, and *Suzaku* data are considered. Some basic properties of those satellites are summarized in table 6.1. The listed instrument characteristics are nominal. Useful ranges have been obtained from experience. For instance, considering the instruments on *RXTE*, the energy range of the Proportional Counter Array (*PCA*) is given as 2–60 keV. However, a useful range turned out to be 2 to 25 keV due to calibration problems of the Xenon K edge structure (Rothschild et al., 2006). Hence for studies of cyclotron lines above 25 keV, the High-Energy X-ray Timing Experiment (*HEXTE*) should be the instrument of choice. For the *IBIS/ISGRI* instrument on *INTEGRAL* there is some long ongoing discussion on the validity of the response in the low-energy regime ($<$ 20 keV). For the cyclotron line energies discussed here, this should not influence the results.

[1] Suzaku is a mythical, divine bird symbolizing renewal.

[2] Japanese for 'Galaxy'

6.2 Source sample

All sources considered in the following are accreting X-ray binaries, for which one or several cyclotron resonance scattering features have been firmly detected in their spectral data, confirmed by several different investigators and different instruments. From the seven objects presented below, three belong to the predominant class of transient sources, which accrete mass via a Be mechanism and are only observable during recurring outburst events (see chapter 1). Her X-1 is an example for a close binary where Roche lobe overflow and disk accretion mechanisms prevail while Vela X-1 is a typical example for a strong wind accretor. In general, the motivation behind the choice of sources was to achieve a sample representative of a variety of different source properties (compare the 'key results' listed in the introductory chapter) and to consider well-studied sources, for which several observations by different instruments, and over a long time have been performed, and high-quality spectral data is available. For each source, a short summary of its general characterstics is given, and a set of synthetic spectra is shown.

Her X-1.

Her X-1 is not only the first accreting X-ray pulsar ever for which a spectral feature was discovered and identified as a CRSF (Trümper et al., 1978) but also one of the best-studied objects up to date (Staubert et al., 2007). The close X-ray binary contains the $1.3\,M_\odot$ pulsar Her X-1 and its optical $2.2\,M_\odot$ companion star HZ Her. The binary system has an orbital period of 1.7 days. Its inclination is believed to be $i > 80\,\mathrm{deg}$ (Klochkov et al., 2006). The close binary is thought to accrete via Roche lobe overflow and under the formation of an accretion disk. The pulse period of Her X-1 was determined to $P = 1.24\,\mathrm{s}$. A long-term variability with a 35 days cycle (Deeter et al., 1998) is observed for Her X-1. This cycle is nowadays attributed to a periodical obscuration of the neutron star and the inner disk due to a warped accretion disk (Shakura et al., 1999; Klochkov et al., 2006). The pulse profile of Her X-1 is highly asymmetric, and varies not only with the choice of energy band but also with its 35 days cycle. Different explanations for its asymmetry have been sought in form of an asymmetric fan beam pattern scenario or by the picture of non-antipodal emission regions (distorted dipole model; Blum & Kraus, 2000). During its main-on state, Her X-1 reaches an X-ray luminosity of $L_X = 2.5 \cdot 10^{37}$ ergs s^{-1}, making it one of the brightest LMXBs. Its magnetic field was measured via a cyclotron line at $\sim$41 keV (Gruber et al., 2001) as $B \sim 4.4 \cdot 10^{12}$ Gauss. It is intriguing to note that a sudden jump of the line position occurred around 1991. Before, the fundamental CRSF was repeatedly measured around 35 keV, indicating a weaker magnetic field of $B \sim 3.8 \cdot 10^{12}$ Gauss (Staubert et al., 2007). Recently, studies of the luminosity dependence of the Her X-1 cyclotron line have been presented. Staubert et al. (2007)

found an increase of the energy of the fundamental CRSF with the luminosity; this detection was of special interest as it implied for the first time a positive correlation of those parameters (compare section 3.3).

V0332+53.

The Be type high-mass X-ray binary V0332+53 is a transient X-ray pulsar which consists of the O8-9Ve star BQ Cam and a neutron star. Discovered in 1983 (Tanaka, 1983), V0332+53 was the fourth accreting X-ray pulsar system where CRSFs were found (Makishima et al., 1990a,b). It is also the second accreting X-ray pulsar after 4U 0115+63 with a detection of more than two cyclotron lines in its spectrum. The third CRSF for V0332+53 was discovered in *RXTE* data (Coburn et al., 2005; Pottschmidt et al., 2005) and confirmed by subsequent *INTEGRAL* observations (Kreykenbohm et al., 2005). These data from its 2005 outburst exhibit very pronounced cyclotron lines at 27, 51 and 74 keV, indicating a surface magnetic field of $\sim 2.7 \cdot 10^{12}$ Gauss for a redshift $z = 0.3$. Studying the evolution of V0332+53 over the outburst, the fundamental CRSF was found to vary with the source luminosity. With the decrease of the X-ray flux from a peak value of $\sim$1 Crab to $\sim$0.01 Crab during the outburst decline, a clear increase of line energy and line depth along with a decreasing line width was found (Tsygankov et al., 2006; Mowlavi et al., 2006). The anticorrelation of $E_{\rm cyc}$ and the source flux had been interpreted before by Mihara, Makishima & Nagase (1998) for 4U 0115+63, Cep X-4 and V0332+53 as due to a change in the height of the shock and the X-ray emitting region with varying mass accretion rate, $\dot{M}$ (compare section 3.3).

A 0535+26.

A 0535+26 is another example for a transient high-mass Be/X-ray binary. It was discovered in 1975 during a giant outburst at a luminosity $L_{(3-7)\rm keV} = 1.2 \cdot 10^{37}$ergs s^{-1} (Rosenberg et al., 1975). During the last 30 years five more giant outbursts and two normal outbursts have been observed. The X-ray pulsar has a pulse period of $P = 103$ s. It is in a highly eccentric orbit ($e = 0.47$) of $P_{\rm orb} = 111$ days duration. A magnetic field of $4.9 \cdot 10^{12}$ G ($z = 0.3$), inferred from the fundamental CRSF at 46 keV in the spectrum of the A0535+26 makes the source the accreting X-ray pulsar with the highest magnetic field so far determined. A long ongoing discussion has taken place about the energy of its fundamental CRSF which started after the claims of the detection of up to two lines (Kendziorra et al., 1994; Grove et al., 1995) in its spectra data during outbursts in 1989 and 1994. After that, and after more than ten years of quiescence, another series of outbursts was observed in between May 2005 and January 2006 (Kretschmar et al., 2005; Terada et al., 2006), allowing for a firm detection of two lines at $\sim$46 and $\sim$100 keV in *RXTE* (Wilson & Finger, 2005) and

INTEGRAL (Kretschmar et al., 2005; Caballero et al., 2007) data. Similar to other sources like Vela X-1, a fainter fundamental CRSF and a more pronounced second CRSF are observed for A0535+26. However the fundamental seems to be especially shallow and broad for this source. Opposed to V0332+53, no variation in $E_{\rm cyc}$ with the luminosity was detected so far (Caballero et al., 2007), although there are first hints at a sudden jump in the line energy from the pre-outburst peak to the main peak (I. Caballero, priv. com.) in the 2005 spectra.

4U 0115+63.

While A0535+26 marks the upper range of $E_{\rm cyc}$ detected for accreting X-ray pulsars, the Be/X-ray binary transient pulsar 4U 0115+63, is the source with the so far lowest cyclotron line energy which has been observed among those sources (compare section 3.3). An impressive number of five cyclotron resonance scattering features has been detected in the spectra of this source (Heindl et al., 1999; Santangelo et al., 1999). It is not surprising that the record in the number of CRSFs is held by the source with the lowest determined B-field. The higher the magnetic field, the higher are the energies of all harmonics, while a high-energy cutoff behavior seen for X-ray pulsars limits severely the statistics at high energies. The first of the absorption features of 4U 0115+63 was discovered at $20\,$keV by Wheaton et al. (1979) only shortly after the first ever discovery of a CRSF in Her X-1. A more detailed analysis of the data by White, Swank & Holt (1983) revealed the presence of in fact two CRSFs at 11.5 and $23\,$keV. An outburst of 4U 0115+63 sixteen years later increased this number to a striking five CRSFs found in the spectral data obtained by instruments on the *RXTE* (Heindl et al., 1999) and *BeppoSAX* (Santangelo et al., 1999) observatories. 4U 0115+63 is hence the best candidate for probing intercorrelations of the line parameters of the harmonics, in particular concerning the quasi-harmonic ratios of the lines. For 4U 0115+63, the observed line ratios ($E_n : E_{\rm cyc}$) seem to deviate from the predictions of Eq. (3.2). These deviations were ascribed to a change of the fundamental line position alone, as the higher harmonics still obey a quasi-linear spacing. A possible explanation for line ratio changes is the scenario of a magnetic field which varies significantly within the line-forming region (compare section 5.3.2, and see Nishimura, 2005). Furthermore, phase resolved spectroscopy reveals a significant change of the line-energies with phase, indicating magnetic field changes of 20 % during one period.

Vela X-1.

The close high-mass X-ray binary Vela X-1 is a typical example of a wind accretor. It consists of a $1.8\,M_\odot$ neutron star and a $23 M_\odot$ B0.5Ib supergiant, HD 77581 with an orbital separation of only 1.7 neutron star radii and an orbital period of ~ 9 days

(van Kerkwijk et al., 1995). This small separation of the two binary partners implies the exposure of the neutron star to a very strong stellar wind with a mass-loss rate estimated as $4 \cdot 10^{-5} M_{\odot}\mathrm{yr}^{-1}$ (Nagase et al., 1986). Vela X-1 has an X-ray luminosity of $4 \cdot 10^{36}$ergs s^{-1}, which is a typical value for an X-ray pulsar. Vela X-1 shows high variability in the flux as flares (Staubert et al., 2004; Kreykenbohm et al., 2006) and intense outbursts (Krivonos et al., 2003). Changes in the luminosity are believed to result either from absorption by clumps of matter around the neutron star, or by a change in the mass accretion rate itself. Observations of the system are used to further probe the circumstellar matter structure (Watanabe et al., 2006). The pulsar spins with a period of about 283 s. The spectrum of Vela X-1 exhibits two CRSFs at 25 and 55 keV. Also for this source, the existence of the fundamental line at 25 keV was a matter of debate. Several studies claiming just one 55 keV line (e.g. Kendziorra et al., 1992; Orlandini et al., 1998a; La Barbera et al., 2003) or in favor of two lines (e.g. Mihara, 1995; Kretschmar et al., 1997; Kreykenbohm et al., 2002) have been published. Recent analyses of *INTEGRAL* data strengthens the presence of two lines at about 23–27 and 53 keV (Schanne et al., 2007, P. Kretschmar, priv. com.). A fundamental line at 25 keV would imply a surface magnetic field of $2.7 \cdot 10^{12}$ Gauss ($z = 0.3$).

4U 1907+09.

4U 1907+09 is a wind-accreting HMXB system (Giacconi et al., 1971b; Fritz et al., 2006), containing a neutron star of spin period ~ 440 s in an eccentric orbit of $P_{\mathrm{orb}} = 8.4$ d (in't Zand et al., 1998) around a type O8-O9 star (Cox, Kaper & Mokiem, 2005). Initial speculations about a possible Be companion (Makishima et al., 1984; Cook & Page, 1987) were ruled out by distance measurements exceeding by far the < 1.5 kpc restriction required for a Be classification of this source (Fritz et al., 2006). A new lower limit of its distance was set recently as 5 kpc by Cox, Kaper & Mokiem (2005), yielding a lower limit on its X-ray luminosity above 1 keV of $L = 2 \cdot 10^{36}$ ergs s^{-1} (in't Zand et al., 1998). A mass loss rate of $\dot{M} \sim 7 \cdot 10^{-6}\, M_{\odot}$ yr^{-1} was estimated for the stellar wind of the companion (Cox, Kaper & Mokiem, 2005; van Kerkwijk, van Oijen & van den Heuvel, 1989). Long-term studies of 4U 1907+09 have revealed a torque reversal from a spin-up to a spin-down trend of this system (Fritz et al., 2006). 4U 1907+09 is one of the sources where multiple cyclotron lines have been observed: Two CRSFs were detected for this source at 19 and 39 keV (Mihara, 1995; Cusumano et al., 1998) by *Ginga* and *BeppoSAX*, and confirmed by *INTEGRAL* (Fritz et al., 2006).

Cen X-3.

Cen X-3, the first accreting X-ray pulsar ever discovered (Giacconi et al., 1971a; Schreier et al., 1972), is a high-mass X-ray binary with the O6-O8 supergiant companion V779 Cen (Hutchings et al., 1979). The pulsar has a spin period of $P = 4.8\,\mathrm{s}$ and an orbital period of $2.1\,\mathrm{d}$ (Burderi et al., 2001; Nagase, 1989). Eclipses of 20 % of the orbital period are seen in the X-ray light curve (Burderi et al., 2001). The system's luminosity is estimated as 10^{37}–$10^{38}\,\mathrm{ergs\,s^{-1}}$ (Nagase et al., 1992; White, Swank & Holt, 1983), assuming a distance of $8\,\mathrm{kpc}$ (Krzeminski, 1974). A cyclotron line was detected at $\sim$30 keV (Santangelo et al., 1998) which is highly variable with the spin phase, varying from $\sim$27 to $\sim$40 keV (Burderi et al., 2001; Suchy et al., 2007). Also, the cyclotron line energy was observed to have a strong asymmetric dependence on the pulse shape (Suchy et al., 2007; Burderi et al., 2001), with its maximum in the rising pulse and decreasing along the pulse phase. Also, other line parameters like the line width strongly vary with the pulse phase (Suchy et al., 2007).

6.3 Calculation of synthetic spectra

For the preparation of synthetic spectra for these sources, the input parameters for the Green's functions convolution model, i.e. the magnetic field strength, B, the parallel electron temperature kT_e, the incident angle of the emerging photons θ ($\mu = \cos\theta$), the basic geometry, and the gravitational redshift at the height of the line-forming region, z, are required. The redshift is necessary to transfer the observed properties to the initial neutron star system for which the Green's functions were simulated. Unfortunately, there is no straightforward way to assess this complete set of parameters from observational results obtained from phenomenological data modeling. Some general assumptions have to be made. To begin with, the magnetic field strength, the value of z, and the observed fundamental line energy E_cyc are correlated. The gravitational redshift is by no means well determined for X-ray pulsars. In order to yield comparable results for all sources, z will be assumed to have a value of 0.3, representative for typical neutron star parameters, in the following. The magnetic field B may then be approximated by applying the 12-B-12 rule (3.1) to the energy of the fundamental CRSF, as determined from phenomenological fits of eligible spectral data. A more precise determination of B from observational studies using the relativistic formula (3.2) is not considered advantageous for the following reasons: first of all, the choice of one observational data set for each source introduces some randomness to E_cyc and B, as these are known to vary for many different reasons for one source. Even if the synthetic spectra were meant to be tuned to this one eligible observational data set, the cyclotron line energy obtained phenomenologically identifies not more than the peak energy of a Gaussian line fitted to a more complex line shape. It is

important to stress that it is not a precise measurement of the physical $E_{\rm cyc}$. Also, the lacking knowledge about the viewing geometry $\mu = \cos\theta$ renders the application of equation (3.2) problematic. It is in principle possible to assess the range of μ from measuring the line-ratios of the CRSFs, however, only under the simplifying assumption of (a) a homogeneous B-field within the line-forming region, (b) an ideal phase resolved spectrum and (c) assuming that the observed radiation has originated from just one magnetic pole. This is a rather idealized scenario, in particular taking studies into account which have shown that for some sources varying B-fields are required to explain the observed line ratios, and that a line ratio change in this scenario can be much more significant than the line ratio dependence on the angle. Furthermore, even in phase-resolved spectroscopy, not only possible two-pole contributions but also the size of the phase bins naturally introduces a mixing of photons emerging from different angles with respect to the magnetic field. A similar problem arises for the determination of the plasma temperature. Although desirable, there is no way so far to obtain the plasma temperature unambiguously from the continuum parameters, which, like the line parameters, are of phenomenological nature. The most straightforward approach would be the estimation of the plasma temperature from the effects of Doppler broadening on the line widths. Again, this is complicated by the relativistic angle dependency. In addition, the natural line width has to be considered. Higher harmonic features are also broadened for the case of variable B-fields. The geometrical setting is another uncertainty of the picture. Theoretical studies promoting either the fan or the pencil beam scenario or a mixture of both scenarios have been suggested for several sources.

For all these (and more) reasons, the following simple ansatz was chosen as a first approach to assess the wealth of observational results: For each source, one observational study was chosen, in order to obtain the (order of the) fundamental line energy and to get a typical continuum spectral shape from the corresponding phenomenological best-fit parameters. The magnetic field strengths were estimated from eq. (3.1), and for $z = 0.3$. The parallel electron temperatures were estimated similar to relation (5.3), and to previous studies (Araya & Harding, 1999) as $kT_e = E_{\rm cyc}/4$. Table 6.2 lists the parameter details assumed for the eligible individual observational results for different sources along with the references to the relevant studies. Having chosen three out of five input parameters (B, $kT_{\rm e}$, $z = 0.3$), a set of 24 spectra resolved into eight angular bins and assuming three different geometries was produced for each individual source by convolution of the corresponding phenomenological continuum spectrum. For the chosen source sample, the complete set of spectra is depicted in Figs. 6.1 to 6.5. Two interesting points catch the eye: first, emission wings are indeed present in some cases. In chapter 5, a rather hard continuum was assumed ($E_{\rm fold} = 40\,$keV) in order to study the effect of emission wings and photon spawning. Figs. 6.1–6.7 extend the theoretical prediction of emission wings in hard spectra

also to more realistic X-ray pulsar spectra. Second, in between the line features, the continuum shape is always recovered, which so far cannot be clearly predicted from observational analysis of cyclotron line sources (A. Santangelo, priv. com.). Also, one notes that the position of the fundamental line in the synthetic spectra, calculated for a magnetic field using Eq. (3.2) (for which the magnetic field was approximated from observational results as $B_{12} \sim E_{\rm cyc}/11.6\,\mathrm{keV}$), is shifted with respect to the observed centroid energy at all angles. The wiggles at higher energies, e.g., in Fig. 6.7, are of statistical nature.

6.4 Observability of the predicted line features

The synthetic source spectra predict features which should be present in the intrinsic spectra of real sources. A different question, however, is the one of the observability of those features in observed source data, due to restrictions, e.g., in the energy resolution and error accuracy of the instruments. This question had already been posed by Isenberg, Lamb & Wang (1998b) considering the prediction of significant emission wings for some geometries at intermediate optical depths. However, no such related study has emerged up to date.

To assess the observability of the predicted shapes of cyclotron resonance scattering features, a source spectrum, folded with a real instrumental response function, was simulated. This analysis was realized using the spectral fitting package *XSPEC* version 11 (Arnaud, 1996). Fig. 6.8 shows the simulated spectrum for a source which was assigned an ideal spectrum of the form of the npex model, a negative and positive power law with a common high-energy cutoff (see section 2.5), folded with the Green's functions for a chosen set of parameters, $B_{12} = 3.0$, $kT_{\rm e} = 5.5\,\mathrm{keV}$, $\cos\theta = 0.5$, $\tau_{\rm T} = 5 \cdot 10^{-4}$, $z = 0.3$, and for slab 1-1 geometry. The flux is appropriate for typical HMXB observations. For an assumed observation time of 20 ks, this spectrum was folded with the *RXTE HEXTE* response, and background was added. Next, this fake spectrum was fitted with a npex component for the continuum. Two Gaussian absorption lines (Coburn et al., 2002) were then included to model the simulated CRSFs. Fig. 6.8 shows the fake data and the model resulting from this fit of continuum and lines, along with the corresponding residuals, compared to the residuals from a fit of only the continuum component. The residuals from the continuum shape represent the simulated line shapes as the same continuum component was used for the simulated and for the model spectrum. Fitting the first two lines with Gaussian absorption lines, the emission wings stay very pronounced in the residuals. For the simulated spectrum, the resonance energy of the fundamental CRSF is calculated from equation (3.2) as $E_1^{\rm obs} = 26.1\,\mathrm{keV}$. The Gaussian fit of the fundamental line gives a centroid energy of $24.77 \pm 0.03\,\mathrm{keV}$ instead. This results indicates that the

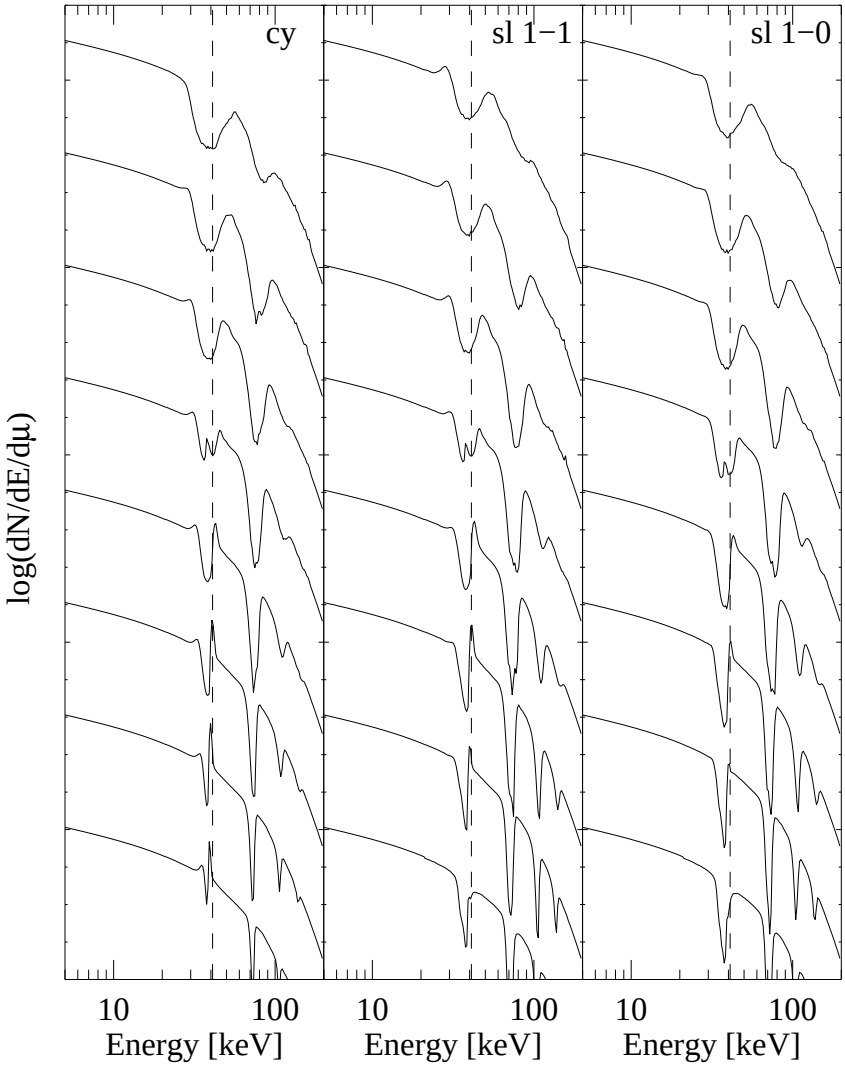

Figure 6.1: Synthetic spectra for Her X-1. Line features are shown for three geometries and eight angular bins (same as in Fig.5.1). The optical depth and redshift are prescribed as $\tau_{\rm T} = 1 \cdot 10^{-3}$ and $z = 0.3$. Continuum parameters and the fundamental line energy are taken from Gruber et al. (2001). The dashed line marks the observational value of $E_{\rm cyc}$ used to calculate $B_{12} \sim E_{\rm cyc}/11.6$.

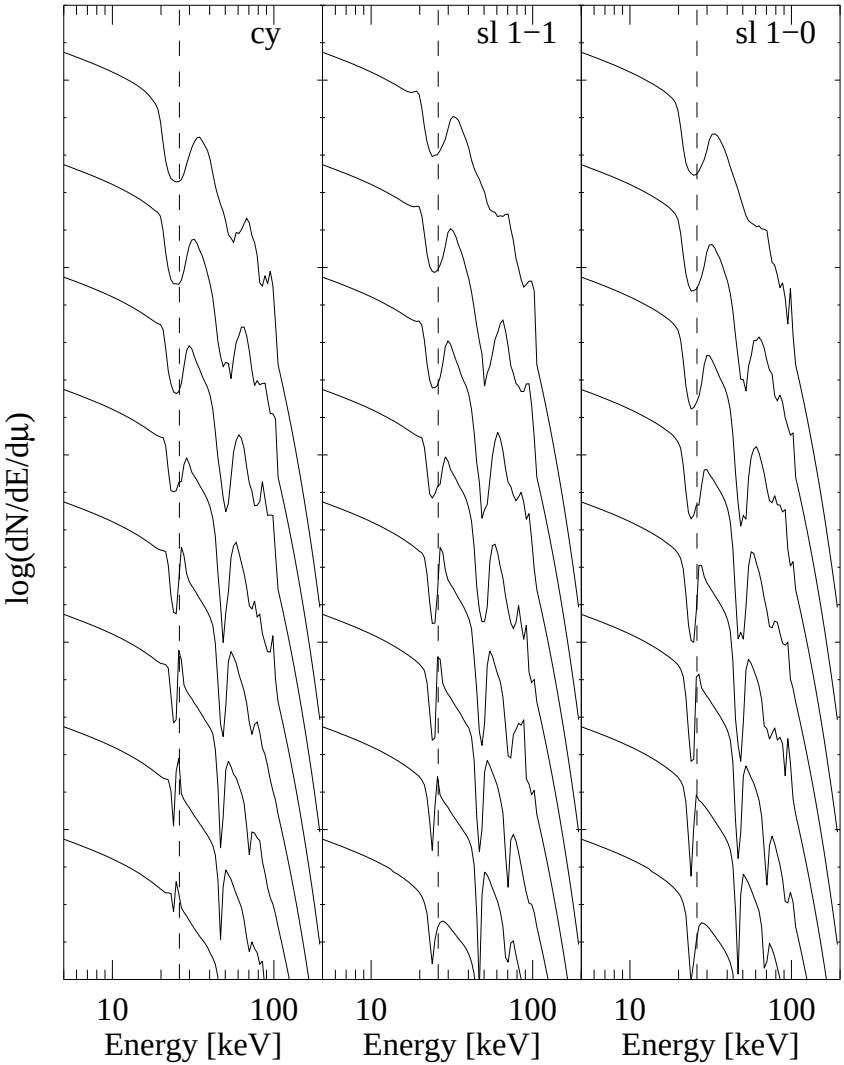

Figure 6.2: Synthetic spectra for V0332+53. The representation is the same as for Fig. 6.1. Continuum parameters and the fundamental line energy are taken from Pottschmidt et al. (2005).

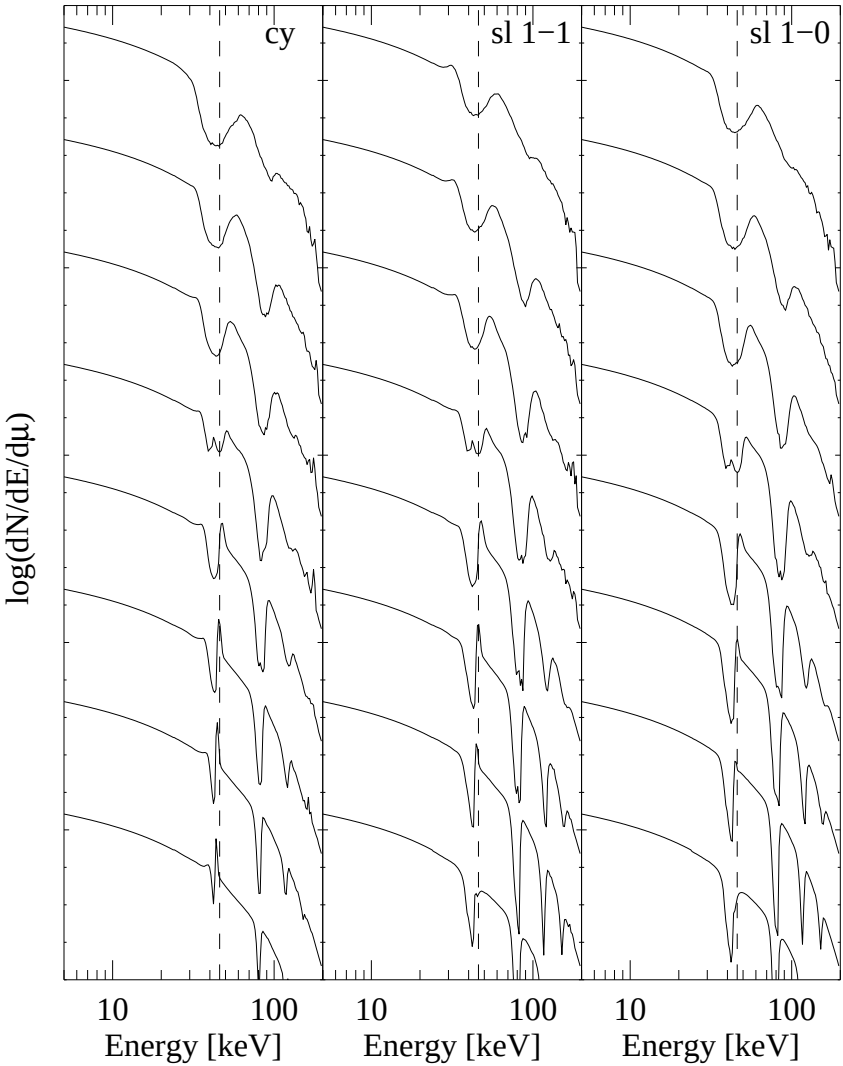

Figure 6.3: Synthetic spectra for A0535+26. The representation is the same as for Fig. 6.1. Continuum parameters and the fundamental line energy are taken from Caballero et al. (2007).

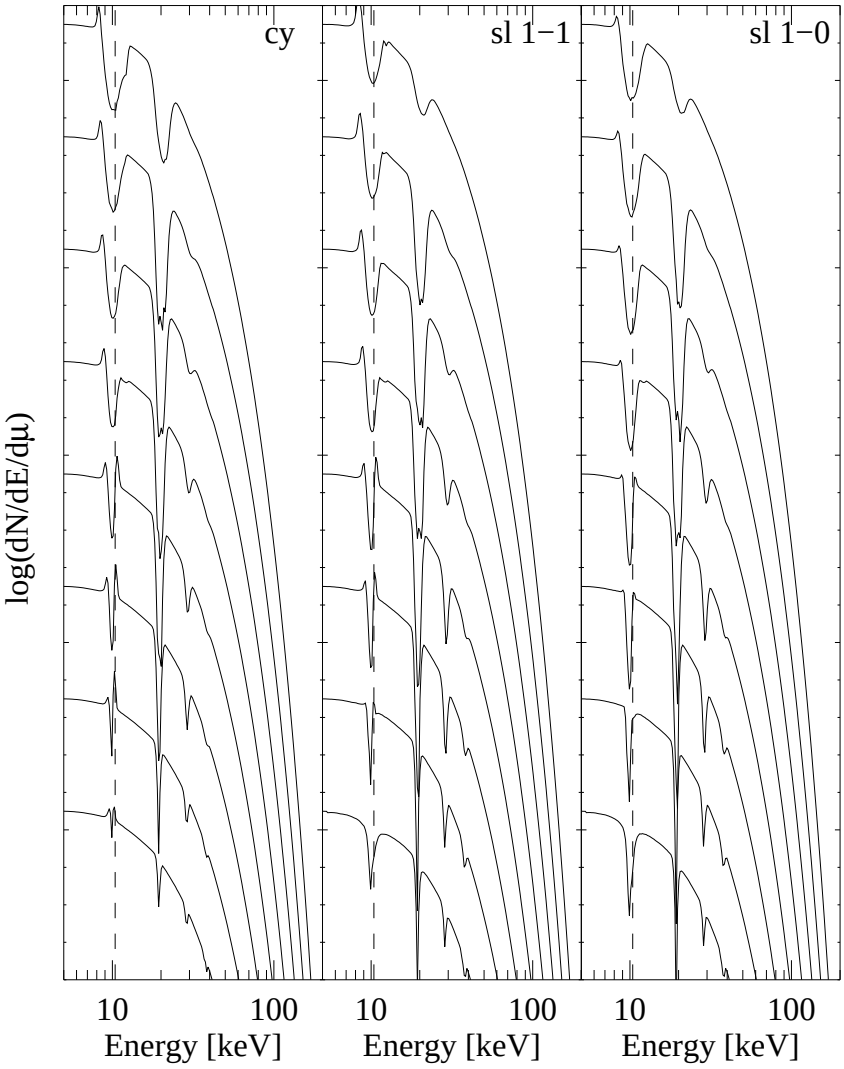

Figure 6.4: Synthetic spectra for 4U 0115+63. The representation is the same as for Fig. 6.1. Continuum parameters and the fundamental line energy are taken from Santangelo et al. (1999).

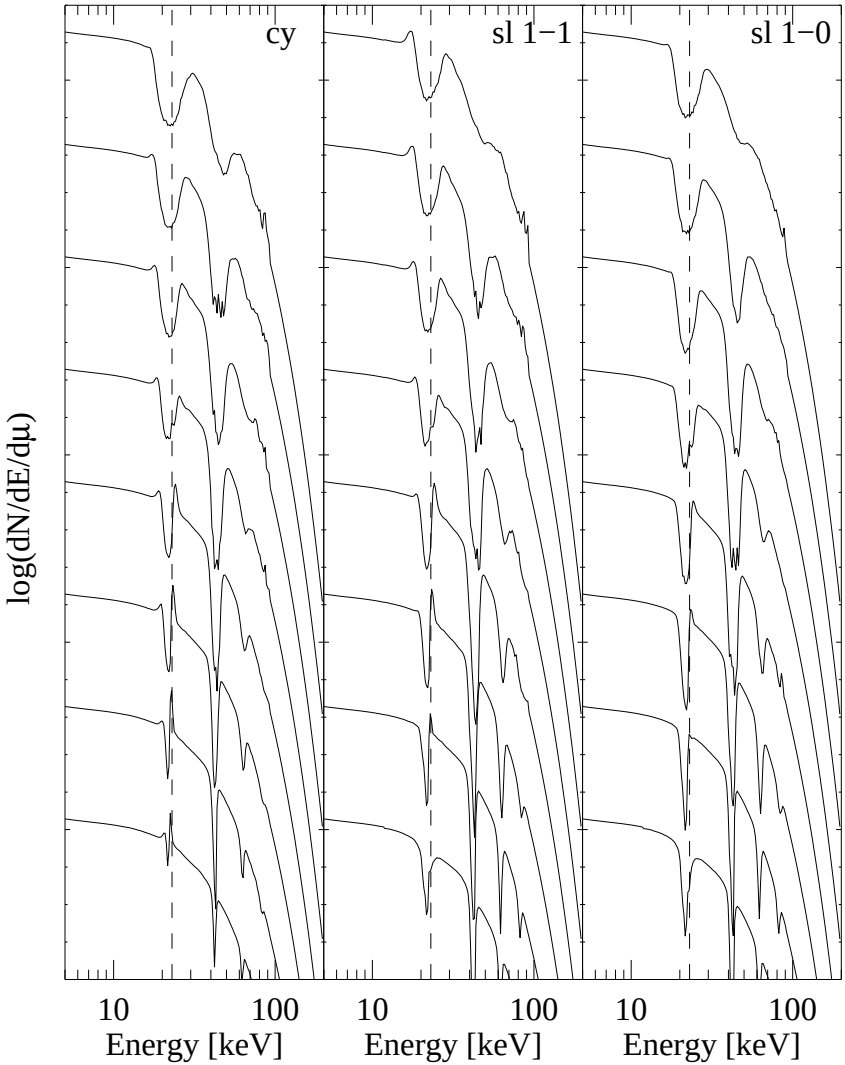

Figure 6.5: Synthetic spectra for Vela X-1. The representation is the same as for Fig. 6.1. Continuum parameters and the fundamental line energy are taken from Kreykenbohm et al. (2002).

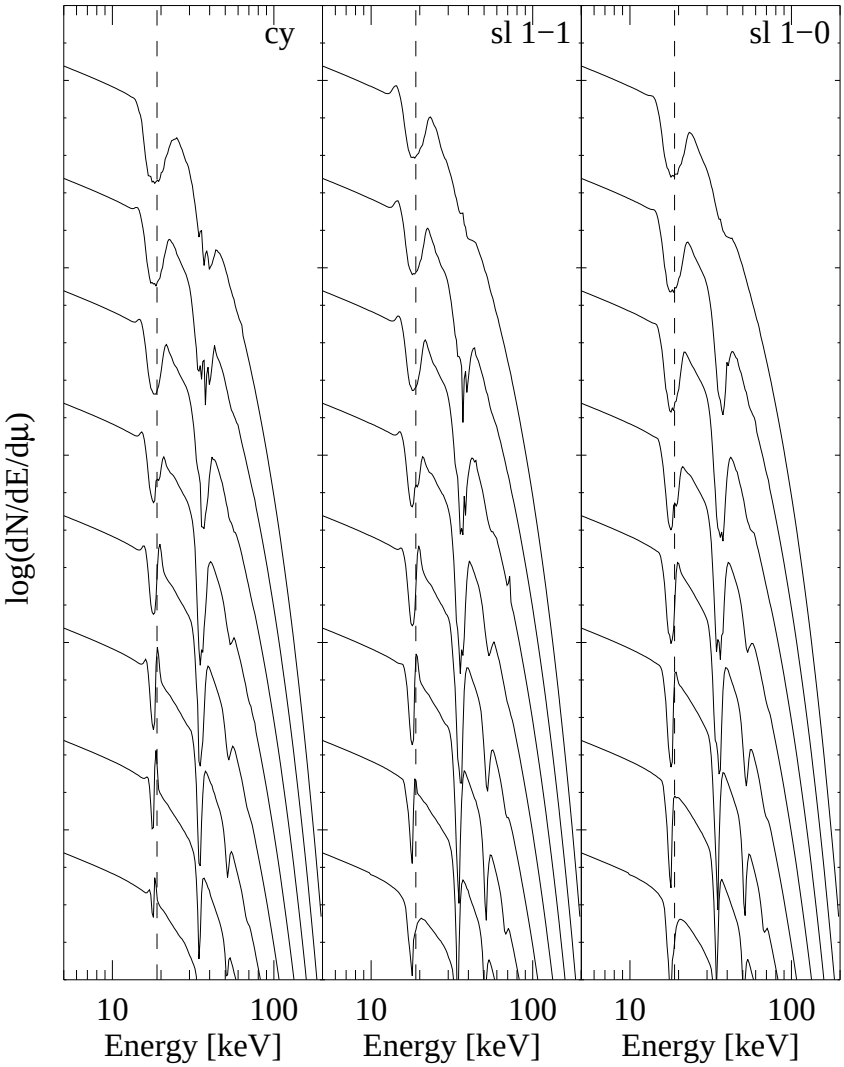

Figure 6.6: Synthetic spectra for 4U 1907+09. The representation is the same as for Fig. 6.1. Continuum parameters and the fundamental line energy are adapted from Fritz et al. (2006).

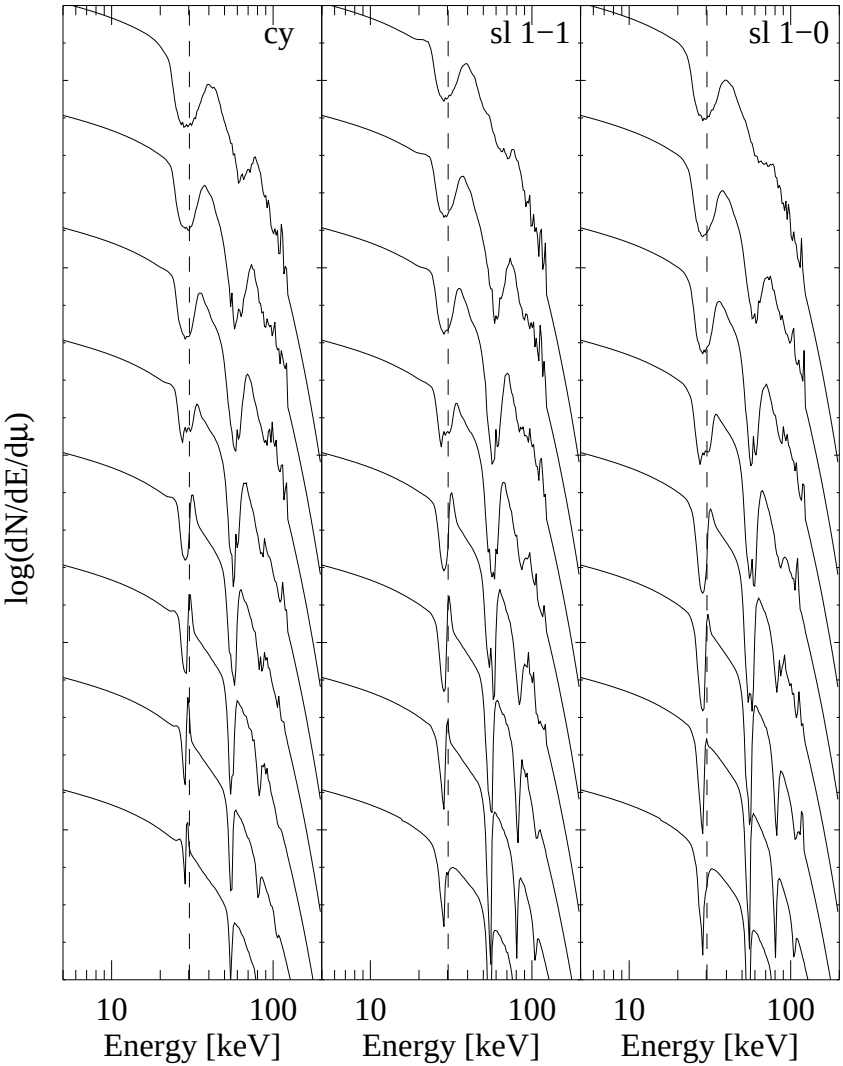

Figure 6.7: Synthetic spectra for Cen X-3. The representation is the same as for Fig. 6.1. Continuum parameters and the fundamental line energy are adapted from Suchy et al. (2007).

Table 6.2: Parameters used for adapting synthetic spectra to different sources. See Figs. 6.1 to 6.7.

object	$E_{\rm cyc}$ [keV]	continuum	Ref.
Her X-1	41	`fdcut(powerlaw)`, Eq. (2.15) $\alpha = 0.84$ $E_{\rm cut} = 19.6\,{\rm keV}$ $E_{\rm fold} = 10.8\,{\rm keV}$	Gruber et al. (2001) *RXTE*
V0332+53	26	`fdcut(powerlaw)` $\Gamma = 0.42$ $E_{\rm cut} = 17.2\,{\rm keV}$ $E_{\rm fold} = 8\,{\rm keV}$	Pottschmidt et al. (2005) *RXTE*
A0535+26	46	`cutoffpl`, Eq. (2.14) $\alpha = 0.51$ $E_{\rm fold} = 17.3\,{\rm keV}$	Caballero et al. (2007) *RXTE*
4U 0115+63	10.4	`npex`, Eq. (2.17) $\Gamma_1 = 1.27$ $\Gamma_2 = 2.$ $E_{\rm fold} = 5.76\,{\rm keV}$ $f = 0.016$	Nakajima et al. (2006) *RXTE*
Vela X-1	23	`npex` $\Gamma_1 = 0.58$ $\Gamma_2 = 2.$ $E_{\rm fold} = 6.\,{\rm keV}$ $f = 5.5 \cdot 10^{-3}$	Kreykenbohm et al. (2002) *RXTE*
4U 1907+09	18.9	`fdcut(powerlaw)` $\Gamma = 1.67$ $E_{\rm cut} = 30.0\,{\rm keV}$ $E_{\rm fold} = 7.0\,{\rm keV}$	Fritz et al. (2006) *INTEGRAL*
Cen X-3	30.3	`fdcut(powerlaw)` $\Gamma = 0.93$ $E_{\rm cut} = 13.2\,{\rm keV}$ $E_{\rm fold} = 6.9\,{\rm keV}$	Suchy et al. (2007) *RXTE*

asymmetric line shapes could introduce a systematic uncertainty in the line energy when modeling observed data with Gaussian or Lorentzian shapes. Also, the lines seem to be very prominent even for low values of the continuum optical depth.

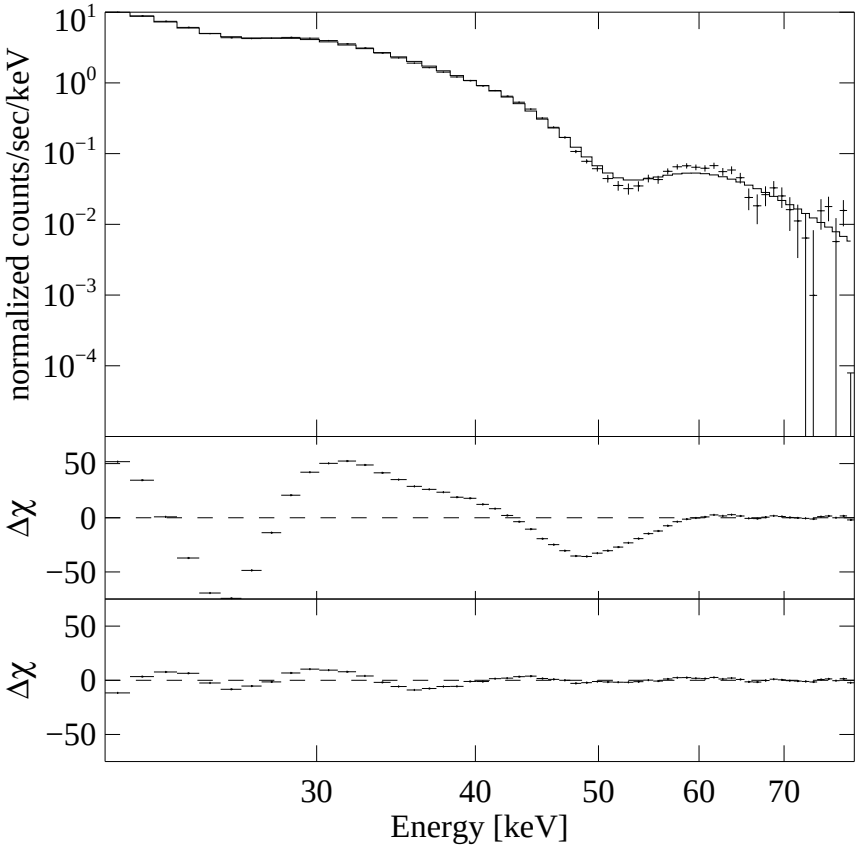

Figure 6.8: *HEXTE* simulations. Upper panel: A simulated spectrum of npex continuum shape (2.17), folded with the simulated Green's functions (slab 1-1 geometry, $B_{12} = 3.0$, $kT_{\rm e} = 5.5\,$keV, $\tau_{\rm T} = 5 \cdot 10^{-4}$, $\cos\theta = 0.5$, $z = 0.3$, $\alpha_1 = 1.5$, $\alpha_2 = 1.5$, $E_{\rm fold} = 6.16\,$keV, $A = 4.6 \cdot 10^{-3}$, $f = 1.17$) is fitted with a npex continuum, multiplied with two Gaussians (gauabs). Upper panel: data and fitted model. Middle panel: residuals for the simulated spectrum fitted with a npex continuum. Bottom panel: residuals for the continuum and lines fit shown in the upper panel. The strong emission wings of the fundamental line in the simulated spectrum are clearly observable in the residuals.

6.5 cyclomc – an XSPEC model for fitting cyclotron lines

A convolution and interpolation model for fitting CRSFs on the basis of the Monte Carlo simulation results has been developed and was implemented as a local model

for the spectral analysis fitting software package *XSPEC* (Arnaud, 1996). This choice of implementation facilitates the applicability of the model for the general observer. Other user-supplied models, based on theoretical studies, have been accepted very well in the past by the scientific community[3]. The technical details of the implementation of this model, called `cyclomc`, are described in appendix A. This model allows for the first time a physical approach to the analysis of cyclotron resonance scattering features. Not only the magnetic field strength and the temperature, but also the optical depth and the ratios of line positions, line widths and line depths are determined by the underlying physical picture. The quality of the fit hence permits conclusions on the accuracy of this picture. As shown in Sect. 5.3, the line ratios could be a sensible indicator for instance for magnetic field variations along the path of photon propagation. The model is obviously restricted to the physical assumptions and the parameter input chosen for the Monte Carlo simulations. During fitting, it interpolates the results on the assumed input parameter grid which has been described in Sect. 4.4. It also requires the independent choice of a continuum spectrum to be folded. Lacking theoretical model applications for X-ray pulsar continua, phenomenological models supplied by the *XSPEC* software are used at present (compare chapter 1). Since `cyclomc` is a convolution model, self-consistent line shapes are obtained for any given continuum. In this section, the model development from first stages to the current status of `cyclomc` is described. Spectral fits of `cyclomc` to a first sample of source data from different instruments is shown, and the model results are analyzed.

6.5.1 The first candidate – 'a long way down': V0332+53

For the example of one data set, obtained from phase-averaged spectroscopy of *INTEGRAL IBIS* data (I. Kreykenbohm, priv. com.) during a 2005 observation of V0332+53, the single steps in the process of the model design are followed-up chronologically. V0332+53 is one of the few cyclotron line sources where more than one cyclotron line is detected at a high significance, which renders it a well-suited candidate for testing both the modeling of the complex fundamental line and the simultaneous modeling of several lines. Figure 6.9 shows early-stage attempts to fit this data set with the first attempts to *XSPEC* implementations of the simulation results (Schönherr et al., 2005, 2007a). At that point, only low temperatures within the range of 2.5 to 3.5 keV had been simulated, and the geometrical constraints only included internally illuminated plasmas (cylinder and slab 1-1). Apart from this, there is another important difference between the upper and lower plot: the type of *XSPEC* model

[3] examples, among others, being the `eqpair` thermal and non-thermal continuum model for X-ray binaries (Coppi, 2000), the relativistic accretion disk line models `diskline` (Fabian et al., 1989, non-rotating BHs) and `laor` (Laor, 1991, rotating BHs), and the `tbabs` model for X-ray absorption by the interstellar medium (Wilms, Allen & McCray, 2000).

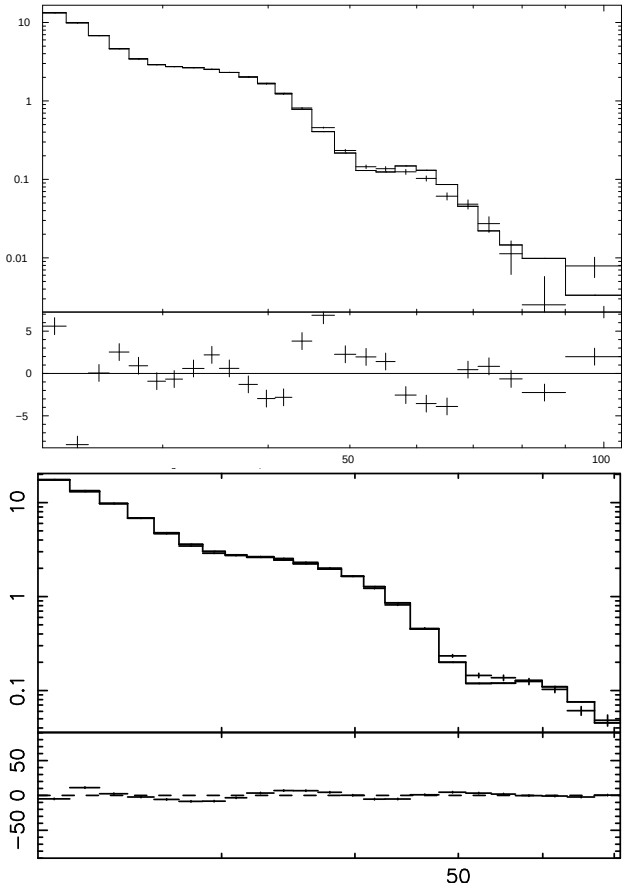

Figure 6.9: Early-stage fits of a user-built *XSPEC* table model (top) and a local analytic model (bottom) to the line features of a phase-averaged spectrum of V0332+53 from *INTEGRAL IBIS* observations. Between slab 1-1 and cylinder geometry the best fit was obtained for cylinder geometry. The data and fitted model (large panels) along with the $\Delta\chi$ residuals (top) or the model-to-data ratio (bottom) are shown (Schönherr et al., 2005, 2007a).

used. The first attempt to implement the model was done in form of a table model. As outlined in appendix A, the usage of a table model does not account rightly for the dependence of the line features on the continuum, and invokes artificial broadening of the lines during the interpolation of the tabulated spectra. This issue initially triggered the major revision of the simulation approach to calculate Green's functions instead

of full spectra, in order to develop a self-consistent, local *XSPEC* model function of formally analytic type in a second step (see appendix A). The artificial line broadening from the table model fits, however, was rather convenient for the fit quality: the observed lines were broader than the ones which could be modeled in the scope of the simulated spectra, indicating the need of higher temperatures: V0332+53 (and nearly all other cyclotron line sources) is expected to require temperatures of the order of $\sim E_{\rm cyc}/4 \gtrsim 6$ keV. Consequently, the second attempt to fit the same data set, which was performed with an early-stage implementation of the local model `cyclomc`, formally yielded a considerably worse fit quality than the one obtained with the table model approach before. The discrepancy between the modeled temperatures and the expected ones was tried to take account of by the inclusion of a `gsmooth` component of 3 keV to effectively broaden the lines. Still, the reduced $\chi^2_{\rm red} = 24$ was absolutely unacceptable. A 'long way down' began, involving numerous trial-and-error processes in the model design and testing. As expected, an important step to progress was the relaxation of the initial restriction to low temperatures after a major bug removal in the Monte Carlo code. More realistic temperatures of up to 20 keV have been simulated since then. The time-consuming simulations were run in parallel to further enlarge the parameter space also with respect to the magnetic field strength. Also, the initial restriction to include only B, $T_{\rm e}$ and μ as variable parameters was extended to an interpolation scheme including also the optical depth $\tau_{\rm T}$. Incremental refinement of the basic interpolation and convolution routine was realized. The analysis of the observability of emission wings triggered the implementation of the bottom-illuminated slab geometry, which also turned out to be an important step for the model improvement.

With the current status of the model reasonable fits of the same data set are achieved, which can be used to assess the physical parameters. Fig. 6.10 shows fits of the first two CRSFs in the *INTEGRAL* data of V0332+53. The data is modeled with a power law with a high-energy cutoff (eq. 2.16, `highecut`), folded with the CRSF Green's functions (`cyclomc`) for all geometries, and assuming 5% systematics for the *IBIS* data. All geometries yielded a similar fit quality and similar $\Delta\chi^2$ residuals; the best fit was obtained for cylinder geometry, yielding a $\chi^2_{\rm red} = 4.1$. Although some residual features remain for all geometries, those fits serve as a proof of concept that CRSFs of X-ray pulsars can be assessed for the first time with a physical model. The obtained parameters are shown for all geometries in Fig. 6.12 (black symbols). Analysis of the fit parameters and the residuals allows for conclusions on the physics of line formation beyond the simplified simulation setup which was taken in this first attempt to model CRSFs.

As mentioned above (section 6.4), the largest discrepancy between numerically predicted and observational line features seems to be the line depth. To assess this issue, a scenario or partial covering was investigated. Partial coverage of radation

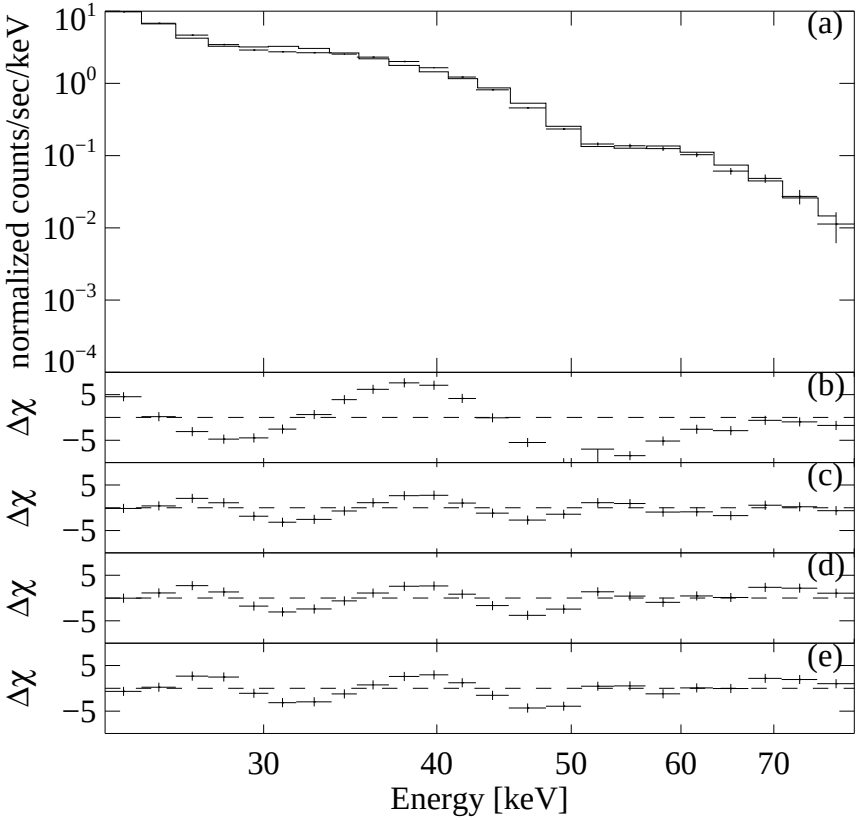

Figure 6.10: Fit of the Green's functions CRSF model `cyclomc` for all geometries to the line features of a phase-averaged spectrum of V0332+53 obtained from *INTEGRAL IBIS* observations. (a) The data and fitted model along with (b) the $\Delta\chi$ residuals for a continuum fit, and the residuals for continuum and line fits assuming (c) cylinder, (d) slab 1-1, and (e) slab 1-0 geometry are shown. The continuum shape is taken as a power law with a high-energy rolloff (2.16). The best fit was obtained for cylinder geometry ($\chi^2_{\rm red} = 4.1$).

means that part of the incident radiation from a source is 'covered' into the direction of the observer (e.g., by absorption in an intermediate layer of matter). In the present context of cyclotron line formation, only part of the continuum seed photons are as-

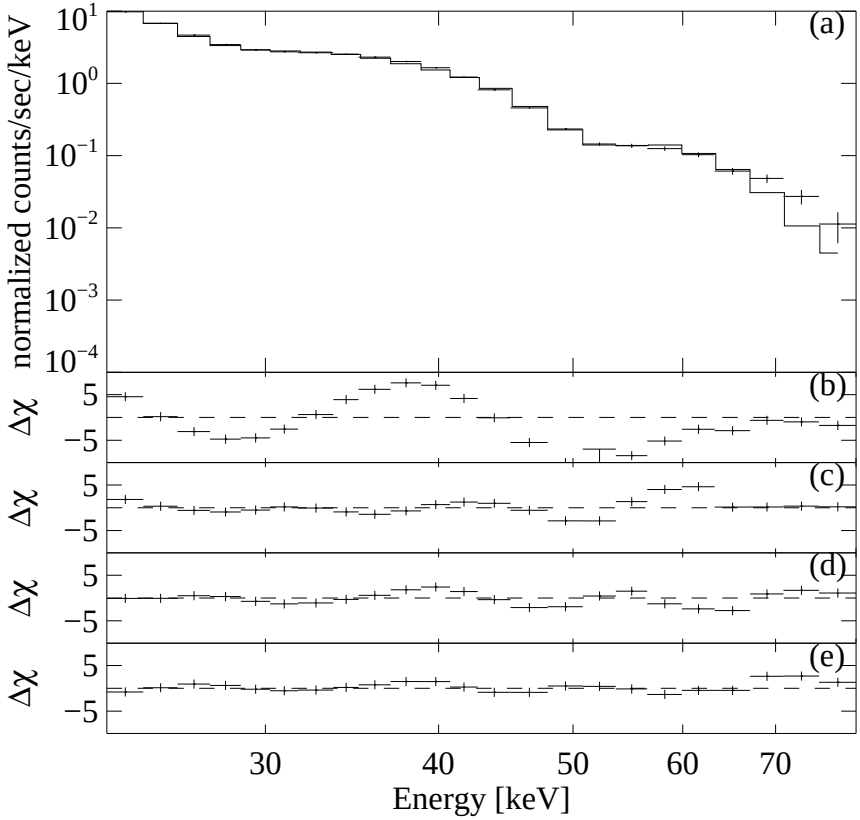

Figure 6.11: Same as Fig. 6.10 but including a scenario of partial covering. The best fit was obtained for slab 1-0 geometry ($\chi^2_{\rm red} = 1.9$).

sumed to pass the line-forming region and to be reprocessed by scattering events. This assumption effectively reduces the observed line depths. Repeating the fits with this new model approach ($A_1 \cdot$ `cyclomc` $\cdot$ `highecut` $+ A_2 \cdot$ `highecut`), the fit quality was significantly improved; the best fit was obtained for slab 1-0 geometry, yielding a $\chi^2_{\rm red} = 1.9$. The results of the fit including the partial covering scenario are shown in Fig. 6.11. The parameters obtained for slab 1-1 and slab 1-0 geometry are rather similar, while the cylinder geometry yields comparably smaller angles, lower

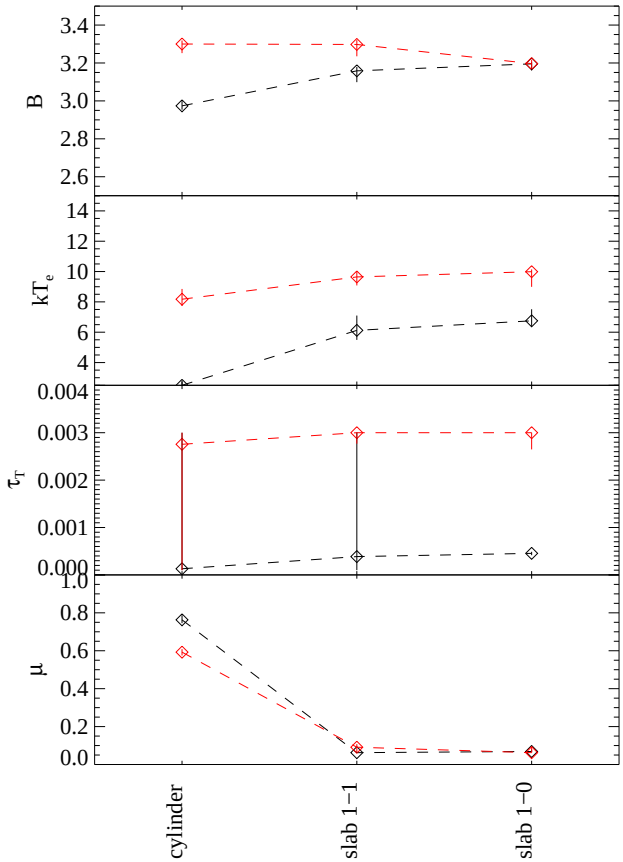

Figure 6.12: Fit parameters from modeling two CRSFs in V0332+53 data, corresponding to the residuals shown in Figs. 6.10 and 6.11, with (red symbols and error bars) and without (black symbols and error bars) the consideration of partial covering. The optical depth, τ_T is least constrained because of the discrepancy in the simulated and observed line depths. The dashed lines are included to guide the eye.

temperatures and lower magnetic field strengths. It was shown in chapter 5 that the variation of the line shapes with the angle is different for slab and cylinder geome-

Table 6.3: Best fit parameters for V0332+53. Data and model are shown in Fig. 6.11. Uncertainties are at the 90% confidence level for one interesting parameter; $\chi^2 = 27.57$ for 14 d.o.f.

name [unit]	fit value
B_{12} $[B/(10^{12}\,G)]$	$3.19^{+0.02}_{-0.03}$
$kT_{\rm e}$ [keV]	$9.99^{+0.15}_{-1.0}$
$\tau_{\rm T}$ $[10^{-3}]$	$3.0^{+0}_{-0.4}$
$\cos\theta$	$0.06^{+0.03}_{-0}$
z	0.3 frozen
α	$1.00^{+0.04}_{-0.09}$
$E_{\rm cut}$ [keV]	$14.4^{+7.0}_{-7.7}$
$E_{\rm fold}$ [keV]	$8.1^{+0.2}_{-0.08}$
A_1	$1.7^{0.2}_{-0.09}$
A_2	$1.4^{+0.08}_{-0.09}$

tries and that both small angles and high temperatures can broaden the lines. The best-fit parameters are given in table 6.3. A magnetic field strength of $3.19 \cdot 10^{12}$ G was obtained. The fundamental cyclotron line energy $E_{\rm cyc}$ was calculated from equation (3.2) as 27.45 keV, the second line position at $E_2 = 53.22$ keV, in agreement with reported results. The obtained temperature, $kT_{\rm e} = 9.99$ keV exceeds the value of $E_{\rm cyc}/4. = 6.86$ keV by a few keV. Fit parameters of `cyclomc` for all geometries with and without including the partial covering scenario are shown in Fig. 6.12. While the magnetic field and the average viewing angle stay rather stable for fits with and without partial covering, the temperature and the optical depth jump to higher values, with $\tau_{\rm T}$ even pegging at its lower and upper boundaries. Both the values for the plasma temperature (~ 10 keV) and for the optical depth ($\gtrsim 10^{-3}$) seem more realistic for the fits including partial covering (Fig. 6.11) than the values obtained from the fits without reducing the line depths (Fig. 6.10). Also the fact that the best fit was obtained for slab 1-0 geometry is conform with physical expectations, as it is the geometry with the least emission wings among the modeled ones, and as it was shown before that strong emission wings cannot be present in real source data.

6.5.2 *Going further – Do we observe a correlation of the temperature and the cyclotron resonance energy?*

Having achieved a model scenario to fit observational data for one source, the natural question to address next is its general applicability to more sources and the further interpretation of the obtained physical parameters. Having discussed different geometrical settings, and the issue of line depths previously, this section now focuses on

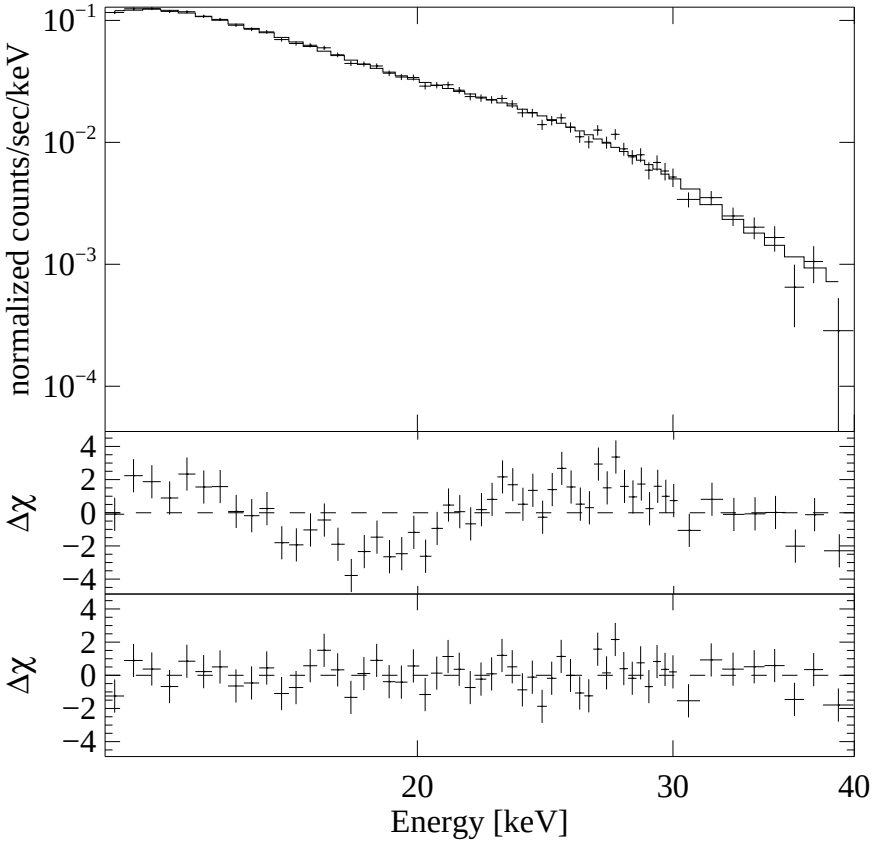

Figure 6.13: Fit of the Green's functions CRSF model `cyclomc` for slab 1-0 geometry and partial covering to the line features of a phase-averaged spectrum of 4U 1907+09 obtained from *Suzaku* observations. The data and fitted model (upper panel) along with $\Delta\chi$ residuals are shown. The residuals are depicted for the continuum fit (middle panel) and the continuum and line fit (bottom panel). The continuum shape is taken as a power law with a Fermi-Dirac cutoff (eq. 2.15, `fdcut`). For the best fit parameters ($\chi^2_{\rm red} = 0.97$), see Table 6.4.

.

modeling the fundamental line. In particular, a correlation of its width and its position in terms of the temperature versus the cyclotron resonance energy is assessed.

Two more test sources, Cen X-3 and 4U 1907+09, have been fitted with `cyclomc`.

To exclude instrumental bias, the data sample was chosen from two different instruments, *RXTE* and *Suzaku*, to complement the *INTEGRAL* results for V0332+53. Results are shown for *RXTE* data of Cen X-3 and *Suzaku* data of 4U 1907+09. Both sources are fit very well with the slab 1-0 and partial covering model setting which gave the best-fit of the V0332+53 data.

Fig. 6.13 shows spectral data (K. Pottschmidt, priv. com) and the best fits to the phase-averaged *Suzaku* spectrum of 4U 1907+09, using a power law with a Fermi-Dirac cutoff (Eq. 2.15) as the continuum component. The best fit, yielding a $\chi^2_{\rm red} = 0.97$, gave a resonance energy calculated at $E_{\rm cyc} = 18.7$ keV from Eq. (3.2) and would predict a second harmonic at 38.6 keV. The temperature $kT_e = 4.91$ keV is very similar to $E_{\rm cyc}/4. = 4.83$ keV. The best fit parameters are given in table 6.4. A surface magnetic field of $2.13 \cdot 10^{12}$ G was obtained for 4U 1907+09 under the assumption of a redshift $z = 0.3$.

Fig. 6.14 shows spectral data (S. Suchy, priv. com.) and the best fit ($\chi^2_{\rm red} = 1.4$) from an *RXTE* observation of Cen X-3. A magnetic field strength of $B = 3.45 \cdot 10^{12}$ G was obtained from the `cyclomc` parameters. The energy of the resonance features was calculated as a function of B and μ as $E_{\rm cyc} = 29.94$ keV. The modeled temperature, $kT_{\rm e} = 6.97$ keV is relatively similar to $E_{\rm cyc}/4 = 7.5$ keV.

All results for $E_{\rm cyc}$ versus $kT_{\rm e}$ from the best fits of V0332+53, 4U 1907+09 and Cen X-3 are illustrated in Fig. 6.15. They strengthen the suggestion of a correlation of the form $kT_{\rm e} = E_{\rm cyc}/4$ (see chapter 4). Observationally, a line to width correlation of the cyclotron lines was proposed (see section 3.3 and Coburn et al., 2002). Therefore it is interesting to note that the temperature versus resonance cyclotron energy correlation is obtained in spite of different best-fit viewing angles, which also influence the line width, apart from Doppler-broadening due to the temperature.

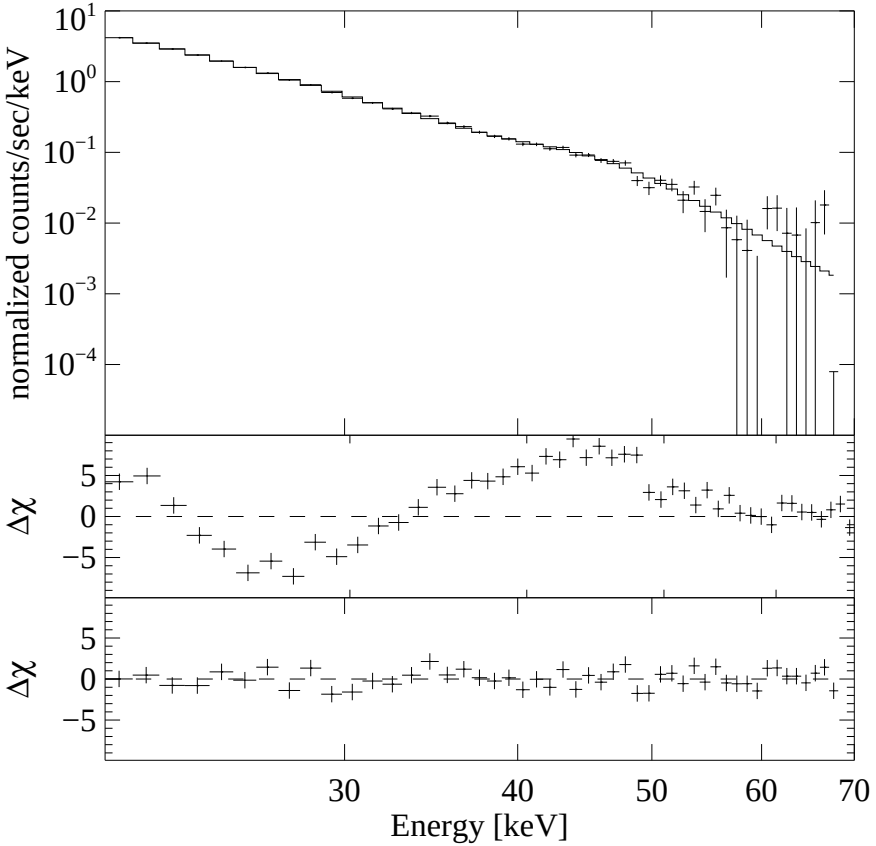

Figure 6.14: Fit of the Green's functions CRSF model `cyclomc` for slab 1-0 geometry and partial covering to the line features of a phase-averaged spectrum of Cen X-3 obtained from *RXTE HEXTE* observations. The data and fitted model (upper panel) along with $\Delta\chi$ residuals are shown. The residuals are depicted for the continuum fit (middle panel) and the continuum and line fit (bottom panel). The continuum shape is taken as a power law with a Fermi-Dirac cutoff (eq. 2.15, `fdcut`). For the best fit parameters ($\chi^2_{\rm red} = 1.4$), see Table 6.5.

Table 6.4: Best fit parameters for 4U 1907+09. Data and model are shown in Fig. 6.13. Uncertainties are at the 90% confidence level for one interesting parameter; $\chi^2 = 44.55$ for 56 d.o.f.

name [unit]	fit value
B_{12} $[B/(10^{12}\,G)]$	$2.13^{+0.2}_{-0.13}$
$kT_{\rm e}$ [keV]	$4.91^{+1.31}_{-0.54}$
$\tau_{\rm T}$ $[10^{-3}]$	$3.0^{+0}_{-3.}$
$\cos\theta$	$0.56^{+0.16}_{-0.06}$
z	0.3 frozen
α	$1.82^{+0.07}_{-0.10}$
$E_{\rm cut}$ [keV]	$10.08^{+3.5}_{-3.3}$
$E_{\rm fold}$ [keV]	$13.74^{+0.78}_{-0.72}$
A_1	$0.06^{0.009}_{-0.008}$
A_2	$0.19^{0.23}_{-0.007}$

Table 6.5: Best fit parameters for Cen X-3. Data and model shown in Fig. 6.14. Uncertainties are at the 90% confidence level for one interesting parameter; $\chi^2 = 54.7$ for 40 d.o.f.

name [unit]	fit value
B_{12} $[B/(10^{12}\,G)]$	$3.45^{+0.04}_{-0.03}$
$kT_{\rm e}$ [keV]	$6.97^{+0.29}_{-0.31}$
$\tau_{\rm T}$ $[10^{-3}]$	$2.6^{+0.4}_{-0.4}$
$\cos\theta$	$0.93^{+0.007}_{-0.01}$
z	0.3 frozen
α	$1.08^{+0.05}_{-0.04}$
$E_{\rm cut}$ [keV]	$7.26^{+0.09}_{-0.08}$
$E_{\rm fold}$ [keV]	$7.14^{+0.03}_{-7.1}$
A_1	$0.38^{+0.02}_{-0.02}$
A_2	$0.93^{+0.01}_{-0.01}$

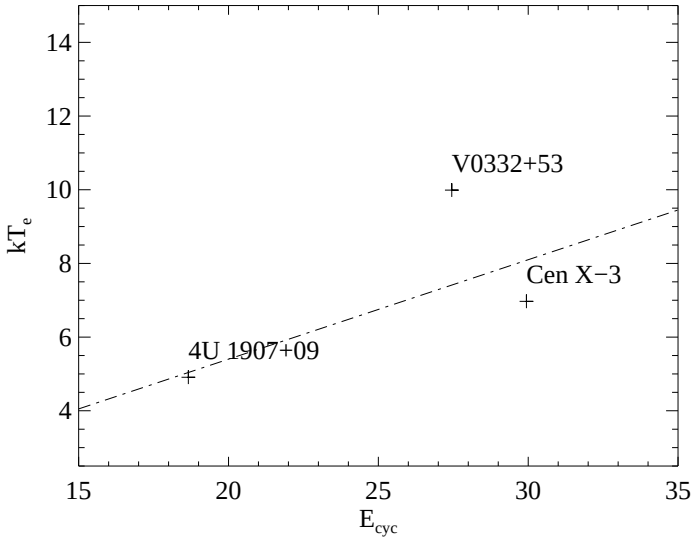

Figure 6.15: Plot of the plasma temperature, $T_{\rm e}$ versus the cyclotron resonance energy, $E_{\rm cyc}$ for the best-fit parameters obtained for V0332+53, 4U 1907+09 and Cen X-3. The relation $E_{\rm cyc} = 0.27 \cdot E_{\rm cyc}$ (Lamb, Wang & Wasserman, 1990) is plotted as a dash-dotted line.

CHAPTER 7

Summary and conclusions

Summary

An in-depth study of the formation of cyclotron resonance scattering features in the spectra of highly magnetized accreting neutron stars has been performed. Theoretical predictions were drawn from Monte Carlo simulations and the physical model assumptions were tested on real observational data. The diagnostic potential of the morphology of cyclotron lines was investigated to assess the underlying physical parameters. The influence of the magnetic field strength, the geometry of the line-forming region, the plasma temperature, the angle of radiation and the seed continuum spectral shape onto the shapes of cyclotron resonance scattering features was discussed.

Continuing the modeling progress from previous work (Araya & Harding, 1996, 1999; Araya-Góchez & Harding, 2000) several key results of those studies were confirmed. Examples are Figs. 5.1–5.3, where the optical depth progression is discussed, matching these illustrations to Figs. 4–6 from Araya & Harding (1999), or Fig. 5.5 for the study of angular redistribution similar to the illustrations used in Araya-Góchez & Harding (2000). With respect to their previous code, the revised Monte Carlo model is different in the following details: most importantly, it is not restricted to the study of hard continua. Instead, a Green's functions approach is chosen to gain independence from a priori chosen forms of incident radiation. The geometrical constraints on the line-forming region were relaxed to include the case of a bottom-illuminated slab as it has been studied by, e.g., Isenberg, Lamb & Wang (1998b) and Nishimura (2005). Moreover, the higher resolution in angle and energy binning permits to illuminate the complex form of the fundamental feature in detail. The time-consuming calculations on a huge parameter grid allow for a systematic comparison of our results to observational data.

Several results from other authors obtained with different numerical approaches were confirmed. In Fig. 5.5 (Chapter 5), the angular redistribution of the photons for

cylinder and slab geometry and for two different values of the plasma optical depth was shown. The percentage of redistributed photons per ($\cos\theta$)-bin increases with the emergent angle of radiation, θ, for cylinder and decreases with θ for slab geometry, as shown in a similar study of an internally irradiated line-forming region by Araya-Góchez & Harding (2000). For a higher optical depth and for cylinder geometry, however, the photon distribution flattens, similar to results shown by Isenberg, Lamb & Wang (1998b) for the comparable case of 1-1 slab geometry with the slab normal perpendicular to the magnetic field vector (see chapter 3). The study of the variation of the cyclotron line ratios for a non-uniform magnetic field picks up an idea from Nishimura (2005), who investigated this case for a B-field which varies linearly with height, slab geometry, and for similar optical depths. The trend of an increase of the line ratios with a decreasing magnetic field and a decrease of the line ratios with an increasing magnetic field within a line-forming region of slab 1-0 geometry (Fig. 5.11) was confirmed.

In chapter 5, theoretical predictions of the model were reported independently from observational data analysis. Except for the study of the line ratios, outlined above, all analysis assumed a uniform magnetic field in the line-forming region. A key result of this work is the study of the variation of the line parameters of the fundamental feature with the magnetic field (Fig. 5.10), the optical depth and the angle (Figs. 5.1–5.3, 5.5, and 5.6), and the temperature (Fig. 5.13). No significant variation of the fundamental line energy, $E_{\rm cyc}$, with angle is seen, and thus this simple scenario can be excluded as an explanation for observed phase dependent variations of $E_{\rm cyc}$. Omitting the emission wings, the depth of the fundamental with respect to the continuum flux is rather stable over the emergent angle, whereas the line width varies significantly with θ for cylinder and slab geometry. For both geometries the lines become wider towards higher $\cos\theta$; for slab geometry an initial decrease for $\cos\theta < 0.25$ is observed.

The variation of the line features for different magnetic field strengths and different temperatures was investigated. Obviously, the positions of the CRSFs are directly linked to the B-field strength (see Eqs. 3.1 and 3.2). However, Fig. 5.10 also shows that changes with B as to the line shapes are rather small. On the other hand, the line shapes vary strongly with increasing temperature, where more asymmetric, Doppler-broadened lines arise for higher plasma temperatures.

Furthermore, variations of the line shapes with the incident continuum shape were studied. In particular, the shape of the fundamental line changes with the continuum shape, an effect which can be understood from photon redistribution, mainly due to photon spawning in hard continua. As a result, for hard spectra for instance the emission wings are much more pronounced than for softer continua. This dependence of the CRSFs on the continuum in principle also allows for conclusions on the contin-

uum shape when modeling cyclotron resonance scattering features.

This work aims at meeting the interests of observers in analyzing cyclotron lines beyond pure theoretical predictions. A considerable part of the work was therefore dedicated to the comparison of the numerical to observational results, and to the development and design of a model applicable to real observational data. The resulting *XSPEC* implementation, named `cyclomc`, is a self-consistent model for simultaneous fits of up to four cyclotron lines.

Before actually fitting observational data, synthetic spectra were produced for a sample of sources, based on phenomenological observational results. The difficulties in the interpretation of those parameters were outlined. In particular, the question of the observability of the theoretically predicted line shapes was discussed in section 6.4. At the early stages of cyclotron line observations it was not clear whether emission features – if they were present in the data – would be observed or just smeared out by the detectors. For instance Isenberg, Lamb & Wang (1998b) and Nishimura (2005) observed that the scenario of a radiation source at the bottom of a slab as one possible geometry for the line forming region leads to less emission features in the spectra than an internally irradiated plasma. It was shown that such strong emission features as predicted by the model scenario should indeed be observable by the instruments on todays' observatories but are not seen in typical X-ray pulsar spectra. The geometry of an internally irradiated plasma is therefore concluded to be no completely valid physical assumption. Those results showed the importance of implementation of the slab 1-0 geometry for the Monte Carlo simulations, as this geometry is known to exhibit much less emission shoulders near the lines.

Testing `cyclomc` on observational data shows that CRSFs can indeed be assessed in real source data with a physical model. V0332+53 was chosen as a first candidate to test the model as it is one of the sources which exhibits several CRSFs with the fundamental one at a moderate energy of $E_{\rm cyc} \sim 27\,$keV. Fits of the first two lines as seen in *INTEGRAL* data were analyzed. This is the first time a simultaneous fit of several CRSFs with a realistic, physical model has been attempted.

Fitting the line shapes for V0332+53 data with `cyclomc`, however, pointed out a general problem of the current model approach: The depths `cyclomc` yields for rather low $\tau_{\rm T}$ are very deep compared to the observations. Fits for all three geometries could therefore be realized only for rather high $\chi^2_{\rm red} \sim 4$. Within those errors, all fits gave comparable results for the magnetic field, the temperature and the optical depth. Different average viewing angles are predicted by the slab or cylindrical geometries, which is expected from the analysis of the variation of the lines with the angle, which was performed in chapter 5. The cylinder geometry yielded the best fit of the data. However, the geometry and the physical parameters could not be constrained unambiguously without finding a way to reduce the average line depths. Magnetic field

gradients in an accretion column might greatly flatten the line shapes (O. Nishimura, private communication). Also, one could imagine a scenario of partial covering of the emergent radiation, where only part of the radiation is assumed to pass the region of line formation and is reprocessed with `cyclomc`. Applying this partial covering scenario significantly improved the fits. The best fit was found for the 1-0 slab geometry, yielding a $\chi^2_{\rm red} = 1.9$.

The analysis of observational data was extended to fitting the fundamental line for two more sources, yielding best fits with $\chi^2_{\rm red} = 1.4$ and $\chi^2_{\rm red} = 0.97$. The obtained values for the magnetic field strength of the three modeled sources, V0332+53, 4U 1907+09, and Cen X-3 are in general agreement with results from previous, phenomenological fits. It is important to stress that these values are based directly on a physical model assumption, with the only uncertainty given by the (fixed) redshift and the errors of the fit. In contrast, magnetic field strengths inferred from phenomenological modeling are calculated from the line centroids which can deviate from the physical resonance energy, $E_{\rm cyc}$. The obtained temperatures for all three sources strengthen the assumption of a correlation between the temperature and the resonance energy, $kT_{\rm e} = E_{\rm cyc}/4$. Again, the values of the temperatures are based directly on physical assumptions, opposed to indirect attempts which have been made to derive the temperature from the (phenomenologically obtained) line widths or from the cutoff characteristics of the continuum.

Outlook

Modeling cyclotron lines is a highly intriguing task, and probably a lot of work will be ongoing in this field of research in the future. While recent discussions of proton cyclotron lines in magnetars have been drawing renewed attention to this topic, the electron cyclotron lines for accreting pulsars are still mysterious enough by themselves to demand further studies.

A better understanding of CRSFs will require further generalizations of simplified model approaches like the CRSF model presented here. Angular anisotropy of the continuum photon flux should be included into the discussion, possibly in connection with the emerging theoretical results on the continuum formation (Becker & Wolff, 2007). The model approach taken could be easily generalized to arbitrary angular distributions by the calculation of our Green's functions independently not only of the continuum energy but also of the continuum angular distribution. Also, a combination of the theoretical investigations for X-ray pulsar continua and cyclotron line features would be desirable. A bulk velocity component and velocity flow gradients in the plasma might be necessary to account for the phase resolved variations of the fundamental line energy. An internally irradiated plasma seems to be a too simplified

approach; the consideration of the source photons to be injected at the bottom of the slab (1-0 geometry) or according to a probably biased distribution of incident photon production in a cylindrical plasma is possibly more realistic. Gravitational light bending should be assessed further as a possible mechanism to change the beam pattern and to broaden and smoothen the line shapes due to two-pole contributions.

However, the probably most pressing issue to be investigated further is the reported discrepancy in theoretical and observational line depths. More realistic B-field gradients could account for shallower lines. As the consideration of a scenario of partial covering, which effectively reduces the line depths, significantly improves the fit quality of `cyclomc` to data, it follows that the consideration of non-constant magnetic fields within the line-forming region could play a major role in the process of better modeling and understanding cyclotron lines. However, this matter is difficult to judge as long as no better constraints exist on the order of magnitude of the plasma density, which is found in the literature at present to vary several orders of magnitude.

Systematic data analysis on the basis of a physical model like the one presented here must be done in the future to further improve the understanding of the manifold observational results. For instance, an extended analysis of parameter correlations like the one predicted for the temperature and the resonance energy would be highly interesting. The model presented here is foreseen to be made available to the scientific community after including a revised interpolation scheme to facilitate its usage for data fitting. Modifications of the underlying physical scenario guided by systematic fits of observational data should help in further improving the comparison of the model and real data.

Bibliography

Alexander, S. G., & Mészáros, P., 1989, Astrophys. J., 344, L1

Alexander, S. G., & Mészáros, P., 1991, Astrophys. J., 372, 565

Alpar, M. A., & Shaham, J., 1985, Nature, 316, 239

Andersson, N., 1998, Astrophys. J., 502, 708

Araya, R. A., & Harding, A. K., 1996, Astrophys. J., 463, 33

Araya, R. A., & Harding, A. K., 1999, Astrophys. J., 517, 334

Araya-Góchez, R. A., & Harding, A. K., 2000, Astrophys. J., 544, 1067

Arnaud, K. A., 1995, The File Format for XSPEC Table Models, OGIP Memo OGIP/92-009

Arnaud, K. A., 1996, in Astronomical Data Analysis Software and Systems V, ed. G. H. Jacoby, J. Barnes, (San Francisco: ASP), 17

Arons, J., 1993, Astrophys. J., 408, 160

Arons, J., Klein, R. I., & Lea, S. M., 1987, Astrophys. J., 312, 666

Baade, W., & Zwicky, F., 1934, Proc. of the Nat. Acad. of Sci., 20, 254

Barnstedt, J., et al., 2007, in prep.

Basko, M. M., & Sunyaev, R. A., 1976, Mon. Not. R. Astron. Soc., 175, 395

Becker, P. A., 1998, Astrophys. J., 498, 790

Becker, P. A., & Wolff, M. T., 2005, Astrophys. J., 630, 465

Becker, P. A., & Wolff, M. T., 2007, Astrophys. J., 654, 435

Bhattacharya, D., & van den Heuvel, E. P. J., 1991, Physics Report, 203, 1

Bhattacharyya, M., Miller, C., & Lamb, F. K., 2006, Astrophys. J., 644, 1085

Bildsten, L., 1998, Astrophys. J., 501, L89

Bildsten, L., et al., 1997, Astrophys. J., 113, S367

Bildsten, L., Chang, P., & Paerels, F., 2003, Astrophys. J., 591, L29

Blandford, R. D., Applegate, J. H., & Hernquist, L., 1983, Mon. Not. R. Astron. Soc., 204, 1025

Blandford, R. D., & Romani, R. W., 1988, Mon. Not. R. Astron. Soc., 234, 57

Blondin, J. M., 1994, Astrophys. J., 435, 756

Blondin, J. M., & Mezzacappa, A., 2007, Nature, 445, 58

Blondin, J. M., & Woo, J. W., 1995, Astrophys. J., 445, 889

Blum, S., & Kraus, U., 2000, Astrophys. J., 529, 968

Bonazzola, S., Heyvaerts, J., & Puget, J. L., 1979, Astron. Astrophys., 78, 53

Boyd, P., & Still, M., 2004, Her X-1 Apparently Entering A New Anomalous Low State, ATEL 228

Boyd, P., Still, M., & Corbet, R., 2004, Her X-1 Exiting Anomalous Low State, ATEL 307

Boyd, P. T., & Smale, A. P., 2000, in Rossi2000: Astrophysics with the Rossi X-ray Timing Explorer. March 22-24, 2000 at NASA's Goddard Space Flight Center,

Greenbelt, MD USA, meeting abstract, ed. T. E. Strohmayer

Bulik, T., Mészáros, P., Woo, J. W., Hagase, F., & Makishima, K., 1992, Astrophys. J., 395, 564

Bulik, T., Riffert, H., Mészáros, P., Makishima, K., Mihara, T., & Thomas, B., 1995, Astrophys. J., 444, 405

Burderi, L., di Salvo, T., Robba, N. R., La Barbera, A., & Iaria, R., 2001, Memorie della Societa Astronomica Italiana, 72, 761

Burnard, D. J., Arons, J., & Klein, R. I., 1991, Astrophys. J., 367, 575

Burnard, D. J., Klein, R. I., & Arons, J., 1988, Astrophys. J., 324, 1001

Bussard, R. W., Alexander, S. B., & Mészáros, P., 1986, Phys. Rev. D, 34, 440

Caballero, I., et al., 2007, Astron. Astrophys., 465, L21

Canuto, V., Lodenquai, J., & Ruderman, M., 1971, Phys. Rev. D, 3, 2303

Chadwick, J., 1934, Proc. Roy. Soc., A, 136, 692

Chakrabarty, D., 2006, in AAS Meeting Abstracts, Vol. 209, (Washington: AAS)

Chandrasekhar, S., 1931, Mon. Not. R. Astron. Soc., 91, 456

Charles, P. A., & Seward, F. D., 1995, Exploring the X-ray universe, (Cambridge, New York: Cambridge University Press)

Chodil, G., Mark, H., Rodrigues, R., Seward, F., Swift, C. D., Hiltner, W. A., Wallerstein, G., & Mannery, E. J., 1967, Phys. Rev. Lett., 19, 681

Clark, G. W., Woo, J. W., Nagase, F., Makishima, K., & Sakao, T., 1990, Astrophys. J., 353, 274

Coburn, W., Heindl, W. A., Gruber, D. E., Rothschild, R. E., Staubert, R., Wilms, J., & Kreykenbohm, I., 2001, Astrophys. J., 552, 738

Coburn, W., Heindl, W. A., Rothschild, R. E., Gruber, D. E., Kreykenbohm, I., Wilms, J., Kretschmar, P., & Staubert, R., 2002, Astrophys. J., 580, 394

Coburn, W., Kretschmar, P., Kreykenbohm, I., McBride, V. A., Rothschild, R. E., & Wilms, J., 2005, Multiple Cyclotron Lines in V0332+53, ATEL 381

Contopoulos, I., & Spitkovsky, A., 2006, Astrophys. J., 643, 1139

Cook, M. C., & Page, C. G., 1987, Mon. Not. R. Astron. Soc., 225, 381

Coppi, P. S., 2000, in BAAS, Vol. 32, (Washington: AAS), 1516

Cottam, J., Paerels, F., & Mendez, M., 2002, Nature, 420, 51

Cox, N. L. J., Kaper, L., & Mokiem, M. R., 2005, Astron. Astrophys., 436, 661

Cusumano, G., di Salvo, T., Burderi, L., Orlandini, M., Piraino, S., Robba, N., & Santangelo, A., 1998, Astron. Astrophys., 338, L79

dal Fiume, D., et al., 2000, Advances in Space Research, 25, 399

Daugherty, J. K., & Harding, A. K., 1986, Astrophys. J., 309, 362

Davidson, K., & Ostriker, J. P., 1973, Astrophys. J., 179, 585

Deeter, J. E., Scott, D. M., Boynton, P. E., Miyamoto, S., Kitamoto, S., Takahama, S., & Nagase, F., 1998, Astrophys. J., 502, 802

Dennerl, K., 1991, *Ph.D. thesis*, Universität München, Garching

di Salvo, T., Santangelo, A., & Segreto, A., 2004, Nuclear Physics B Proceedings Supplements, 132, 446

Duncan, R. C., & Thompson, C., 1992, Astrophys. J., 392, L9

Einstein, A., 1911, Annalen der Physik, 340, 898

Fabian, A. C., Rees, M. J., Stella, L., & White, N. E., 1989, Mon. Not. R. Astron. Soc., 238, 729

Faucher-Giguère, C.-A., & Kaspi, V. M., 2006, Astrophys. J., 643, 332

Flowers, E., & Ruderman, M. A., 1977, Astrophys. J., 215, 302
Fock, V., 1928, Z. Phys., 47, 446
Francey, R. J., Fenton, A. G., Harries, J. R., & McCracken, K. G., 1967, Nature, 216, 773
Freeman, P. E., Lamb, D. Q., Wang, J. C. L., Wasserman, I., Loredo, T. J., Fenimore, E. E., Murakami, T., & Yoshida, A., 1999, Astrophys. J., 524, 772
Friedman, J. L., & Morsink, S. M., 1998, Astrophys. J., 502, 714
Fritz, S., Kreykenbohm, I., Wilms, J., Staubert, R., Bayazit, F., Pottschmidt, K., Rodriguez, J., & Santangelo, A., 2006, Astron. Astrophys., 458, 885
Ghosh, P., & Lamb, F. K., 1978, Astrophys. J., 223, L83
Ghosh, P., & Lamb, F. K., 1979a, Astrophys. J., 232, 259
Ghosh, P., & Lamb, F. K., 1979b, Astrophys. J., 234, 296
Giacconi, R., Gursky, H., Kellogg, E., Schreier, E., & Tananbaum, H., 1971a, Astrophys. J., 167, L67
Giacconi, R., Gursky, H., Paolini, F. R., & Rossi, B. B., 1962, Phys. Rev. Lett., 9, 439
Giacconi, R., Kellogg, E., Gorenstein, P., Gursky, H., & Tananbaum, H., 1971b, Astrophys. J., 165, L27
Gil, J. A., Melikidze, G. I., & Mitra, D., 2002, Astron. Astrophys., 388, 235
Glendenning, N. K., 1996, Compact Stars, Nuclear Physics, Particle Physics and General Relativity, XIV, (New York: Springer-Verlag)
Gnedin, Y. N., Pavlov, G. G., & Shibanov, Y. A., 1978, Sovjet. Astr. Letters, 4, 117
Gnedin, Y. N., & Sunyaev, R. A., 1974, Astron. Astrophys., 36, 379
Gold, T., 1969, Nature, 221, 25
Gonthier, P. L., Harding, A. K., Baring, M. G., Costello, R. M., & Mercer, C. L., 2000, Astrophys. J., 540, 907
Götz, D., Mereghetti, S., Hurley, K., Mirabel, I. F., Esposito, P., Tiengo, A., Weidenspointner, G., & von Kienlin, A., 2007, in Proceedings of the 6th INTEGRAL Workshop, Moscow, 2006, (Noordwijk: ESA Publications Division), in press
Götz, D., Mereghetti, S., Tiengo, A., & Esposito, P., 2006, Astron. Astrophys., 449, L31
Grove, J. E., et al., 1995, Astrophys. J., 438, L25
Gruber, D. E., Heindl, W. A., Rothschild, R. E., Coburn, W., Staubert, R., Kreykenbohm, I., & Wilms, J., 2001, Astrophys. J., 562, 499
Gunn, J. E., & Ostriker, J. P., 1969, Nature, 221, 454
Hankins, T. H., & Eilek, J. A., 2006, in AAS Meeting Abstracts, Vol. 209, (Washington: AAS), 104
Harding, A. K., & Daugherty, J. K., 1991, Astrophys. J., 374, 687
Harding, A. K., Kirk, J. G., Galloway, D. J., & Mészáros, P., 1984, Astrophys. J., 278, 369
Harding, A. K., & Lai, D., 2006, Rep. Prog. Phys, 69, 2631
Harding, A. K., & Preece, R., 1987, Astrophys. J., 319, 939
Heindl, W., Coburn, W., Kreykenbohm, I., & Wilms, J., 2003, Cyclotron Line in XTE J0658-073, ATEL 200
Heindl, W. A., & Chakrabarty, D., 1999, in "Highlights in X-ray Astronomy 1998", ed. B. Aschenbach, M. J. Freyberg, (Garching: MPE), 25
Heindl, W. A., et al., 2000, in AIP Conf. Proc. 510, Proc. 5th Compton Symp., ed. M. L. McConnell, J. M. Ryan, (New York: AIP), 1230
Heindl, W. A., Coburn, W., Gruber, D. E., Pelling, M. R., Rothschild, R. E., Wilms, J., Pottschmidt, K., & Staubert, R., 1999, Astrophys. J., 521, L49
Heindl, W. A., Coburn, W., Gruber, D. E.,

Rothschild, R. E., Kreykenbohm, I., Wilms, J., & Staubert, R., 2001, Astrophys. J., 563, L35

Heindl, W. A., Rothschild, R. E., Coburn, W., Staubert, R., Wilms, J., Kreykenbohm, I., & Kretschmar, P., 2004, in AIP Conf. Proc. 714: X-ray Timing 2003: Rossi and Beyond, ed. P. Kaaret, F. K. Lamb, J. H. Swank, (New York: AIP), 323

Hessels, J. W. T., Ransom, S. M., Stairs, I. H., Freire, P. C. C., Kaspi, V. M., & Camilo, F., 2006, Science, 311, 1901

Hewish, A., Bell, S. J., Pilkington, J. D., Scott, P. F., & Collins, R. A., 1968, Nature, 217, 709

Houck, J. C., & Denicola, L. A., 2000, in Astronomical Data Analysis Software and Systems IX, ed. N. Manset, C. Veillet, D. Crabtree, (San Francisco: ASP), 591

Hulse, R., & Taylor, J., 1975, Astrophys. J., 195, L51

Hutchings, J. B., Cowley, A. P., Crampton, D., van Paradus, J., & White, N. E., 1979, Astrophys. J., 229, 1079

Ibrahim, A. I., adn Jean H. Swank, S. S.-H., Parke, W., Zane, S., & Turolla, R., 2002, Astrophys. J., 574, L51

Inoue, H., et al., 2005, Suzaku detection of cyclotron line near 50 keV for A0535+26, ATEL 613

in't Zand, J., et al., 1998, Astrophys. J., 496, 386

Isenberg, M., Lamb, D. Q., & Wang, J. C. L., 1998a, Astrophys. J., 493, 154

Isenberg, M., Lamb, D. Q., & Wang, J. C. L., 1998b, Astrophys. J., 505, 688

Johnson, M. H., & Lippmann, B. A., 1949, Phys. Rev., 76, 828

Jones, P. B., 2004, Phys. Rev. Lett., 93, 221101

Kaaret, P., et al., 2007, Astrophys. J., 657, L97

Kendziorra, E., et al., 1994, Astron. Astrophys., 291, 31

Kendziorra, E., et al., 1992, in The Compton Observatory Science Workshop, ed. C. R. Shrader, N. Gehrels, B. Dennis, (Washington: NASA), 217

Kennard, E., 1927, Z. Phys., 44, 326

Klochkov, D., Shakura, N., Postnov, K., Staubert, R., & Wilms, J., 2006, A precessing warped accretion disk around the X-ray pulsar Her X-1, astro-ph/0612790

Kontar, E. P., MacKinnon, A. L., Schwartz, R. A., & Brown, J. C., 2006, Astron. Astrophys., 446, 1157

Kopal, Z., 1989, The Roche problem and its significance for double-star astronomy, Astrophysics and Space Science Library 152, (Dordrecht and Boston: Kluwer Academic Publishers)

Kouveliotou, C., et al., 1998, Nature, 393, 235

Kouveliotou, C., et al., 1999, Astrophys. J., 510, L115

Kraus, U., 1998, Light deflection near neutron stars, (Braunschweig and Wiesbaden: Vieweg), 66

Kraus, U., Blum, S., Schulte, J., Ruder, H., & Mészáros, P., 1996, Astrophys. J., 467, 794

Kraus, U., Nollert, H.-P., Ruder, H., & Riffert, H., 1995, Astrophys. J., 450, 763

Kraus, U., Zahn, C., Weth, C., & Ruder, H., 2003, Astrophys. J., 590, 424

Kretschmar, P., 1996, *Ph.D. thesis*, University of Tübingen

Kretschmar, P., et al., 2005, Integral observes possible cyclotron line at 47 keV for 1A 0535+262, ATEL 601

Kretschmar, P., et al., 1997, in The Transparent Universe, ed. C. Winkler, T. J.-L. Courvoisier, P. Durouchoux, (Noordwijk: ESA Publications Division), 141

Kretschmar, P., et al., 1997, Astron. Astrophys., 325, 623

Kreykenbohm, I., 2004, *Ph.D. thesis*, University of Tübingen

Kreykenbohm, I., Coburn, W., Wilms, J.,

Kretschmar, P., Staubert, R., Heindl, W. A., & Rothschild, R. E., 2002, Astron. Astrophys., 395, 129

Kreykenbohm, I., Kretschmar, P., Wilms, J., Staubert, R., Kendziorra, E., Gruber, D. E., Heindl, W. A., & Rothschild, R. E., 1999, Astron. Astrophys., 341, 141

Kreykenbohm, I., et al., 2005, Astron. Astrophys., 433, 45

Kreykenbohm, I., Staubert, R., von Kienlin, A., Martinez-Nunez, S., Mas-Hesse, M., Sanchez, C., Palumbo, G. G. C., & Sunyaev, R. A., 2006, Vela X-1 in a highly active state, ATEL 711

Krivonos, R., Produit, N., Kreykenbohm, I., Staubert, R., von Kienlin, A., Winkler, C., & Gehrels, N., 2003, A very intense X-ray outburst of Vela X-1 detected with INTEGRAL, ATEL 211

Krzeminski, W., 1974, Astrophys. J., 192, L135

Kuster, M., Wilms, J., Staubert, R., Risse, P., Heindl, W. A., Rothschild, R., Shakura, N. I., & Postnov, K. A., 2002, A Her X-1 Turn-On: Using the pulse profile to probe the outer edge of an accretion disk, astro-ph/0203213

La Barbera, A., Santangelo, A., Orlandini, M., & Segreto, A., 2003, Astron. Astrophys., 400, 993

La Barbera, A., Segreto, A., Santangelo, A., Kreykenbohm, I., & Orlandini, M., 2005, Astron. Astrophys., 438, 617

Lamb, D. Q., Wang, J. C. L., & Wasserman, I. M., 1990, Astrophys. J., 363, 670

Lamb, F., & Yu, W., 2005, in Binary Radio Pulsars, ed. F. A. Rasio, I. H. Stairs, (San Francisco: ASP), 299

Lamb, F. K., & Miller, M. C., 2001, Astrophys. J., 554, 1210

Lamb, F. K., Pethick, C. J., & Pines, D., 1973, Astrophys. J., 184, 271

Lamb, F. K., Shibazaki, N., Alpar, M. A., & Shaham, J., 1985, Nature, 317, 681

Landau, L., 1930, Z. Physik, 64, 629

Landau, L., 1932, Phys. Z. Sowjetunion, 1, 285

Landau, L., 1979, Lehrbuch der theoretischen Physik III, 3. Auflage, (Berlin: Akademie-Verlag)

Laor, A., 1991, Astrophys. J., 376, 90

Laplace, P. S., 1796, De l'Imprimerie du Circle Social, Paris, An IV, 2, 305

Latal, H. G., 1986, Astrophys. J., 309, 372

Leahy, D. A., 1991, Mon. Not. R. Astron. Soc., 251, 203

Levin, Y., & Ushomirsky, G., 2001, Mon. Not. R. Astron. Soc., 324, 917

Levine, A., Rappaport, S., Putney, A., Corbet, R., & Nagase, F., 1991, Astrophys. J., 381, 101

Levine, A. M., & Jernigan, J. G., 1982, Astrophys. J., 262, 294

Lewin, W. H. G., & van der Klis, M., (eds.) 2006, Compact stellar X-ray sources, Cambridge Astrophysics Series 39, (Cambridge, UK: Cambridge University Press)

Lewin, W. H. G., van Paradijs, J., & Taam, R. E., 1993, Space Science Reviews, 62, 223

Lewin, W. H. G., van Paradijs, J., & van den Heuvel, E. P. J., (eds.) 1995, X-ray binaries, Cambridge Astrophysics Series, (Cambridge, MA: Cambridge University Press)

Lipunov, V. M., 1992, Astrophysics of Neutron Stars, (Berlin Heidelberg: Springer)

Liu, Q. Z., van Paradijs, J., & van den Heuvel, E. P. J., 2005, Astron. Astrophys., 442, 1135

Longair, M. S., 1981, High Energy Astrophysics, (Cambridge: Cambridge University Press)

Lorimer, D. R., 2005, Living Reviews in Relativity, 8

Lorimer, D. R., & Kramer, M., 2004,

Handbook of Pulsar Astronomy, Cambridge observing handbooks for research astronomers 4, (Cambridge, UK: Cambridge University Press)
Maisack, M., Grove, J. E., Kendziorra, E., Kretschmar, P., Staubert, R., & Strickman, M. S., 1997, Astron. Astrophys., 325, 212
Makishima, K., Kawai, N., Koyama, K., Shibazaki, N., Nagase, F., & Nakagawa, M., 1984, Publ. Astron. Soc. Jpn., 36, 679
Makishima, K., & Mihara, T., 1992, in Proc. 28th Yamada Conf., ed. Y. Tanaka, K. Koyama, (Tokyo: Univ. Acad. Press), 23
Makishima, K., et al., 1990a, Astrophys. J., 365, L59
Makishima, K., Mihara, T., Nagase, F., & Tanaka, Y., 1999, Astrophys. J., 525, 978
Makishima, K., et al., 1990b, Publ. Astron. Soc. Jpn., 42, 295
Mazets, E. P., Golenetskii, S. V., Aptekar, R. L., Gurian, I. A., & Ilinskii, V. N., 1981, Nature, 290, 378
Mereghetti, S., 2001, in X-ray Astronomy: Stellar Endpoints, AGN, and the Diffuse X-ray Background, ed. N. E. White, G. Malaguti, G. G. C. Palumbo, Vol. 599, (New York: AIP), 219
Mereghetti, S., Götz, D., Mirabel, I. F., & Hurley, K., 2005, Astron. Astrophys., 433, L9
Mereghetti, S., & Stella, L., 1995, Astrophys. J., 442, L17
Mészáros, P., 1978, Astron. Astrophys., 63, L19
Mészáros, P., 1984, Space Science Reviews, 38, 325
Mészáros, P., 1992, High-Energy Radiation from Magnetized Neutron Stars, (Chicago: University of Chicago Press)
Mészáros, P., Harding, A. K., Kirk, J. G., & Galloway, D. J., 1983, Astrophys. J., 266, L33
Mészáros, P., & Nagel, W., 1985a, Astrophys. J., 298, 147
Mészáros, P., & Nagel, W., 1985b, Astrophys. J., 299, 138
Mészáros, P., & Riffert, H., 1988, Astrophys. J., 327, 712
Michell, J., 1784, Philosophical Transactions of the Royal Society of London LXXIV, part 1, 35
Mihara, T., 1995, *Ph.D. thesis*, RIKEN, Tokyo
Mihara, T., Makishima, K., Kamijo, S., Ohashi, T., Nagase, F., Tanaka, Y., & Koyama, K., 1991, Astrophys. J., 379, L61
Mihara, T., Makishima, K., & Nagase, F., 1995, in BAAS, Vol. 27, (Washington: AAS), 1434
Mihara, T., Makishima, K., & Nagase, F., 1998, Advances in Space Research, 22, 987
Mihara, T., Makishima, K., Ohashi, T., Sakao, T., & Tashiro, M., 1990, Nature, 346, 250
Minkowski, R., 1941, Publ. Astron. Soc. Pac., 53, 224
Mowlavi, N., et al., 2006, Astron. Astrophys., 451, 187
Nagase, F., 1989, Publ. Astron. Soc. Jpn., 41, 1
Nagase, F., Corbet, R. H. D., Day, C. S. R., Inoue, H., Takeshima, T., Yoshida, K., & Mihara, T., 1992, Astrophys. J., 396, 147
Nagase, F., et al., 1991, Astrophys. J., 375, L49
Nagase, F., Hayakawa, S., Sato, N., Masai, K., & Inoue, H., 1986, Publ. Astron. Soc. Jpn., 38, 547
Nagel, W., 1980, Astrophys. J., 236, 904
Nagel, W., 1981a, Astrophys. J., 251, 278
Nagel, W., 1981b, Astrophys. J., 251, 288
Nakajima, M., Mihara, T., Makishima, K., & Niko, H., 2006, Astrophys. J., 646, 1125
Newton, S. I., 1704, Opticks, (New York: Dover)
Nishimura, O., 2003, Publ. Astron. Soc. Jpn., 55, 849
Nishimura, O., 2005, Publ. Astron. Soc. Jpn.,

57, 769
Ohashi, T., et al., 1984, Publ. Astron. Soc. Jpn., 36, 699
Oppenheimer, J., & Volkoff, G., 1939, Phys. Rev., 55, 374
Orlandini, M., et al., 1998a, Astron. Astrophys., 332, 121
Orlandini, M., et al., 1998b, Astrophys. J., 500, L163
Ostriker, J. P., & Davidson, K., 1973, in IAU Symp., ed. H. Bradt, R. Giacconi, 143
Ostriker, J. P., & Gunn, J. E., 1969, Astrophys. J., 157, 1395
Pacini, F., 1967, Nature, 216, 567
Page, D., 1998, in The Many Faces of Neutron Stars., ed. R. Buccheri, J. van Paradijs, A. Alpar, 539
Pethick, C. J., 1992, Reviews of Modern Physics, 64, 1133
Plesset, M., 1930, Phys. Rev., 36, 1728
Potekhin, A. Y., & Lai, D., 2007, Mon. Not. R. Astron. Soc., 376, 793
Pottschmidt, K., et al., 2005, Astrophys. J., 634, L97
Pravdo, S. H., & Bussard, R. W., 1981, Astrophys. J., 246, L115
Pringle, J. E., & Rees, M. J., 1972, Astron. Astrophys., 21, 1
Rabi, I., 1928, Z. Phys., 49, 507
Reisenegger, A., 2003, in Proc. International Workshop on Strong Magnetic Fields and Neutron Stars
Reisenegger, A., Prieto, J. P., Benguria, R., Lai, D., & Araya, P. A., 2005, in Magnetic Fields in the Universe: From Laboratory and Stars to Primordial Structures., ed. E. M. de Gouveia dal Pino, G. Lugones, A. Lazarian, (San Francisco: AIP), 263
Riffert, H., & Mészáros, P., 1988, Astrophys. J., 325, 207
Riffert, H., Nollert, H.-P., Kraus, U., & Ruder, H., 1993, Astrophys. J., 406, 185
Rosenberg, F. D., Eyles, C. J., Skinner, G. K., & Willmore, A. P., 1975, Nature, 256, 628
Rothschild, R. E., et al., 2006, Astrophys. J., 641, 801
Ruderman, M., 1972, Annual Review of Astronomy and Astrophysics, 10, 427
Santangelo, A., del Sordo, S., Segreto, A., dal Fiume, D., Orlandini, M., & Piraino, S., 1998, Astron. Astrophys., 340, L55
Santangelo, A., Segreto, A., Del Sordo, S., Mauro, O., Parmar, A. N., & Dal Fiume, D., 2000, in BAAS, Vol. 32, (Washington: AAS), 1230
Santangelo, A., et al., 1999, Astrophys. J., 523, L85
Schanne, S., Gotz, D., Gerard, L., Sizun, P., Falanga, M., Hamadache, C., Cordier, B., & von Kienlin, A., 2007, in Proceedings of the 6th INTEGRAL Workshop, Moscow, 2006, (Noordwijk: ESA Publications Division), in press
Schönherr, G., Wilms, J., Kretschmar, P., Kreykenbohm, I., Coburn, W., Rothschild, R., & Santangelo, A., 2005, in Proceedings of "The X-ray Universe 2005", San Lorenzo de El Escorial, 2005, (Noordwijk: ESA Publications Division)
Schönherr, G., Wilms, J., Kretschmar, P., Kreykenbohm, I., Coburn, W., Rothschild, R., & Santangelo, A., 2007a, in Proceedings of the 6th INTEGRAL Workshop, Moscow, 2006, (Noordwijk: ESA Publications Division), in press
Schönherr, G., Wilms, J., Kretschmar, P., Kreykenbohm, I., Rothschild, R., Santangelo, A., Staubert, R., & Coburn, W., 2007b, Astron. Astrophys., submitted
Schreier, E., Levinson, R., Gursky, H., Kellogg, E., Tananbaum, H., & Giacconi, R., 1972, Astrophys. J., 172, L79
Shakura, N. I., Postnov, K. A., & Prokhorov, M. E., 1991, Pis ma Astronomicheskii Zhurnal, 17, 803
Shakura, N. I., Prokhorov, M. E., Postnov,

K. A., & Ketsaris, N. A., 1999, Astron. Astrophys., 348, 917

Shapiro, S. L., & Teukolsky, S. A., 1983, Black holes, white dwarfs, and neutron stars: The physics of compact objects, (New York: Wiley)

Shore, S. N., L. M., & van den Heuvel, E., 1994, Interacting Binaries, (Berlin: Springer)

Sina, R., 1996, *Ph.D. thesis*, University of Maryland

Slater, G., Salpeter, E. E., & Wasserman, I., 1982, Astrophys. J., 255, 293

Sokolov, A. A., & Ternov, I. M., 1964, Sov. Phys. Doklady, 8, 1203

Sokolov, A. A., & Ternov, I. M., 1968, Synchrotron Radiation, (New York: Pergamon)

Soldner, J., 1804, Astron. Jahrbuch, 161, reprinted in Ann. der Phys. (1921), 65, 593

Soong, Y., Gruber, D. E., Peterson, L. E., & Rothschild, R. E., 1990, Astrophys. J., 348, 641

Staelin, D. H., & Reifenstein, E. C., 1968, Science, 162, 1481

Staubert, R., 2003, ChJAAS, 3, 270

Staubert, R., Bezler, M., & Kendziorra, E., 1983, Astron. Astrophys., 117, 215

Staubert, R., et al., 2004, in 5th INTEGRAL Workshop on the INTEGRAL Universe, ed. V. Schoenfelder, G. Lichti, C. Winkler, (Noordwijk: ESA Publications Division), 259

Staubert, R., Schandl, S., Klochkov, D., Wilms, J., Postnov, K., & Shakura, N., 2006, in The Transient Milky Way: A Perspective for MIRAX, ed. J. Braga, F. D'Amico, R. E. Rothschild, Vol. 840, (San Francisco: AIP), 65

Staubert, R., Shakura, N. I., Postnov, K., Wilms, J., Rothschild, R. E., Coburn, W., Rodina, L., & Klochkov, D., 2007, Astron. Astrophys., 465, L25

Stella, L., 2001, in X-ray Astronomy: Stellar Endpoints, AGN, and the Diffuse X-ray Background, Vol. 599, (San Francisco: AIP), 365

Suchy, S., et al., 2007, in prep.

Tanaka, Y., 1983, 2

Tanaka, Y., 1986, Observations of Compact X-Ray Sources, Lecture Notes in Physics 255, (Berlin: Springer), 198

Tananbaum, H., Gursky, H., Kellogg, E. M., Levinson, R., Schreier, E., & Giacconi, R., 1972, Astrophys. J., 174, L143

Terada, Y., et al., 2006, Astrophys. J., 648, L139

Thompson, C., & Duncan, R. C., 1993, Astrophys. J., 408, 194

Thorsett, S. E., & Chakrabarty, D., 1999, Astrophys. J., 512, 288

Timmes, F. X., Woosley, S. E., & Weaver, T. A., 1996, Astrophys. J., 457

Trümper, J., Pietsch, W., Reppin, C., Sacco, B., Kendziorra, E., & Staubert, R., 1977, NY Acad. Sc., 302, 538

Trümper, J., Pietsch, W., Reppin, C., Voges, W., Staubert, R., & Kendziorra, E., 1978, Astrophys. J., 219, L105

Tsuruta, S., & Cameron, A. G. W., 1966, Canadian Journal of Physics, 44, 1863

Tsygankov, S. S., & Lutovinov, A. A., 2005, Astronomy Letters, 31, 380

Tsygankov, S. S., Lutovinov, A. A., Churazov, E. M., & Sunyaev, R. A., 2006, Mon. Not. R. Astron. Soc., 371, 19

Turatto, M., 2003, Classification of Supernovae, Lecture Notes in Physics 598, (Berlin: Springer), 21–36

Urpin, V. A., Levshakov, S. A., & Iakovlev, D. G., 1986, Mon. Not. R. Astron. Soc., 219, 703

van der Klis, M., 2006, Advances in Space Research, 38, 2675

van Kerkwijk, M. H., van Oijen, J. G. J., & van den Heuvel, E. P. J., 1989, Astron. Astrophys., 209, 173

van Kerkwijk, M. H., van Paradijs, J., Zuiderwijk, E. J., Hammerschlag-Hensberge, G., Kaper, L., & Sterken, C., 1995, Astron. Astrophys., 303, 483
Ventura, J., 1979, Phys. Rev. D, 19, 1684
Wang, J. C. L., Lamb, D. Q., Loredo, T. J., Wasserman, I. M., & Salpeter, E. E., 1989, Phys. Rev. Letters, 63, 1550
Wang, J. C. L., Wasserman, I. M., & Salpeter, E. E., 1988, Astrophys. J., 68, S735
Wang, J. C. L., Wasserman, I. M., & Salpeter, E. E., 1989, Astrophys. J., 338, 343
Wang, Y.-M., & Frank, J., 1981, Astron. Astrophys., 93, 255
Wang, Y.-M., & Welter, G. L., 1981, Astron. Astrophys., 102, 97
Watanabe, S., et al., 2006, Astrophys. J., 651, 421
Weth, C., 2001, A Doppler Shift model to explain the Cyclotron Line Variability in X-Ray Pulsars, astro-ph/0101044
Wheaton, W. A., et al., 1979, Nature, 282, 240
Wheeler, J. A., 1966, Ann. Rev. Astron. Astrophys., 4, 393
White, N. E., Swank, J. H., & Holt, S. S., 1983, Astrophys. J., 270, 711
Wijnands, R., 2001, Advances in Space Research, 28, 469
Wilms, J., Allen, A., & McCray, R., 2000, Astrophys. J., 542, 914
Wilson, C., 2006, in Chandra Proposal 2101
Wilson, C. A., & Finger, M. H., 2005, RXTE confirms cyclotron line near 50 keV for A 0535+26, ATEL 605
Woods, P. M., & Thompson, C., 2006, Soft gamma repeaters and anomalous X-ray pulsars: magnetar candidates, Cambridge Astrophysics Series 39, (Cambridge, UK: Cambridge University Press), 547–586
Woosley, S. E., Heger, A., & Weaver, T. A., 2002, Rev. Mod. Phys., 74, 1015
Yahel, R. Z., 1979, Astrophys. J., 229, 73
Yakovlev, D. G., & Pethick, C. J., 2004, Ann. Rev. Astron. Astrophys., 42, 169
Zane, S., Turolla, R., Stella, L., & Treves, A., 2001, Astrophys. J., 560, 384
Zhang, C. M., Yin, H. X., Kojima, Y., Chang, H. K., Xu, R. X., Li, X. D., Zhang, B., & Kiziltan, B., 2007, Mon. Not. R. Astron. Soc. 374, 232

APPENDIX A

Model implementation in *XSPEC*

XSPEC model types

There are two types of user-built models which may be included into the *XSPEC* spectral fitting software (Arnaud, 1996):

- table models, and
- analytic models.

For the table model type (Arnaud, 1995) it suffices to supply a FITS table of a certain form, containing the user's set of model spectra. *XSPEC* integrated interpolation routines are used for the calculation of intermediate spectra when fitting the model to data. The creator of the FITS table model can chose between linear or logarithmic interpolation methods.

An analytic model in *XSPEC* is supplied in form of a *Fortran* coded function. If the model is an additive model, this function, for a given energy grid E_i, a given initial number of photons per energy bin $(N_E^{\text{initial}})_j$ and a given set of model parameters, returns the modeled number of photons per energy bin $(N_E^{\text{final}})_j$. On the other hand, a multiplicative model returns a factor $(f_E^{\text{final}})_j$ per energy bin.

`cyclomc`

`cyclomc` formally is implemented as an analytic *XSPEC* model, although it is based on a discrete set of Monte Carlo spectra which are stored in the form of FITS tables. An implementation as a multiplicative *XSPEC* table model, although most straightforward, was ruled out for two reasons: first, the line shapes are dependent on the continuum. A multiplicative model, calculating the line features for arbitrary *XSPEC* continua, would therefore necessarily bring about inconsistencies. Second, the positions of the lines depend strongly on the magnetic field strength, which is one of

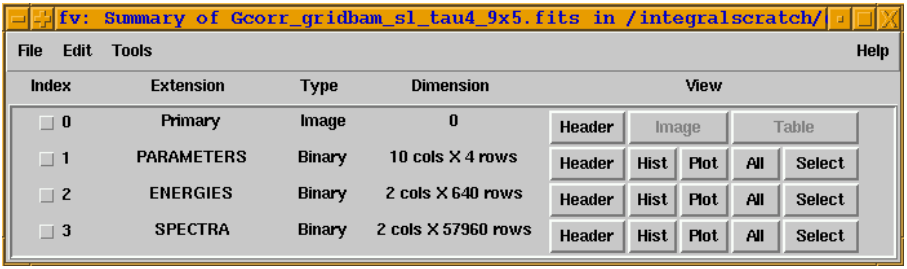

Figure A.1: FITS tables file. Various extensions include the model parameter points (PARAMETER) for B, $T_{\rm e}$, μ and $E_{\rm in}$, the energy grid $E_{\rm out}$ (ENERGY) and the calculated Green's functions (SPECTRA). SPECTRA contains two columns: the first column contains the parameter combination B, $T_{\rm e}$, μ, and $E_{\rm in}$ for which the simulations were run. The second column is a vector of the 640 Green's functions for all output energies $E_{\rm out}$.

the fit parameters. Simple interpolation between spectra at two grid points of different B implies a mixing of B-fields with ΔB linked to the grid spacing, broadening the lines artificially. Hence, a self-consistent approach requires the implementation of `cyclomc` as an analytic model function. Lacking a simple analytic expression for the line shapes, it is based on a specific interpolation and convolution model. For a given energy grid and continuum flux (model), `cyclomc` returns the final flux (continuum and lines) for arbitrary fit parameter sets within preset bounds.

FITS tables

For running `cyclomc`, the general user must obtain both the model function and four to twelve FITS tables comprising the simulation results for one to three a priori calculated geometries and for four values of the optical depth. One must then compile `cyclomc` in a local *XSPEC* model directory, and set the environment variables accordingly, e.g.,

```
setenv LMODDIR /home/user/local.models
setenv LD_LIBRARY_PATH $LMODDIR:$LD_LIBRARY_PATH.
```

The user may then chose a geometry (cylinder, slab 1-1 or slab 1-0) by setting the environment variable, `$CYCLOMOD`, to point at a corresponding directory, e.g.,

```
setenv CYCLOMOD /home/user/cyl,
```

containing the model results for this geometry. The model code expects to find four FITS tables (one for each optical depth), named `mc_taui.fits` ($i = 1, 2, 3, 4$) in `$CYCLOMOD`. For any spectral data in *XSPEC* the model can now be called with the

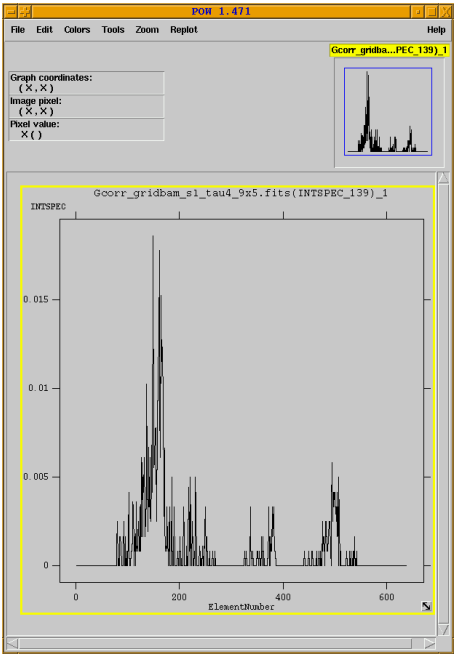

Figure A.2: Illustration of Green's functions storage in FITS tables.

syntax

`model cyclomc · <continuum>`.

If no FITS tables are found, an error message occurs. Each FITS table contains the Green's functions for all parameter combination of B, $kT_{\rm e}$ and μ for the redistribution from $n(E_{\rm in})$ energies (monoenergetic photon injection) to $n(E_{\rm out})$ different energies $E_{\rm out}$. The FITS tables' structure, which formally follows the instructions for XSPEC table models, is illustrated in Fig. A.1. Before the actual fit procedure, one should check if the hard and soft bounds of the parameters B_{12} and $T_{\rm e}$ correspond to the 'MINIMUM' and 'MAXIMUM' column entries for $B/B_{\rm crit}$ and $kT_{\rm e}$ in the PARAMETERS extension of the FITS tables, and to reset them with *XSPEC*'s 'newpar' command in case. The simulation results for the whole parameter grid are stored in the second column of the extension, named SPECTRA. Each line contains one 'spectrum' which effectively stores $n(E_{\rm out})$ Green's functions for the energy redistribution G($E_{\rm in} \rightarrow E_{\rm out}$) of the continuum photons (see Fig. A.2).

The concept of Green's functions

"From the viewpoint of mathematics it allows one to generate solutions to any inhomogeneous linear differential equation with boundary conditions. From the viewpoint of radiation physics the Green's function relates a disturbance to its measurable effect or response. From the viewpoint of engineering $G(x;\xi)$ expresses those inner workings of a linear system which relates its input to its output.[1]"

In linear algebra, an inverse operator $G = (\hat{A} - \lambda\hat{B})^{-1}$ which solves

$$\mathbf{u} = G\mathbf{b} \quad \text{for} \quad (\hat{A} - \lambda\hat{B})\mathbf{u} = \mathbf{b} \tag{A.1}$$

in infinite dimensional Hilbert space is called the Green's function of $(\hat{A} - \lambda\hat{B})$. The solution of a corresponding boundary problem

$$\begin{aligned} Lu(x) &= -f(x) \quad a < x < b \\ B_1(u) &= 0 \\ B_2(u) &= 0 \end{aligned}$$

can be expressed by its Green's function, which fulfills

$$\begin{aligned} LG(x;\xi) &= -\delta(x-\xi) \quad a < x, \xi < b \\ B_1(G) &= 0 \\ B_2(G) &= 0\,, \end{aligned}$$

as

$$u(\xi) = \int_a^b G(\xi;x) f(x) dx \tag{A.2}$$

In the framework of this work the 'physicist's and engineer's approach' is taken, and the term 'Green's functions' is adopted to describe the transition probabilities from an initial photon state (E, θ) to its final state (E', θ') after propagation through the plasma (compare, e.g., Kontar et al., 2006; Becker & Wolff, 2007). The final energy distribution of the photons, their emergent spectrum, can be given as a function of the initial one as

$$F^{\text{em}}(E_0, \theta_0) = \int_{-\infty}^{+\infty} F^{\text{initial}}(E, \theta) G(E \rightarrow E_0, \theta \rightarrow \theta_0) dE d\theta\,. \tag{A.3}$$

[1] from 'Linear Mathematics in infinite dimensions' by N. Drakos and R. Moore, `http://www.math.ohio-state.edu/~gerlach/math/BVtypset/node166.html`

The discretized Green's functions obtained from the simulations give the transition probabilities between discrete energy and angular intervals. They take the form of a response matrix of the line-forming region to the seed photons. Under the condition of initial isotropy, Eq. A.3 is therefore approximated by the discrete sum (see chapter 4, eq. 4.7)

$$\frac{N^{\text{final}}_{E_j,\theta_k}}{\Delta E_j} = F^{\text{em}}(E_j,\theta_k) = \frac{\sum_i G^(E_i \rightarrow E_j,\theta_k)\, F^{\text{cont}}(E_i)\Delta E_i}{\Delta E_j}\,. \tag{A.4}$$

In the following, the angle θ is parameterized by its cosine μ, in accordance with the simulation setup.

Convolution and interpolation procedure

During the actual fitting of the data, for each test parameter set during *XSPEC*'s fitting procedure, the flux is calculated internally from convolution of the chosen continuum model with an interpolated set of Green's functions from the Monte Carlo simulations (compare chapter 4).

Technically, calculating $\left\{N^{\text{final}}_{E_j,\mu_k}\right\}_{j,k}$ involves the following steps

- regridding of the input energy grid $\left\{E_j^{\text{XSPEC}}\right\}_j$ and photons per bin $\left\{N^{\text{initial}}_{E_j}\right\}_j$ to the internal energy resolution $\{E_i/B_{12}\}_i$ of the stored Green's functions.
- calculating the surface magnetic field, accounting for the redshift from the supplied fit parameter B_{12}
- association of all *XPSEC* fit parameters with neighboring values of B, Te, μ, τ on the discrete parameter grid
- marking of all ($2^4 \times 161 \times 640$) relevant Green's functions (stored in 8×161 lines for each optical depth from two FITS tables)
- two-dimensional linear interpolation in T_{e} and μ
- determination of the shifts in energy for the Green's functions of both neighboring B values.
- linear interpolation in B of the shape of the Green's functions, while accounting for the shifts in energy on the energy grid.
- linear interpolation in τ

- convolution of the *XSPEC* initial spectrum $\left\{N_{E_j}^{\text{initial}}\right\}_i$ with the interpolated Green's functions
- regridding of the convolved spectrum (flux) from $\{E_i/B_{12}\}_i$ to $\left\{E_j^{\text{XSPEC}}\right\}_j$

The model code has been tested extensively, especially as to the consistency of the interpolated spectra with Monte Carlo spectra, calculated directly for the given parameter set.

Acknowledgements

“Live as if you were to die tomorrow. Learn as if you were to live forever.”

[Mahatma Gandhi]

Thanks to everyone who accompanied me this part of my way, learning and living!

I am very grateful to Jörn Wilms who got me started initially on this whole cyclotron line business and the fascinating “magnetized world”. Many thanks go to both my thesis advisors, Jörn Wilms and Andrea Santangelo, and likewise to Peter Kretschmar for many inspiring discussions throughout this work.

Sunny times were my visits to ESAC, Spain. Marcus, I am very much in your debt for opening me the first door there and for introducing me to Jörn and to the guys from Tübingen in the first place. Peter, thanks for for joining in in advising my thesis (moving to ESAC just in time), and for welcoming me as your temporal office mate any time.

A Mar, Auré (Jean-Pierre), Isa, Pili, Jenny, Celia, Ruben, Stefano, Flori, Iñaki, Ester y a todos los demas...gracias por todo!! la vida en ESAC y en Madrid siempre fue tan genial por vosotros.

Thanks to everyone at the IAAT for hanging around, for my first gig in a christmas-songs-and-heavy-metal band ever, for the little Swabian I learned (‘Es tut wieder.’/‘Es hat noch Kaffee.’), for countless mugs of Espresso, and for the tons of cake you tirelessly supplied.

Special thanks go to Isa, Elke and Nikolai for carefully proof-reading this thesis and to all of you who organized my ‘Nachprüfung’ giving me the unforgettable experience

of (rock-)climbing a staircaise from below in high-heels...

I am very grateful to Prof. Staubert for offering ‘words of wisdom’ when most needed.

Isabel, you were the one who helped me ‘no volverme loca’ more than once, and to share not only the office but also most emergency chocolate bars and more than one bottle of good Rioja with me...

Heiko, Johannes, Maaike, Raimund, Axel, Bärbel, Sybille, Julia, Uli, Joachim and all the others: thanks for all the time ‘on the rocks’. I hope we will climb mountains together even when we are so old we need the ‘Schweizer Flaschenzug’ to reach the top!

Many thanks go to Leonie, Jana & Britta, simply for staying friends,

to Axel, für ‘das gute Leben’,

and to my parents, my sister and all my family for being there for me – as they have always been.

Much credit goes to Rafael Araya for providing the first version of the Monte Carlo code which was the starting point of this work. I’d also like to thank the Department of Physics of the University of Warwick and the European Space Astronomy Centre of the European Space Agency for their hospitality. I’d like to acknowledge the Centre for Scientific Computing of the University of Warwick and the Regionales Rechenzentrum Erlangen for providing the computing resources used in this work. This work was supported by a scholarship from the Studienstiftung des Deutschen Volkes and by the DLR grant 50 OR 0302.

Curriculum vitae

23.07.1979	born in Düsseldorf, Germany
09.1989–06.1998	High School. Annette-von-Droste-Hülshoff-Gymnasium, Düsseldorf
06.1998	High-School Graduation
10.1998–02.2001	University. Rheinische Friedrich-Wilhelms-Universität Bonn, majors: physics and mathematics
11.2000	Bachelor of mathematics
12.2000	Bachelor of physics
10.2000–12.2002	University. major: physics, minor: astronomy
10.2001–03.2002	ERASMUS visiting student at the Universidad Autónoma de Madrid, Spain
12.2002	graduation exams
03.2003–02.2004	Research Centre Jülich. Diploma-thesis: “Diffusion of extended particles on a lattice”, Advisor: G. Schütz
02.2004	Graduation (Diploma) in physics
04.2004–10.2004	Traineeship at the European Space Astronomy Centre (ESAC) of the European Space Agency (ESA), Villafranca, Spain
06.2004	IASTE internship at the Russian Academy of Sciences, Moscow
01.2005–05.2007	Eberhard-Karls-Universität Tübingen; Institute of Astronomy and Astrophysics, ESAC, ESA, Spain; University of Warwick, UK Preparation of this thesis: “Strong magnetic fields of accreting neutron stars”. Advisors: J Wilms and A. Santangelo; funded by the German Honors Society

My academic teachers have been the professors and lecturers:

Astronomy and Astrophysics: K. de Boer, U. Klein, J. Wilms, A. Santangelo
Theoretical Physics: M. Huber, H. Monien, G. Schütz
Mathematics: C.-F. Bödigheimer, S. Hildebrandt, A. Kunoth
Experimental Physics: N. Wermes, E. Klempt, H. Hübel, J. Bisplinghoff
Applied Physics: D. Meschede, U. Klein

Lebenslauf

23.07.1979	geboren in Düsseldorf, Deutschland
09.1989–06.1998	Annette-von-Droste-Hülshoff-Gymnasium, Düsseldorf
06.1998	Abitur
10.1998–02.2001	Rheinische Friedrich-Wilhelms-Universität Bonn. Grundstudium der Physik (Dipl.) und der Mathematik (Dipl.)
11.2000	Vordiplom Mathematik
12.2000	Vordiplom Physik
10.2000–12.2002	Hauptstudium der Physik und Astronomie
10.2001–03.2002	ERASMUS Aufenthalt an der Universidad Autónoma de Madrid, Spanien
12.2002	Diplomprüfungen Physik
03.2003–02.2004	Forschungszentrum Jülich. Diplomarbeit: “Diffusion ausgedehnter Teilchen auf dem Gitter”, Betreuer: G. Schütz
02.2004	Diplom Physik
04.2004–10.2004	Traineeship am European Space Astronomy Centre (ESAC) der European Space Agency (ESA), Villafranca, Spanien
06.2004	IASTE Praktikum an der Russian Academy of Sciences, Moskau
01.2005–05.2007	Eberhard-Karls-Universität Tübingen; Institut für Astronomie und Astrophysik; ESAC, ESA, Spanien; University of Warwick, UK Anfertigung dieser Dissertation “Starke Magnetfelder akkretierender Neutronensterne”, betreut von: J. Wilms und A. Santangelo; gefördert durch die Studienstiftung des deutschen Volkes

Meine akademischen Lehrer waren die Professoren, Dozenten und Dozentinnen Dres.:

Astronomie und Astrophysik: K. de Boer, U. Klein, J. Wilms, A. Santangelo
Theoretische Physik: M. Huber, H. Monien, G. Schütz
Mathematik: C.-F. Bödigheimer, S. Hildebrandt, A. Kunoth
Experimentalphysik: N. Wermes, E. Klempt, H. Hübel, J. Bisplinghoff
Angewandte Physik: D. Meschede, U. Klein